8-2010

Optimal design of vehicle with internal space frame structure subjected to high impact load

Jagadeep Thota
University of Nevada, Las Vegas

Repository Citation

Thota, Jagadeep, "Optimal design of vehicle with internal space frame structure subjected to high impact load" (2010). *UNLV Theses, Dissertations, Professional Papers, and Capstones*. 863.
http://dx.doi.org/10.34917/2206017

OPTIMAL DESIGN OF VEHICLE WITH INTERNAL SPACE FRAME STRUCTURE SUBJECTED TO HIGH IMPACT LOAD

by

Jagadeep Thota

Bachelor of Engineering
Bangalore University, India
2001

Master of Science
University of Nevada, Las Vegas
2006

A dissertation submitted in partial fulfillment of
the requirements for the

Doctor of Philosophy in Mechanical Engineering
Department of Mechanical Engineering
Howard R. Hughes College of Engineering

Graduate College
University of Nevada, Las Vegas
August 2010

THE GRADUATE COLLEGE

We recommend that the dissertation prepared under our supervision by

Jagadeep Thota

entitled

Optimal Design of Vehicle with Internal Space Frame Structure Subjected to High Impact Load

be accepted in partial fulfillment of the requirements for the degree of

Doctor of Philosophy in Mechanical Engineering

Mohamed B. Trabia, Committee Chair

Brendan J. O'Toole, Committee Chair

Woosoon Yim, Committee Member

Georg F. Mauer, Committee Member

Zhiyong Wang, Committee Member

Samaan G. Ladkany, Graduate Faculty Representative

Ronald Smith, Ph. D., Vice President for Research and Graduate Studies
and Dean of the Graduate College

August 2010

ABSTRACT

Optimal Design of Vehicle with Internal Space Frame Structure Subjected to High Impact Load

by

Jagadeep Thota

Dr. Mohamed B. Trabia, Examination Committee Chair
Professor of Mechanical Engineering
University of Nevada, Las Vegas

Dr. Brendan J. O'Toole, Examination Committee Chair
Associate Professor of Mechanical Engineering
University of Nevada, Las Vegas

Armored military vehicles are heavily used in modern warfare. These vehicles are subjected to lethal attacks from projectiles and land mines. The shocks from these attacks may risk the safety of the occupants and damage the electronic instruments within the vehicle. Extensive research on the analysis and reduction of shocks on civilian vehicles has been performed. Fewer researchers addressed these problems in the case of military vehicles. Space frames are usually used to enhance structural strength of the vehicle while reducing its overall weight. These frames comprise of beams connected together at joints. Recently, space frames were incorporated in military vehicles.

In this dissertation, a finite element model of a military vehicle with an internal space frame is developed. The space frame is composed of hollow square cross-section bars and angle sections. These frame members are bolted to the joints. The space frame is enclosed by uniform-thickness armor, except at the turret. The vehicle is subjected to high impact load that simulates a projectile hit. The vehicle design is optimized to reduce the overall mass, and shock at critical locations of the space frame.

A lab-scale space frame structure derived from the military vehicle space frame is designed and built. The lab-scale space frame is subjected to non-destructive shock propagation tests. A finite element model of this structure is developed with the objective of matching the experimental results.

ACKNOWLEDGEMENTS

I am greatly indebt to and express sincere gratitude to my dissertation advisors Dr. Mohamed B. Trabia and Dr. Brendan J. O'Toole for their invaluable guidance and suggestions throughout the entire course of this research work. Working with Dr. Trabia has strenghtened my passion for research and more critically taught me a disciplined appraoch in obtaining the research objectives. He was always available for answering any questions, and showed a path however dead the road ahead seemed. I am extremely proud to be his student. Dr. O'Toole is an outstanding individual and a true gentleman. He has given me the oppurtunity to work not only on my dissertation but also on various other research projects which have helped me in getting an enormous amount of research exposure and experience. His caring nature and efforts to fund me through my dissertation have helped me concentrate on my doctoral studies without worring about the financial aspect of it, and resulted in completing this work within the plannned time. I am extremely fortunate to have done my graduate studies under his tutelage.

I would like to thank Dr. Woosoon Yim, Dr. Samaan G. Ladkany, Dr. Georg F. Mauer , and Dr. Zhiyong Wang for their time in reviewing the prospectus, dissertation, participation of defense, and counseling of the dissertation as the committee members. Dr. Ladkany is one of my favourite professors and he is a nice individual to converse with. His ability to explain complex theories from simple basics have helped me master some of the harder subjects. Dr. Mauer is the first professor I have worked under, as a teaching assistant, in my graduate life and hence needs a special mention. My teaching abilities and interaction skills were highly enhanced during the teaching assistant position under him.

I am very grateful to the ‘Nelson family’; Stacy, Kevin and Debbie (Stacy’s mother) for considering me a part of their family. The love and affection they have showered on me has made my stay away from my parents and brothers bearable. Stacy and I have worked together in various projects and they have all been thoroughly enjoyable. She has been a wonderful colleague and friend, and will always remain my favorite ‘grandma’.

I would like to express my heartiest gratitude to my friends and colleagues; Srujan Babu Sridharala, Ravi Seera, Karthik Doppala, Gopi Nallani, Venkat Mudupu, Pavan Singaraju, Shivakanth Gutta, Kimberly Clark, Julio Malpica, Brianna Watson Mayorga, Kumarswamy Karpanan, Deepaksankar Somasundaram and Balaji Aresh to name a few. They have always stuck by me during my ups and downs, and are instrumental in making my graduate life enjoyable.

I would like to take this opportunity to be thankful for having a great and wonderful family. My parents, mom Swarajya Lakshmi and dad Narasimha Murthy, have been extremely supportive of my studies and always motivated me to excel in my field of study. I am fortunate to have such loving and understanding parents. My brothers, Pradeep and Sandeep, are instrumental in what I have achieved till date as all I had to do was follow the successful path laid out by them. Special acknowledgement to Pradeep for always being there, as a family member, and looking out for me during my graduate study. He has always been a positive influence on my career. I would like to dedicate this dissertation to my family, especially my mom.

TABLE OF CONTENTS

LIST OF TABLES

LIST OF FIGURES

CHAPTER 1

INTRODUCTION

Armored personnel vehicles are extensively used in modern warfare. These vehicles are subjected to lethal attacks from projectiles and land mines. The shocks from these attacks may risk the safety of the occupants and damage the electronic instruments within the vehicle. Extensive research on the analysis and reduction of shocks in civilian vehicles has been conducted [1-4]. Fewer researchers however addressed these problems in the case of military vehicles [5-7].

In the modern world, light combat vehicles and armored vehicles are playing a key role in supporting the troops and other heavily armored combat vehicles. As such, during the real combat situations they are subjected to extreme loading scenarios. Fierce battlefield environments make these vehicles susceptible to damage and the survivability of the occupants becomes questionable. Appropriate design of these vehicle structures against severe on field conditions is vital to ensure occupant survivability and vehicular operational needs [5].

Several types of armored vehicles are used in modern wars. While heavily armored vehicles play a major role, medium and light vehicles usually help in consolidating positions. While all types of combat vehicles need to be designed keeping in view of their severe environments, light combat vehicles are at greater risks when subjected to shock loads. These shock loads primarily occur due to impacts from projectiles or blasts. An area of critical concern is the propagation of shocks within combat vehicles to the location of the driver and the other personnel in the crew compartment as well as attachment points for optical and electronic devices [6]. Failure of equipment due to shock and vibration may render the whole system ineffective leading to life threatening situations. Detailed study of shock propagation can help reduce these effects by appropriate design of all the structural sub-assemblies.

1.1 Literature Review

1.1.1 Description and Analysis of Space Frame Structures

Medwadowski [8] stated that in general, all structures could be divided into two categories, depending on the manner in which they transfer load. The most common category is that of rigid structures, which includes space frames. When subjected to applied loads rigid systems experience deformations that are small compared to the overall dimensions of the structure itself. This is true even in the case of "large deformations". The geometry of the structure after deformation is essentially the same as its geometry prior to deformation. Thus, in majority of cases, the mathematical model is linear and generally, the equations of equilibrium can be written for the undeformed structure. In most general cases, internal force transfer in rigid structures is achieved with the aid of three distinct mechanisms: axial, bending and torsional. Of these, the axial force transfer mechanism is considered most efficient, since all fibers of an element participate equally in the task.

The second category is of flexible structures or tension structures. When subjected to transverse loads, flexible structures experience a significant change of geometry. In fact, their ability to transfer such loads depends on their ability to change shape. Thus the problem of analysis of tension structures involves a mathematical model, which experiences deformations large compared to the overall dimension of the system, hence geometrically nonlinear. The consequences are likely to be severe, not only from the point of view of analysis, but also from the point of view of fabrication of elements, and construction.

It is expected that the beam members of a space frame within an armored vehicle may undergo severe deformations when subjected to projectile impacts and blasts. Similarly, it is observed that load transmitted within assembled structures is influenced by the distribution of joints of the space frame [9]. Therefore, the study of shock transmission through the various jointed components within a combat vehicle is of particular interest due to the need of guaranteeing the survivability of its occupants. Mackerle [10, 11] published a bibliography of research pertaining to the finite element vibration and dynamic response analysis of engineering structures subjected to impact, blast or shock loadings.

Meek et al. [12-14] conducted research on geometrically nonlinear static analysis of three-dimensional space frame structures. The elastic analysis of frame structures through FE method in the post-buckling range inevitably involves the solution of large systems of nonlinear equations. The authors [12-14] proposed that the most satisfactory way of solving such problems was to combine the arc-length method within each increment with the Newton-Raphson method as the iteration strategy. For large joint rotations, Oran's joint orientation matrix was used to update the rotational displacement of a joint. The two examples studied by the authors were a two hinged deep arch and a shallow geodesic dome. The work dealt with the 'imperfect' approach to trace the secondary paths of three-dimensional frame structures. Eigenvetors are calculated at bifurcation points to force the structure on to the secondary path by introducing small perturbation either in load or in geometry.

A dynamic response analyses method of space frame structures was presented by Masuda et al. [15], which can deal with frames having finite rotations in the three-dimensional space. This method mainly concentrates on studying the dynamic instability (a state at which small increment in loading produces sudden changes in maximum response) in the presence of strong geometric non-linearity and three-dimensional behavior. Karpurapu et al. [16] proposed a kinematic model for linear/nonlinear analysis that is suitable for the analysis of three-dimensional framed structures of general shape. The accuracy of the proposed model was evaluated by analyzing two full-scale structures, four-legged stiff tower and nine-legged tower, Figure 1, for random and periodic ground accelerations applied at various frequencies. The kinematic model comparison with the full structure was excellent both in terms of peak magnitudes and also the distribution of peaks over the entire duration of analysis. Vasilopoulos et al. [17] successfully presented a rational and efficient seismic design methodology for regular space steel frames using an advanced time domain finite element analysis that takes into account geometrical and material nonlinearities. Two numerical examples, 3-story and 7-story steel space frame structures were presented to illustrate the method and demonstrate the advantages.

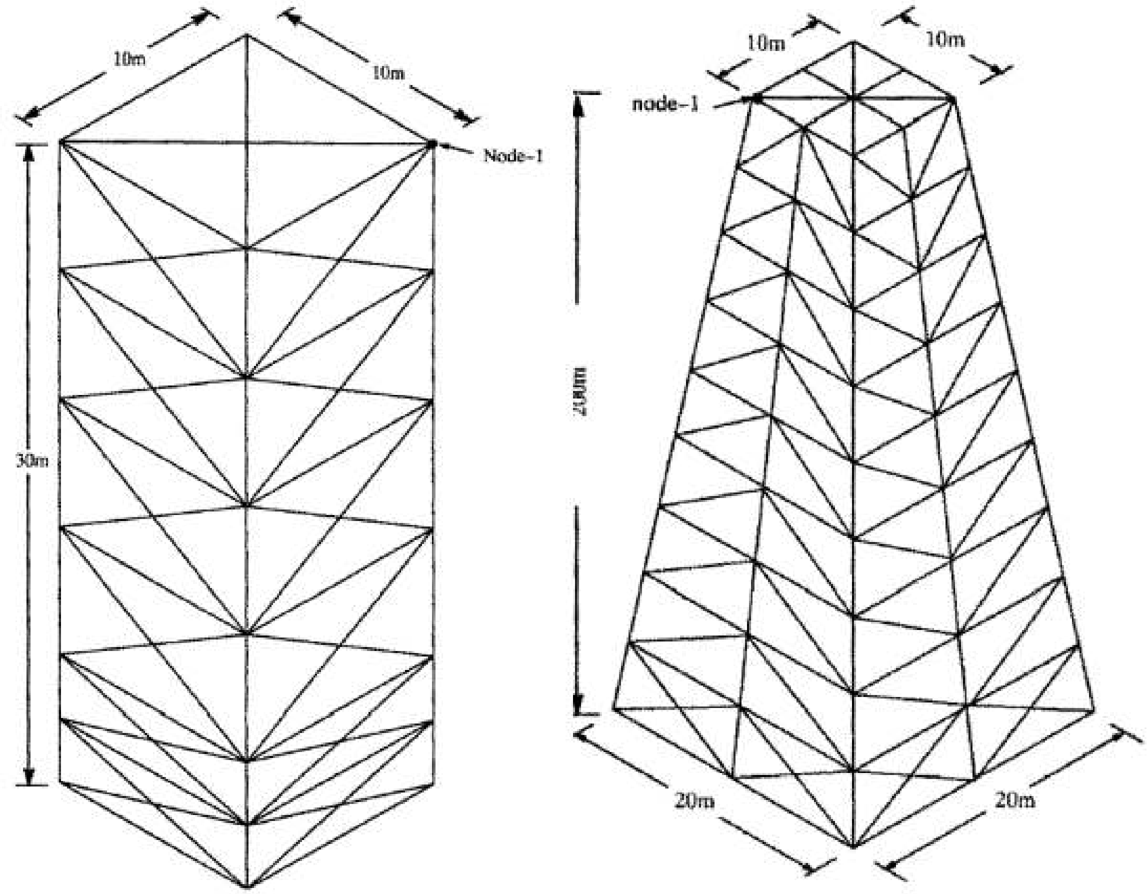

Figure 1.1: Space frame structures analyzed by Karpurapu [16]

Goman et al. [18] suggested a displacement-based finite element technique that can handle large deflections with rotations of more than 15°. An incremental secant stiffness approach which considered the effects of joint flexibility for the nonlinear analysis of two and three-dimensional frames was used. The model was successful in handling large deflections accurately in three-dimensional space. It exhibited fast rate of convergence. A simple procedure for dynamic and static analysis of space frames undergoing large deflections was explained by Chan et al. [19]. This method combined ease of implementation and fast rate of convergence for equilibrium. Research has also been done on developing tools that help in optimizing geometric parameters of space frames by imposing stress and free frequency constraints [20]. Ohga et al. [21] used a combined finite element-transfer matrix (FETM) method to investigate space frame structures under harmonic and impulsive excitations. The authors showed that for the case of space frame structures with large number of degrees of freedom, the computation time for the FETM method is appreciably shorter than that for the ordinary finite element method.

Liew et al. [22, 23] described a second-order plastic hinge analysis of three-dimensional frame structures. This beam-column formulation is based on the use of stability interpolation functions for the transverse displacements, and considers the elastic coupling effects between axial, flexural and torsional displacements. The developed algorithm was used to predict accurately the elastic flexural buckling load of columns and frames by modeling each physical member as one element. It could also predict the elastic buckling loads associated with axial-torsional and lateral-torsional instabilities, which are essential for predicting the nonlinear behaviour of space frame structures. Material nonlinearity was modeled by using the concentrated plastic hinge approach. After applying this concept to several space frame examples, Liew [22, 23] noted that the accuracy of the plastic hinge analysis is reasonable only for cases when material stress-strain law is essentially elastic-plastic. Huu et al. [24] proposed a modified plastic hinge analysis known as fiber plastic hinge concept. This considers the second order inelastic behaviour of space steel frames. This approach compared well with the ABAQUS program for space frame structures. Dabaon et al. [25] conducted experiment to study the behaviour of steel space frames and composite semi-rigid joints. A three-dimensional finite element model was proposed using ANSYS software for the analytical investigation. With respect to initial stiffness and moment capacity, the finite element model gave good agreement with the experimental results.

A finite element formulation for analyzing prismatic thin-walled space frame structures composed of arbitrary cross sections was developed by Chen et al. [26] based on second order geometric theory. It can also be used to consider distributed loading in large-deformation analysis. Using the elemental stiffness equation, a set of global nonlinear stiffness equations were established, based on an updated Lagrangian formulation and direct stiffness assembly. A work-increment-control method, which converges quadratically, was used to solve the nonlinear equations. The FE program developed was tested on a three-dimensional L shaped space frame structure. Two types of cross sections were considered: first case had C type sections and in the second case there were I beams. When compared between distributed versus equivalent point loading, the equivalent loading leads to less accurate results.

Yu et al. [27] presented a structural analysis algorithm called the finite particle method (FPM) for kinematically indeterminate frame structures. FPM models the analyzed domain composed of finite particles. Newton's second law is adopted to determine the motions of all particles. With FPM there isn't a need to solve nonlinear equations to calculate the stiffness equilibrium matrix. Yu [27] analyzed three examples using the FPM method and showed it can produce a more accurate analysis result. Haq et al. [26] talked about a generic graph-based design language which enables the automation of space frame structures design process by facilitating the generation of a large variety of design variants very efficiently. This approach consists of basic components (vocabulary) and a set of rules (design patterns), which enables the designer to define a formal graph-based, but still domain-independent representation form of an object. The authors presented three case studies; a motorbike space frame, a transverse control arm and automotive space frame structure, and showed that this method leads to time savings and increase in product quality due to analysis of many design variants of the product. Kollar [29] discussed the stability problems of space frame structures. He proposed that space frame structures essentially show two kinds of instability: local and overall buckling. Kollar also mentions snapping of space frames under concentrated load present a special problem. According to him this problem can be treated either by the discrete or by the continuum method.

Space frame structures are built with a number of beams connected together at joints. The beam members in an armored vehicle may undergo severe deformation in the presence of high transient events like projectile impacts and blasts. To ensure the safety of the crew inside armored vehicles, the whole structure should collapse within the crushable zone to absorb the impact energy. This can be achieved by reducing the stiffness of the structure with the addition of imperfections like dents and bends [30]. The resistance of sandwich beams to dynamic loads remains to be fully investigated in order to quantify the advantages of sandwich construction over monolithic designs in shock resistant structures [30]. Every space frame structure is under some degree of direct member loading. At least, the self weight of the structure certainly affects the members directly, and in structures covered with panels their weight is also likely to apply some lateral pressure on the members. In spite of this fact, direct member loading is usually ignored in space frame designs and assumed to lead only to a negligible effect on frame performance. El-Sheikh [32] did a parametric study on space frame structures and proved conversely.

Liu et al. [33] looked at strengthening the space frame joints by reinforcing them with carbon cloth. They considered four side joints of a beam column plate, made of reinforced concrete and subjected to low cycle repeated load. Numerical simulations were carried out using ANSYS software. The results showed a marked increase in the ultimate bearing capacity and yield load of the frame side joints. The stiffness of the joints are increased due to the high strength feature of the carbon cloth.

Damages in space frame structures can be detected using state-spaced based algorithms. They traditionally involve comparisons between measurements taken at the same location but at different times to determine if a change has taken place. However, Overby et al. [34] added features such as state-space cross-prediction error and generalized interdependence such that the detection method instead compares simultaneous measurements at different locations. With this a fuller assessment of structural damage was possible. In addition, other characteristics such as extent, location, and type of damage were revealed from this method. Qian et al. [35] proposed a two-stage approach to diagnose the damage location and extent in steel braced space frame structures. The two-stage approach comprises of the damage locating vectors method and eigensensitivity analysis. To verify the effectiveness of the proposed approach, numerical simulation and experimental testing of a steel braced space frame model were performed. Ten and seven damage patterns were simulated in the numerical and experimental test respectively. Modal parameters of the undamamged and damaged structures were extracted from the acceleration data using the natural excitation technique (NexT) and the eigensystem realization algorithm (ERA). The extended damage locating vectors method was utilized to determine potentially damaged elements. Based on the identified modal information, the extent of damage of the potentially damaged elements is estimated using the second-order eigensensitivity analysis. The authors [35] demonstrated that this approach was effective when the damage of the frame members or joints in steel braced space frame structure reaches a certain level.

1.1.2 Optimization of Space Frame Structures

Research has been going on in the area of optimization of the space frame structures. The objective of a majority of this optimization work involves minimizing the mass of the space frame structures. Degertekin et al. [36] compared optimization techniques, tabu search (TS) and genetic algorithm (GA), for the optimum design of geometrically nonlinear steel space frames. TS utilizes the feature of short-term memory facility (tabu list) and aspiration criteria. GA employs reproduction, crossover and mutation operators. The objective of the optimization procedure was to obtain minimum weight frames by selecting suitable sections from a standard set of steel sections such as American Institute of Steel Construction (AISC) wide-flange shapes. Three space frame structures were considered for optimization: a 3-story 24-member space frame, 2-story 26-member space frame, and 4-story 84-member space frame, Figure 2. Stress constraints of AISC Load and Resistance Factor Design (LRFD) specification, lateral and interstory displacement constraints, and size constraints for the columns were imposed on the frames. TS resulted in obtaining 8% more lighter space frames when compared to GA. This is due to that TS does not turn back to the old designs using its artificial memory facility and it is able to inspect much more area than GA in the solution space. This increases the probability of reaching global optima in TS. However, the computing time associated with TS is larger than that of GA.

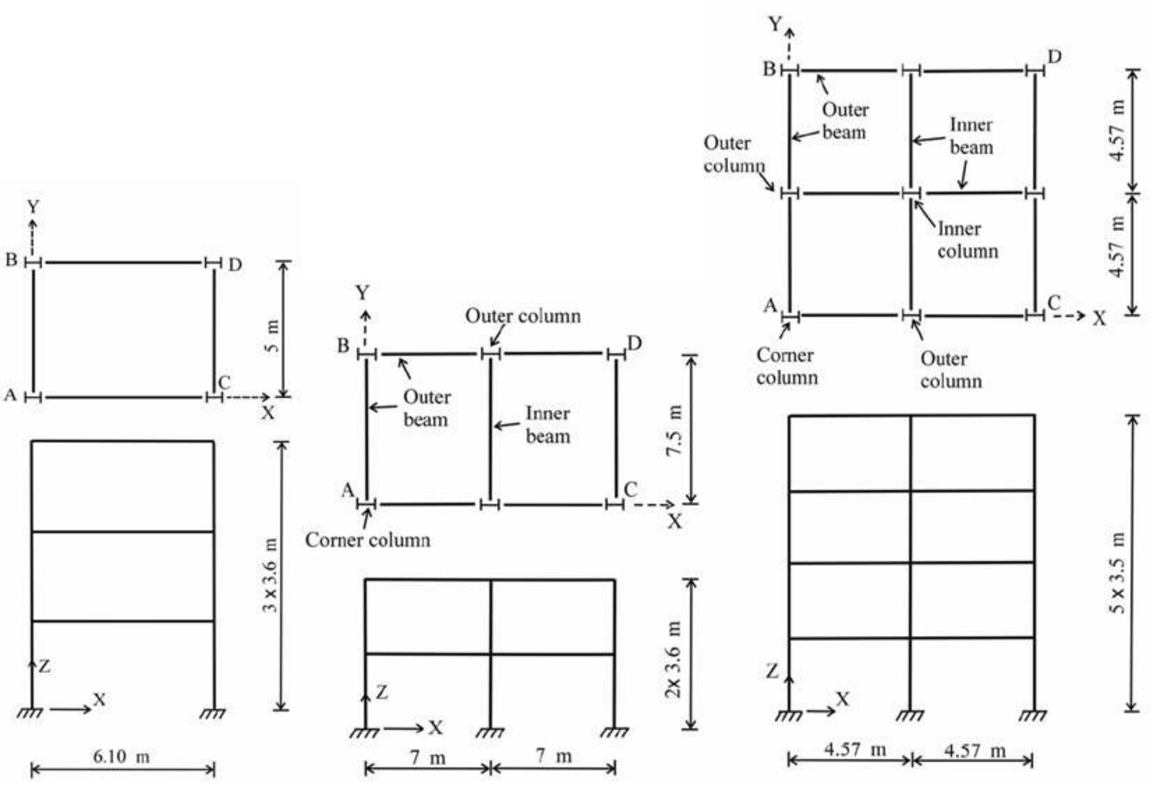

Figure 1.2: Space frame structures optimized by Degertekin [36]

Jalkanen [37] studied four heuristic methods; simulated annealing (SA), tabu search (TS), genetic algorithm (GA) and particle swarm optimization (PSO), on a discrete space frame sizing optimization problem. This work considered minimizing the mass of two cases: structure with eight beams and a structure with twenty-six beams. In both cases, the structures are subjected to displacement, stress, buckling and frequency constraints. It was shown that population based methods (GA and PSO) worked better than the local search methods (SA and TS). An optimization study similar to that of [37] was performed, but only for an eight-beam space frame structure [38]. It compared two algorithms (SA and GA) only. This work did not consider the frequency constraint. Contrary to [37], the results of [38] indicated that SA algorithm gave a better design approach for the space frame structure when compared to GA, though GA was much faster in converging toward the results. A structural optimization on a car space frame was conducted [39] using a gradient-based algorithm known as method of moving asymptotes (MMA) [40].

Hayalioglu [41] utilized a GA code to optimize the weight of steel moment-resisting space frames subjected to AISC LFRD specifications. The design variables were selected similar to [36]. The types of space frame structures considered were: 1-story 8-member space frame, 4-story 84-member space frame, and 10-story 130-member space frame. Displacement and AISC LRFD stress constraints were imposed on the structure. The optimized designs obtained using AISC LRFD code were compared to those where AISC Allowable Stress Design (ASD) was considered, and the former code resulted in lighter structures. Savings in weight for designs based on LFRD when compared to ASD were 28%, 12%, and 0.7% for the 1-storey, 4-storey, and 10-story frames respectively. For LFRD designs lighter frames were obtained when the stress constraint is dominant when compared to having dominant displacement constraints. Soegiarso [42] did a similar study using a robust optimality criteria algorithm.

Optimization of large space frame steel structures subjected to realistic code-specified stress, displacement, and buckling constraints was investigated by Soegiarso et al. [43]. The design of the space frame structure was based on the AISC ASD specifications. The structures were subjected to wind loadings according to UBC in addition to dead and live loads. A parallel-vector multi-constraint discrete optimization algorithm was developed. This algorithm is applied to three building space frame structures ranging in size from a

20-story structure with 1,920 members to 60-story structure with 5,760 members, and its parallel processing and vectorization performance was evaluated. For the largest structure, speedups of 6.4 and 17.8 were achieved due to parallel processing and vectorization, respectively. When vectorization is combined with parallel processing a very significant speedup of 97.1 is obtained.

Czyz et al. [44] presented an optimization methodology for the design of maximum natural frequency space frames subjected to constant volume constraint. Rectangular cross-sections of the frame members were considered, and the limits on the maximum and minimum sizes, as well as on the ratio of two dimensions of each cross section, were imposed. From the results of the optimization process the authors indicated that the formulation of optimality conditions based on the separation of bending energy in two orthogonal planes accelerates the convergence.

Hamza et al. [45] optimized an N-shaped truss (NTS) structure using three types of GAs and a version of TA known as reactive taboo search (RTS). RTS predicted better performance than the GAs but lacked some of the GA capabilities to span the search space. A modified RTS that uses a population based exploitation of the search history was proposed in [45], and it showed improved results. Hamza and Saitou [46] presented an automated algorithm for design of vehicle structures for crashworthiness, based on the analyses of the structural crash mode. The algorithm applies fuzzy logic concept to compare the crash modes between iterations. This algorithm was successfully tested using the models of a front half of a vehicle and a fully detailed vehicle.

Lyu and Saitou [47, 48] presented a method for identifying the optimal designs of components and joints in a space frame of a vehicle. They considered structural characteristics, manufacturability and ease of assembly. Lee and Saitou [49, 50] focused on the dimensional integrity of the vehicle design. The optimization problem was posed as a simultaneous determination of the location and feasible types of joints in a structure selected from predefined joint libraries. The structural stiffness was evaluated by finite element analysis of a beam-spring model modeling the joints and joined frames. Manufacturing and assembly costs were estimated based on the geometries of the components and joints. They used an enumerative approach for considering the dimensional integrity of an assembly. Lyu et al. [51] extended on their previous work and combined the structural stiffness, manufacturing, assembly costs, and dimensional integrity under a unified framework of multi-objective optimization process. Dimensional integrity in this case was evaluated as the adjustability of the given critical dimensions, using an internal optimization routine that finds the optimal subassembly partitioning of an assembly for in-process adjustability. GA was used as the optimization algorithm for the aforementioned studies [47-51].

1.1.3 Optimization of Military Vehicles

The following is a survey of research in the area of optimizing military vehicles for shock loading. Trabia et al. [52] conducted shock optimization studies on a single hull Armored Personal Carrier (APC) that is subject to mine blast loading or projectile impact. The objective of the study was to interrupt shock at critical locations on the APC hull by welding or bolting joints to the panels and varying its dimensional parameters. Three locations were chosen: the driver seat, the commander seat, and an instrumentation panel having the electronic components. This work was extended to the design of joints for reducing projectile impact, [53]. Sakaray et al. [54] optimized the mass of a military vehicle internal space frame, subjected to a projectile impact, by varying the locations of the space frame joints as well as their lengths while maintaining the stresses in the vehicle within a preset limit. This work showed that the problem exhibited limited sensitivity to the location of the joints.

1.1.4 Space Frame Material: Aluminum

The use of aluminum alloys in the manufacturing of components subsystems, systems and full vehicles has been on the rise, especially with electric vehicles. The drive for lighter weight and less fuel consumption has contributed to the widespread use of aluminum alloys in the automotive industry. Having a density equal to one third that of steel, aluminum material has been used as a substitute for steel at the component, system and full vehicle levels. Even when used at higher thickness, aluminum components remain lighter than steel ones. For a aluminum component with a thickness equal to one and one half that of a similar steel component, the aluminum component weight is equal to half the weight of its equivalent in steel. Aluminum components substitution in steel vehicle bodies has been on the rise as more and more steel parts are being replaced by aluminum ones. Full structural aluminum systems are more popular with aluminum intensive and electric vehicles. In these cars, either stamping or extrusion, or a combination of both is used with the vehicles bodies. Casting, at present, is not as popular as stamping or extrusion in components designed for crash energy management. Several aluminum intensive commercial vehicles have been built in the past few years including Audi ASF A8, Ford Taurus, Honda Acura NSX, Jaguar Sport XJ220, SCCA Trans-AM, GM Impact Electric, etc [54].

Aluminum is a material that is soft, ductile and possesses a great resistance to corrosion in its pure state. To enhance its strength, aluminum is often mixed with other materials to form alloys with higher yield and ultimate strength. The 5000 and 6000 series aluminum alloys are most widely used in impact applications. Aluminum has a lower modulus of elasticity when compared to steel. The modulus effect can be critical when failure is by elastic buckling. However, for plastic buckling, the failure is by material yield, rather than through local structural instability. This makes yield strength more critical in plastic buckling.

Aluminum elongation at rupture averages 15-25% in comparison to about 40% in steel. Elongation at rupture is critical in high impact applications as the strain associated with the folding process of deep collapse is high enough to crack and possible rupture the material. Elongation in the ranges of 15-25% has been demonstrated to satisfy the strain required during crashing and folding of energy absorbing components. Aluminum is easily recyclable and has a strong corrosion resistance.

The quest for lighter crash energy absorbing automotive structures has increased the use, parallel with other materials, of the 5000 (for sheets) and 6000 (for extruded parts) series aluminum structures. These aluminum structures, when properly designed and joined, are able to demonstrate a very high impact energy absorbing capability [55]. Baccouche [56] conducted frontal impact studies on aluminum vehicle space frame. Component and system modeling of the front end were conducted under NCAP's 35 mph full frontal impact using rigid body dynamic, nonlinear beam FE and stability codes. A three-dimensional spring mass model was built for the front end structure using the rigid body and finite element code MADYMO. Component load versus crash distance and system versus time response were computed. The authors concluded that the aluminum space frame vehicle demonstrated an outstanding capability to manage the impact energy during the crash.

1.2 Objectives

The objective of this dissertation is to present a methodology for the design of military vehicles with an internal space frame structure subjected to high impact or shock loadings. Based on this objective the conducted work is broadly classified into:

- Develop a FE model of a military vehicle with an internal space frame structure.
- Parameterize this FE model, and conduct mass and shock optimization studies.
- Manufacture a lab-scale space frame structure to conduct shock transmission studies.

CHAPTER 2

FINITE ELEMENT MODEL

2.1 Military Vehicle Description

A light weight military vehicle, with an internal space frame structure, is being conceptualized by the United States Army Research Laboratory (US ARL). This test vehicle is named IS-ATD and its internal space frame structure AX-1. Figure 2.1 shows a concept of the IS-ATD vehicle with an internal AX-1 space frame and bottom hull. The research for this dissertation concentrated on the upper half of the vehicle, namely the outer armor and the internal space frame, and the bottom portion, which majorly comprises of the hull and the wheels, were not considered. This was due to the objective expected from this project by the US ARL which funded the work. Also, Trabia et al. [52] and Sakaray et al. [54] dealt with the design and optimization of the hull and its joints for a military vehicle quite adequately. This study doesn't take into account some of the general vehicle components such as doors, hatches, etc so as to simplify the computational study to make it less expensive and concentrate more on the internal space frame structure. Also, these components don't significantly contribute to the studies carried out in this dissertation.

Figure 2.2 shows a simplified model of the upper half of the vehicle. The vehicle is supported by internal space frame structure, Figure 2.3. The space frame is a non-monolithic type with joints and frame members making up the entire structure. The frame members are bolted together through common components at the joints. Figure 2.4 shows a typical joint with frame members bolted to the joint branches. This arrangement allows for quick replacement of any section of the space frame that might get damaged in combat due to a projectile hit or blast impact. This design of the upper half of the vehicle with the internal space frame structure is chosen as the base model for conducting the studies in this dissertation.

Figure 2.1: IS-ATD military vehicle (model supplied by US ARL)

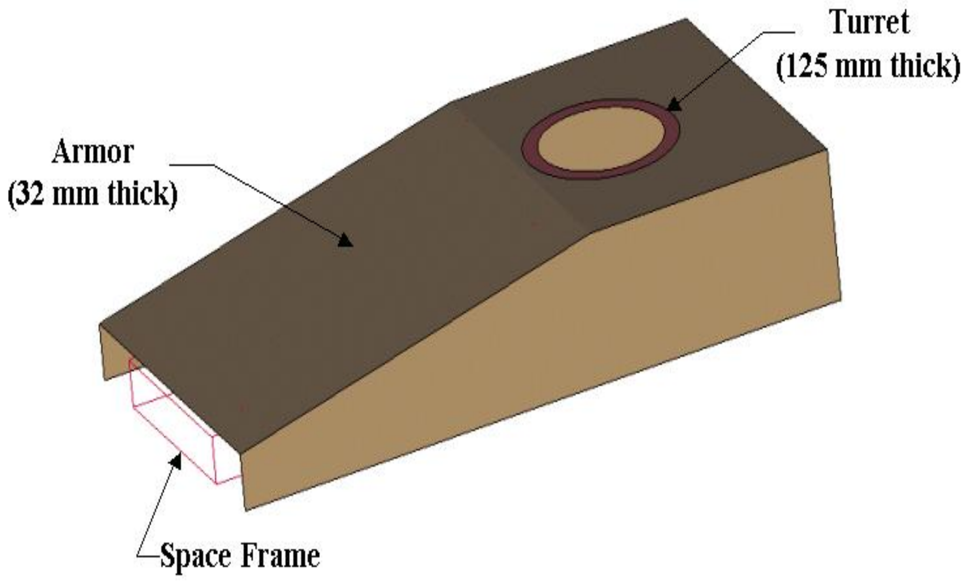

Figure 2.2: Simplified model of upper half of the military vehicle

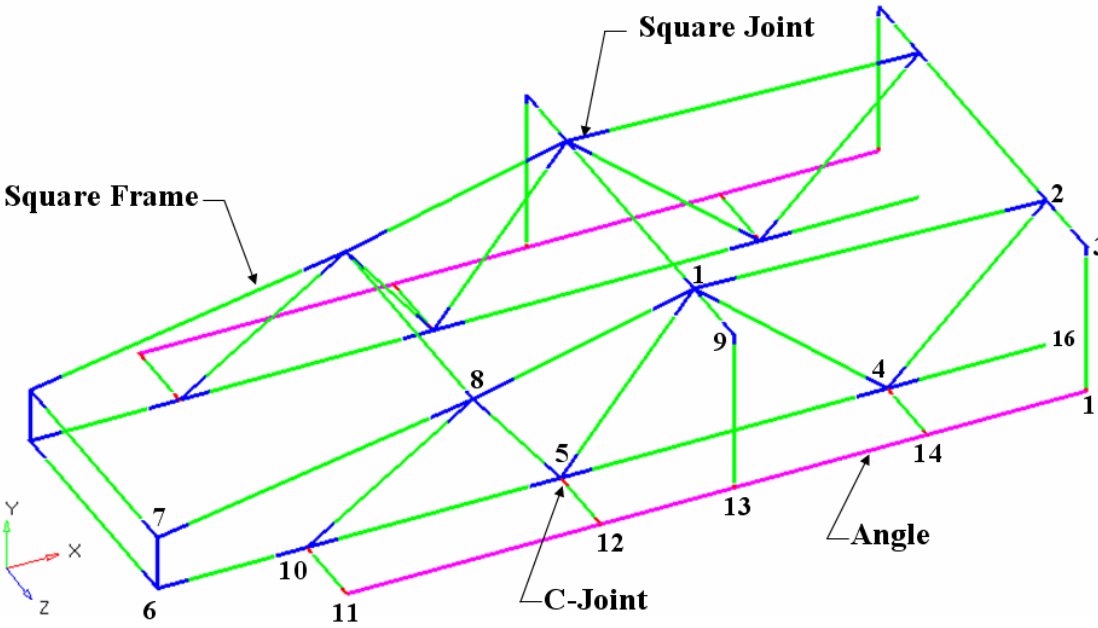

Figure 2.3: Line diagram of the internal space frame

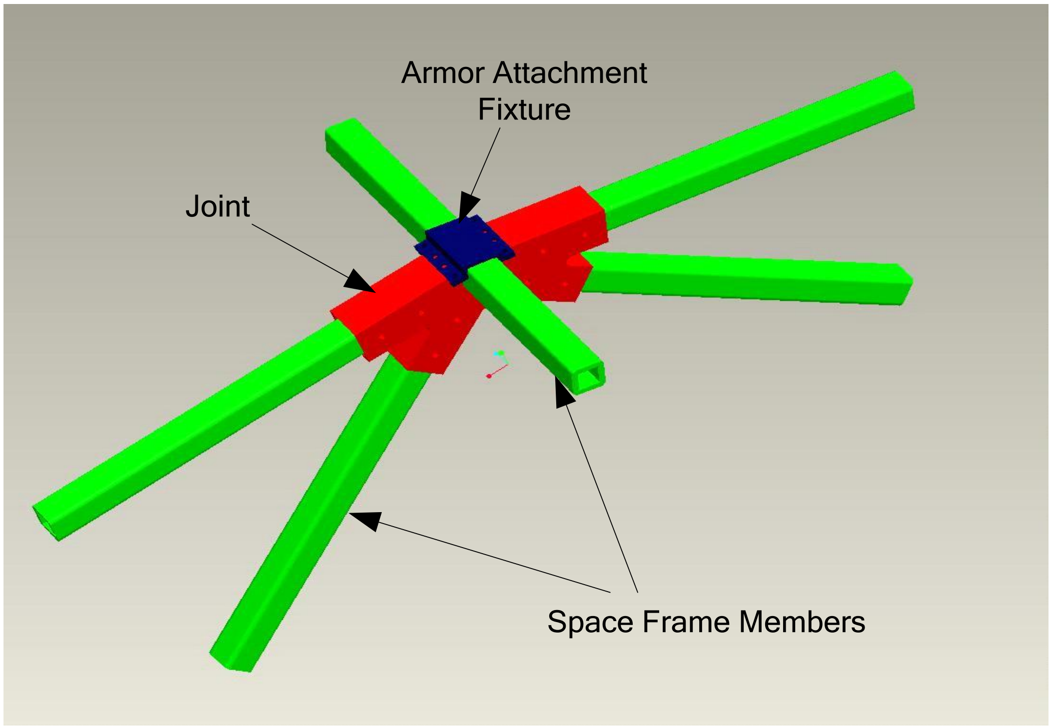

Figure 2.4: Model of a joint and frame members pertaining to that joint

The outer armor of the vehicle has a uniform thickness of 32 mm except around the turret region, where it is stiffened to be 125 mm. Overall, the upper half of the vehicle measures 4.05 m in length and 1.94 m in width. The maximum height of the vehicle, which is the back end portion of the vehicle, is 0.82 m. The height at the frontal portion of the vehicle, where it is at minimum, is 0.31 m. The vehicle, including the internal space frame, is symmetric about the x-y plane. The maximum height of the space frame structure, back end portion, is 0.76 m, and the minimum height located at the front end measure 0.25 m. The numbers in Figure 2.3 represent the space frame joint locations. Table 2.1 provides the coordinates of these joint locations. The data of the joints for other half of the space frame are not included due to the aforementioned symmetry of the vehicle. The space frame members are mostly made of hollow square section bars. The side members, one on each side, comprise of angle sections. These members are labeled *angle* in Figure 2.3. The joints comprise of either hollow square sections (S) or C-type sections (C). All sections have uniform thickness. The arrangement of the space frame members with the joints are as shown in Figure 2.3 and Figure 2.4. Table 2.2 lists the dimensions of these members and joints. The details of the branches of each joint are listed in Table 2.3. The following notation is used to describe the length and the section type of each branch. For example, $LN_{8,7}$ is the branch starting from *joint 8* along the line connecting it to *joint 7*. On the other hand, $LN_{7,8}$ is the branch starting from *joint 7* along the line connecting it to *joint 8*. $LN_{i,i}$ is the branch from *joint i* in the direction of the vehicle symmetry plane, x-y plane, which is the negative z-direction. The joints at the front of the vehicle, *joint 6* and *joint 7*, are connected with one branch only due to the space limitations in this region.

Table 2.1: Coordinates of the space frame joint locations (meters)

Joint	Type	X-coordinate	Y-coordinate	Z-coordinate
1	S	1.015	0.217	0.597
2	S	2.618	0.207	0.597
3	S	2.618	0.207	0.972
4	S	1.891	-0.512	0.597
5	S	0.400	-0.512	0.597
6	S	-1.441	-0.512	0.597
7	S	-1.441	-0.260	0.597
8	S	0.000	0.000	0.597
9	S	1.008	0.249	0.972
10	S	-0.759	-0.512	0.597
11	C	-0.759	-0.512	0.972
12	C	0.400	-0.512	0.972
13	C	1.008	-0.512	0.972
14	C	1.891	-0.512	0.972
15	C	2.618	-0.512	0.972
16	S	2.618	-0.512	0.597

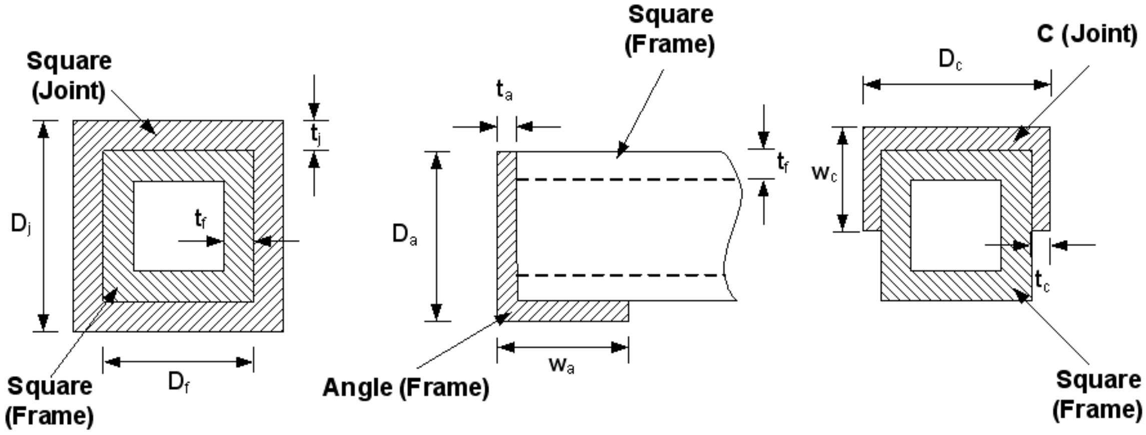

Figure 2.5: Different sections of the space frame

Table 2.2: Sectional dimensions of the space frame (mm)

Section Type			
Square (Frame)	$D_f = 69.9$	-	$t_f = 6.4$
Angle (Frame)	$D_a = 92.1$	$w_a = 28.6$	$t_a = 15.9$
C (Joint)	$D_c = 101.6$	$w_c = 25.4$	$t_c = 12.7$
Square (Joint)	$D_j = 101.6$	-	$t_j = 12.7$

Table 2.3: Details of the joint branches (mm)

Joint	Joint branch	Length	Section	Joint	Joint branch	Length	Section
1	$LN_{1,1}$	77	S	6	$LN_{6,6}$	148	S
	$LN_{1,2}$	195	S		$LN_{6,10}$	148	S
	$LN_{1,4}$	147	S	7	$LN_{7,6}$	253	S
	$LN_{1,5}$	142	S		$LN_{7,7}$	148	S
	$LN_{1,8}$	196	S		$LN_{7,8}$	148	S
	$LN_{1,9}$	77	S	8	$LN_{8,1}$	198	S
2	$LN_{2,1}$	190	S		$LN_{8,5}$	134	S
	$LN_{2,2}$	77	S		$LN_{8,7}$	197	S
	$LN_{2,3}$	77	S		$LN_{8,8}$	77	S
	$LN_{2,4}$	89	S		$LN_{8,10}$	134	S
3	$LN_{3,2}$	143	S	9	$LN_{9,1}$	143	S
	$LN_{3,15}$	51	S		$LN_{9,13}$	51	S
4	$LN_{4,1}$	120	S	10	$LN_{10,5}$	143	S
	$LN_{4,2}$	124	S		$LN_{10,6}$	143	S
	$LN_{4,5}$	143	S		$LN_{10,8}$	143	S
	$LN_{4,14}$	57	C		$LN_{10,11}$	57	C
	$LN_{4,16}$	143	S	11	$LN_{11,10}$	57	C
5	$LN_{5,1}$	124	S	12	$LN_{12,5}$	57	C
	$LN_{5,4}$	143	S	13	$LN_{13,9}$	25	C
	$LN_{5,8}$	120	S	14	$LN_{14,4}$	57	C
	$LN_{5,10}$	143	S	15	$LN_{15,3}$	25	C
	$LN_{5,12}$	57	C				

2.2 System and Software

All the computational analysis is done on a 2.8 GHz AMD Athlon processor, having a 2 GB RAM. Altair HyperMesh v9.0 is used as the pre-processor to create and mesh the 3D model of the military vehicle and the internal space frame. Explicit finite element (FE) code, LS-DYNA v971 [57], is used to simulate the structural response of the FE model. LS-POST and Altair HyperView v9.0 are used as post-processors for analyzing the results obtained after processing the FE model through LS-DYNA.

2.3 Units

The standard S.I. system of units is used to create the FE model of the vehicle and simulate the response through LS-DYNA. The basic and derived units used in defining the FE model in LS-DYNA are listed in Table 2.4 and Table 2.5 respectively.

Table 2.4: Basic units used in LS-DYNA

Basic Parameter	Units
Length	Meter (m)
Mass	Kilogram (kg)
Time	Second (s)

Table 2.5: LS-DYNA derived units

Derived Parameter	Units
Density	kg/m^3
Force	N
Stress / Pressure / Modulus	GPa
Strain	m/m (dimensionless)

2.4 Material

The entire vehicle, including the internal space frame structure with the joints, is made of Aluminum 7039 alloy heat treated to a T64. The material characteristics of this alloy are listed in Table 2.6. *MAT_PLASTIC_KINEMATIC [Appendix A] material model, present in LS-DYNA, is used to define the Aluminum 7039-T64 properties for the dynamics analysis of the vehicle. This material model essentially behaves like a bilinear elastic-plastic material and is used to model isotropic and kinematic hardening plasticity materials. This material model covers for the stress strain curve in the elastic region (until yield stress) and also in the plastic region (beyond yield stress). The stress-strain curve is assumed to be linear within each of these regions and hence made up of two straight lines. Such a simplified stress strain curve is shown in Figure 2.6. The slope of the stress-strain curve (from origin to the yield point) is defined as the Elastic Modulus of the material. While the slope of the stress-strain curve (beyond yield point) is defined as the Tangent Modulus for this material model. To determine the linear portion of the curve in the plastic region, a point that lies intermediate to the points corresponding to the ultimate stress and failure stress values on the stress-strain curve is selected so as to achieve a reasonable value for the Tangent Modulus.

Table 2.6: Material properties of Aluminum 7039-T64

Property	Value
Density (kg/m^3)	2700
Modulus of Elasticity (GPa)	69
Poisson's Ratio	0.33
Yield Strength (MPa)	380
Tangent Modulus (MPa)	562
Failure Strain (m/m)	0.13

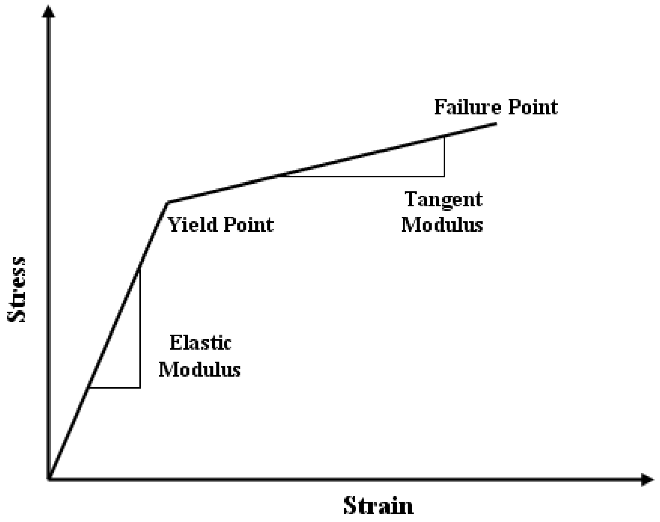

Figure 2.6: Material model for the FE analysis

2.5 Element Types

Accurate modeling of the components of the vehicle and their modes of interaction is essential for predicting the dynamic response of the vehicle under projectile impact load. A simplified model that combines shell and beam elements is used to reduce the computational time while maintaining reasonable accuracy. The outer armor and turret plates are meshed using shell elements. The internal space frame structure comprises of beam elements. Also, this model was created keeping the objective of optimization in perspective.

2.5.1 Beam Element

The beam element is defined by two nodes and is a one-dimensional line with bending capabilities. The element has six degrees of freedom at each node: translation in the nodal x, y and z directions and rotation about the x, y and z axes. A third node known as orientation node is required to create this element. This orientation node ensures that the cross-section of the beam is defined such that it is perpendicular to the axis of a segment of the beam. This type of element is used in explicit dynamic analysis.

Figure 2.7 depicts the creation of the beam element in LS-DYNA. The beginning and end of the element are defined using nodes n_1 and n_2. Node n_3 (orientation node) is added to create a plane (*r-s* plane) along with nodes n_1 and n_2 that is normal to the cross section of the element (*s-t* plane). Since n_3 is defined in the *r-s* plane, the cross section of the beam element is oriented along the *s-t* plane. Since the space frame structure comprises of straight beams or lines, single orientation node can be used to define the beam elements along that line. An example for meshing one segment of the space frame, a hollow square frame member, is shown in the Figure 2.8, where a segment of the tubular cross-section, *A-B*, uses a single orientation node, *C*, to mesh all the elements in that segment. If the beam is curved, each element in the segment should have a separate orientation node so that the orientation of cross-section is perpendicular to any given element.

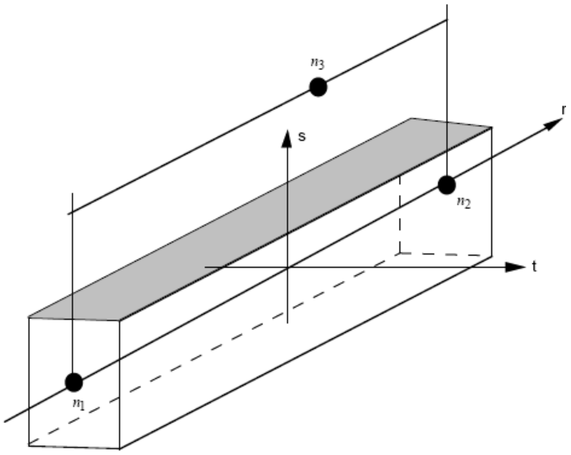

Figure 2.7: Scheme of a beam element [57]

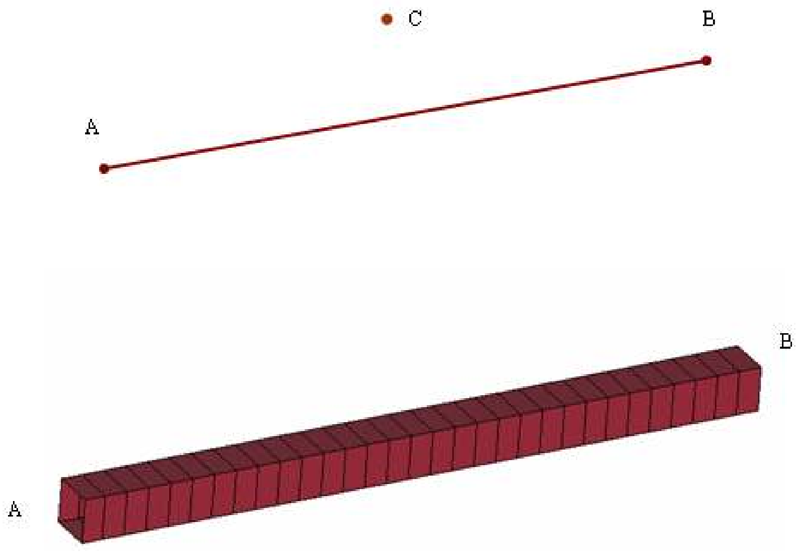

Figure 2.8: Example showing creation of the beam elements

Since the AX-1 space frame comprises of different cross-sections, Figure 2.5, two cards present in LS-DYNA are used to define the beam elements for a type of cross-section. The *SECTION_BEAM [Appendix A] card is used to define the cross-sectional dimensions of the beam. Three parameters of the beam, namely the wall thickness, height and width are defined through this card. Another card known as *INTEGRATION_BEAM [Appendix A], defines the number of integration points through the thickness of the beam and the shape of the beam cross-section (angle, C, etc). The basis of the integration point is to divide the cross-section into simple rectangular regions, as shown in Figure 2.9 for an angle section. The center of each rectangular region is an integration point. First the strain is evaluated at each integration point, based on the curvature and relative nodal displacements. Then using the basic relations, the stresses corresponding to the strains are evaluated at each integration point. Finally, the stresses are integrated numerically to produce the axial force and moments [54].

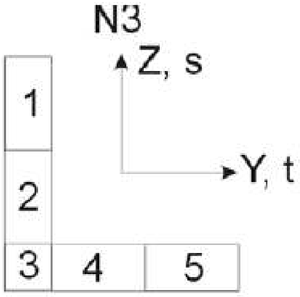

Figure 2.9: Integration points for an angle section [57]

2.5.2 Shell Element

The shell elements used in meshing the outer armor and turret plates are four-noded with bending capabilities. Both in-plane and normal loads are permitted. The element has six degrees of freedom at each node: translation in the nodal x, y and z directions and rotation about the x, y and z axes. This type of element is used in explicit dynamic analysis [57].

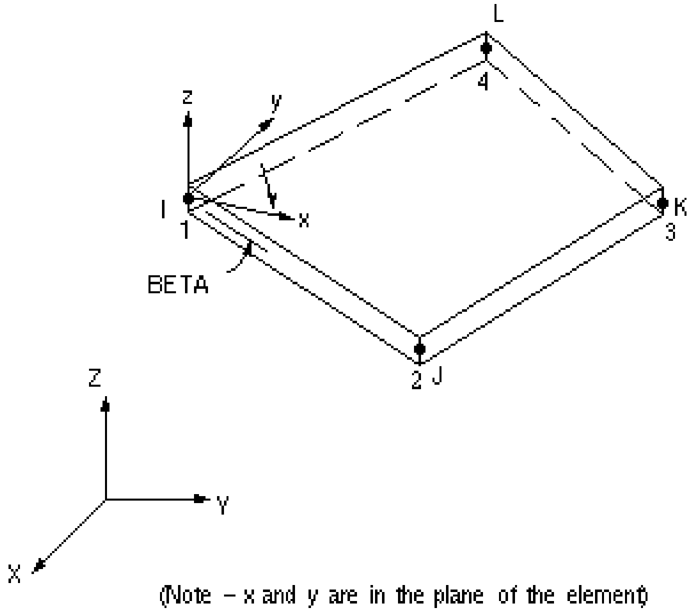

Figure 2.10: Scheme of a shell element [57]

The node numbering is done in the anticlockwise direction for this type of element as shown in Figure 2.10. With this type of node numbering the loads act towards the element, i.e., positive load acts in the negative z direction with respect to the Figure 2.10. The Belytschko-Lin-Tsay shell type of element formulation is used for this shell element. This is the default shell element formulation used in LS-DYNA due to its computational efficiency. The Belytschko-Lin-Tsay shell element [57] is based on a combined co-rotational and velocity strain formulation. The efficiency of the element is obtained from the mathematical simplifications that result from these two kinematical assumptions. The co-rotational portion of the formulation avoids the complexities of nonlinear mechanics by embedding a coordinate system in the element. The choice of velocity strain, or rate deformation, in the formulation facilitates the constitutive evaluation.

2.6 FE Model

The FE model of the vehicle is as shown in Figure 2.11. The model has a total of 1192 beam elements and 8872 shell elements. Mesh stability studies were conducted to ascertain the appropriateness of the element size in the model. Trabia et al [52] showed that a uniform mesh of 0.04 m can be used to model projectile impact on the vehicle. Therefore, the vehicle shell is meshed with a uniform size of approximately 0.04 m. The mesh of the space frame is represented in Figure 2.12. The beam elements are shown as blocks in this figure for illustration purposes only.

Figure 2.11: FE model of the vehicle with the internal space frame

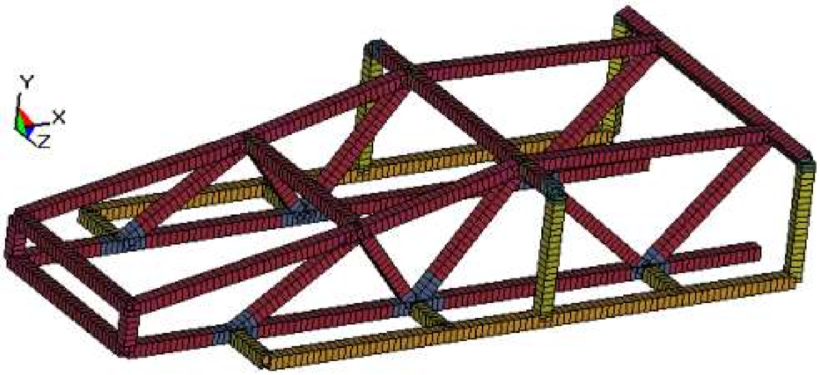

Figure 2.12: FE model of the space frame represented in 3D blocks

2.7 Boundary Conditions

2.7.1 Contact Definitions

Interaction between the space frame and armor elements was simulated using the following two types of contact definitions available in LS-DYNA:

- *CONTACT_TIED_NODES_TO_SURFACE (Appendix A) is used for the locations where the armor is rigidly fastened to the frame. Sixteen regions of these contacts are included in the model, Figure 2.13.

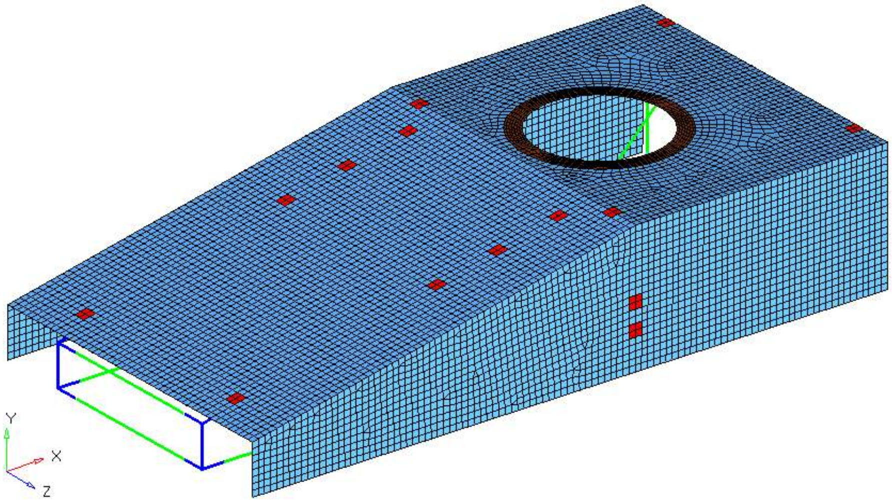

Figure 2.13: Regions on the vehicle depicting tied contacts

- *CONTACT_AUTOMATIC_NODES_TO_SURFACE (Appendix A) is used to model the interaction between the armor and the space frame where they are not physically connected. Fourteen regions of these contacts are included in the model, Figure 2.14.

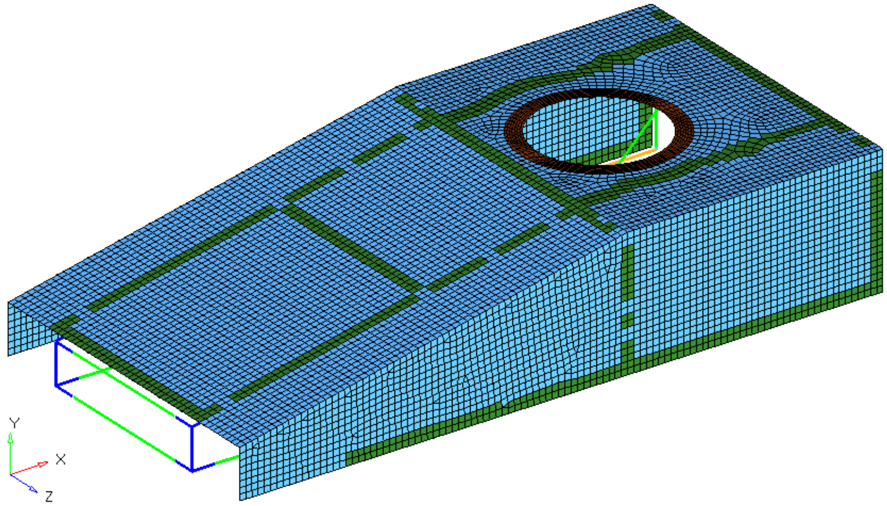

Figure 2.14: Automatic surface contact locations on the vehicle

2.7.2 Constraints

The vehicle, in general, is in contact with the ground through the wheels when subjected to impact load. This type of boundary condition will result in diverting a portion of the impact energy as kinetic energy. Therefore, it was decided to fix some locations on the vehicle to study its performance under a situation when it will absorb all of the impact energy. Four nodes on the internal space frame were selected and fixed completely. These four nodes represent the four corners at the back-end of the space frame shown in Figure 2.15.

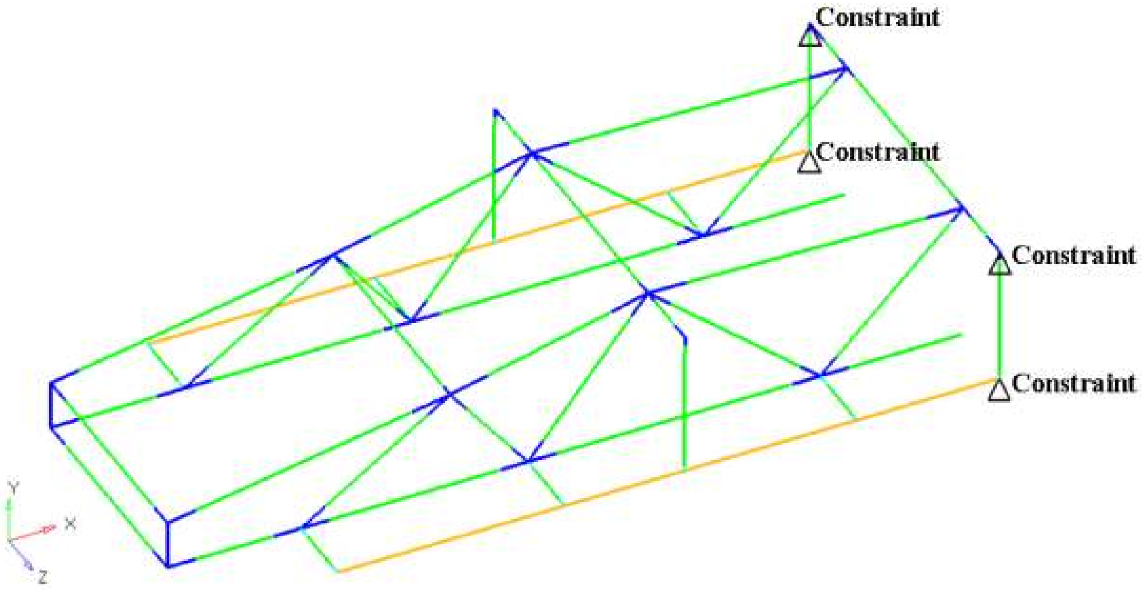

Figure 2.15: Locations or nodes on the space frame rigidly constrained

2.7.3 Loading Conditions

The vehicle is subjected to projectile impact loading on the side wall, Figure 2.16. The projectile impact location was chosen to be closer to the front of the vehicle to increase the bending effect due to the fixed-displacement boundary conditions at the rear.

This force impact curve is a smooth, simplified load curve approximately equivalent to force resulting from the momentum of a projectile of mass 0.8 kg hitting the side of the vehicle with an initial velocity of 938 m/s over 0.25 ms. It is assumed that the mass of the projectile is steadily disappearing through the loading phase and the force is increasing linearly. The calculations result in a peak load of 600 kN. The load curve goes back to zero linearly over 8.05 ms. The duration of the impact load and the FE model run time is 8.4 ms. The loading curve is shown in Figure 2.17.

The total computational time for this FE model with the aforementioned boundary conditions is approximately five minutes.

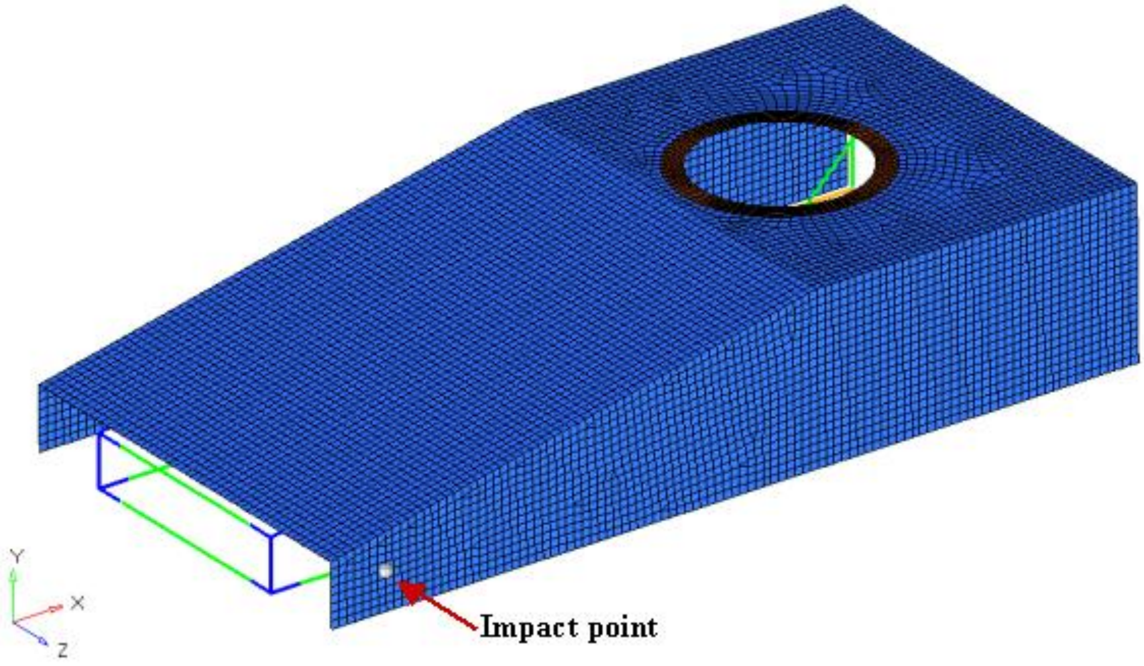

Figure 2.16: Side projectile impact location

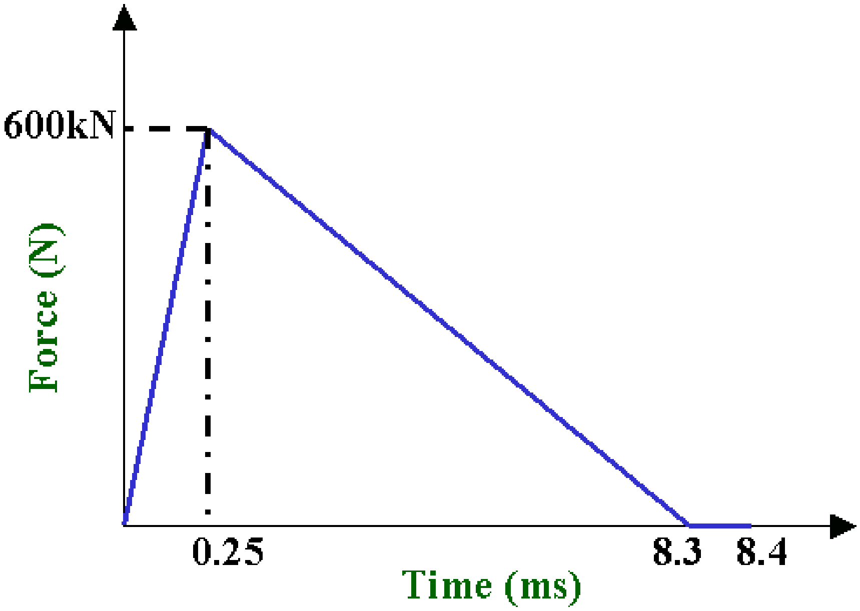

Figure 2.17: Triangular impact impulse of the projectile

CHAPTER 3

OPTIMIZATION

Optimization can be defined as the procedure for achieving the most desirable design of any product. Optimization is predominantly iterative and hence a series of operations are performed sequentially to obtain the optimal result. In the past, optimization of a product was done manually. This made the optimization process very tedious and time consuming, and hence the field was very limited. But with the advancement of technology and advent of computers, there is more scope available for optimization. With regard to space frames optimization, there has been active research in minimizing the weight, as was noticeable from the literature survey listed in Chapter 1. The research in the area of military vehicle space frame optimization is minimal and mostly classified. Optimization can be an important tool for the military vehicle and its internal space frame structure to minimize the overall mass, which can be an essential aspect for the mobility of the vehicle in transport and frontline. The structural integrity of the vehicle can be improved with the help of optimization technique. This can lead to mitigating shock in the vehicle due to projectile hits or explosive loads. The objectives of this chapter are,

- To propose and validate an optimization technique for the military vehicle and the internal space frame structure.
- To minimize the mass of the military vehicle.
- To reduce the shock at identified critical locations on the space frame structure.

The FE model of the military vehicle with its internal space frame detailed in Chapter 2, Figure 3.1, is taken as the base model for conducting optimization studies. This model is most suitable for the iterative optimization procedure due to its combination of accuracy, computational efficiency and modeling simplicity.

Figure 3.1: FE model of the vehicle with the internal space frame

3.1 Mass Optimization

3.1.1 Problem Description

The objective of this optimization process is to reduce the mass of the vehicle by minimizing the mass of the components of the internal space frame structure and the outer armor. This is obtained by varying the cross-sectional parameters of the space frame components and the thickness of the armor, while maintaining its structural integrity. Previous optimization study explored the effect of varying joint locations on the mass of the vehicle [51]. This study showed that moving *joint 5*, Figure 3.2, in increments between *joint 4* and *joint 10* along the x-direction resulted in a negligible change in vehicle mass (less than 0.03%). Therefore, it is decided not to include varying the joint locations as a design variable for optimization.

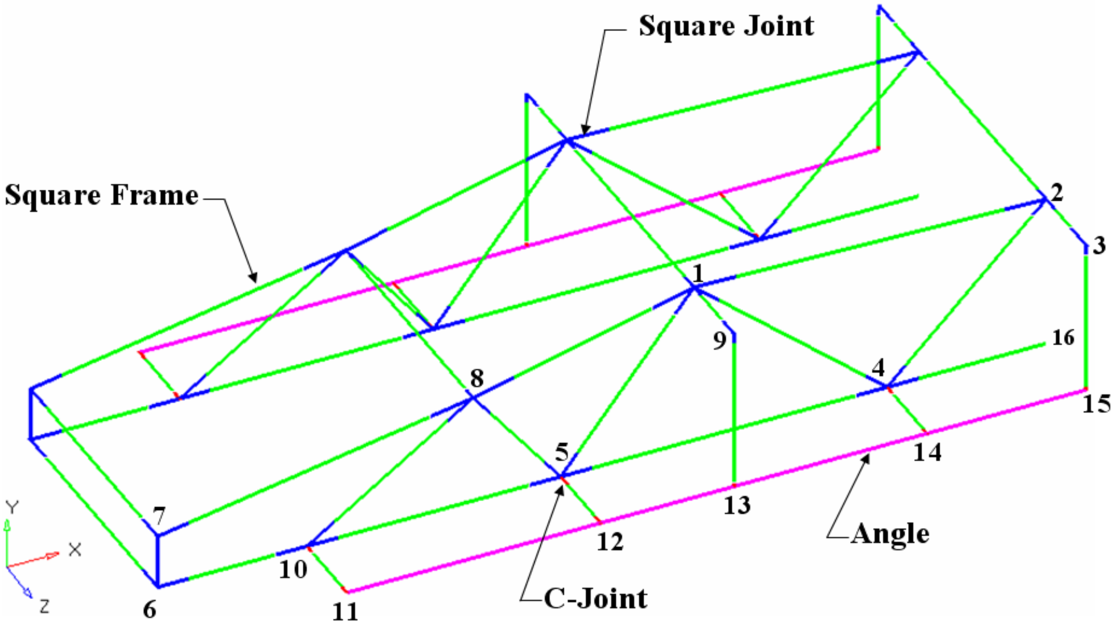

Figure 3.2: Internal space frame structure of the military vehicle

3.1.2 Parameterization of the FE Model

Five independent variables that describe the various cross-sections of the frame members and joints, Figure 3.3, are considered for the optimization,

- x_1: wall thickness of the frame members.
- x_2: inner height of the frame members.
- x_3: wall thickness of the angle member.
- x_4: wall thickness of the C-joints.
- x_5: wall thickness of the joints.

A sixth independent variable is considered,

- x_6: thickness of the armor plate.

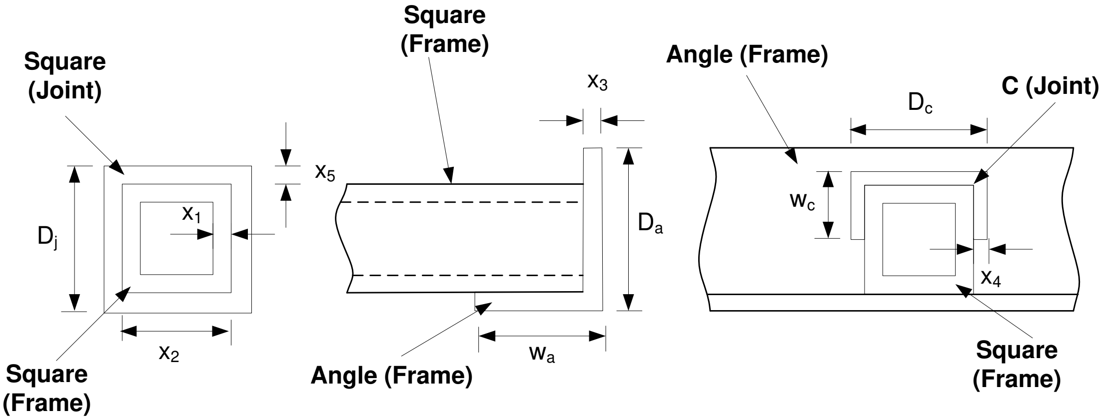

Figure 3.3: Parameterization of the space frame sections for mass optimization

The thickness of the armor around the turret is kept fixed. The dependent variables of the cross-sectional dimensions of the frame and joints components of the space frame are given in Equation 3.1 below (dimensions are in meters). A 12.7 mm extension is used for w_a and w_c in Figure 3.3 to allow space for bolting the angle and the C-joint to the other frame members.

$$\begin{aligned}
D_f &= x_2 + 2x_1 \\
D_j &= x_2 + 2x_1 + 2x_5 \\
D_a &= x_2 + 2x_1 + x_3 \\
w_a &= 0.0127 + x_3 \\
D_c &= x_2 + 2x_1 + 2x_4 \\
w_c &= 0.0127 + x_4
\end{aligned} \tag{3.1}$$

The mass of any frame member or joint is given as,

$$M_{i,j} = \rho[LN_{i,j}AB_{i,j} + LN_{j,i}AB_{j,i} + (L_{i,j} - LN_{i,j} - LN_{j,i})A_{i,j}] \tag{3.2}$$

where,

$M_{i,j}$	mass of frame member or joint branches connecting *joint i* to *joint j* (kg)
ρ	mass density of frame members and joints (kg/m^3)
$LN_{i,j}$	length of joint branch starting from *joint i* along the line connecting *joint j* (m)
$L_{i,j}$	length of vector connecting *joint i* to *joint j* (m)
$AB_{i,j}$	combined cross-sectional area of the branch connecting *joint i* to *joint j* and the enclosed frame member (m^2)
$A_{i,j}$	cross sectional area of frame members or joints between *joint i* and *joint j* (m^2)

The areas of the frame members and joints are obtained from Table 3.1. The area of the optimized armor portion is computed to be 12.957 m^2 (A_s), which is the total surface area of the vehicle's top and sides minus the turret hole and stiffening portion surrounding it. Therefore, the mass of the vehicle armor is obtained from Equation 3.3,

$$M_{armor} = (A_s)(\rho)(x_6) \tag{3.3}$$

where,

M_{armor}	mass of the outer armor of the military vehicle (kg)
A_s	surface area of the armor (m^2)
ρ	mass density of the armor material (kg/m^3)
x_6	thickness of the outer armor (m)

Table 3.1: Areas of relevant sections (m^2)

Section type	Area equation
Square (Frame)	$4x_1(x_1+x_2)$
Angle (Frame)	$x_3(2x_1+x_2+x_3+0.0127)$
C (Joint)	$x_4(2x_1+x_2+2x_4+0.0254)$
Square (Joint)	$4x_5(2x_1+x_2+x_5)$

3.1.3 Objective Function and Constraints

The objective function is given as,

$$\text{Minimize, } M = M_{armor} + 2M_{11,15} + 2\sum_{j=1}^{16}\sum_{k=1}^{16}\delta_{j,k}M_{j,k} - \sum_{n=1,2,6,7,8} M_{n,n} \tag{3.4}$$

The variable $\delta_{j,k}$ is the reverse Kronecker delta and is defined by Equation 3.5. The second term in Equation 3.4 corresponds to the mass of the two side angle members while the fourth term describes the fact that there are single frame members in the center of the vehicle that start from *joint 6*, *joint 7*, *joint 8*, *joint 1*, and *joint 2*, Figure 3.4.

$$\delta_{j,k} = \begin{cases} 0, & if \;\; j = k \\ 1, & if \;\; j \neq k \end{cases} \tag{3.5}$$

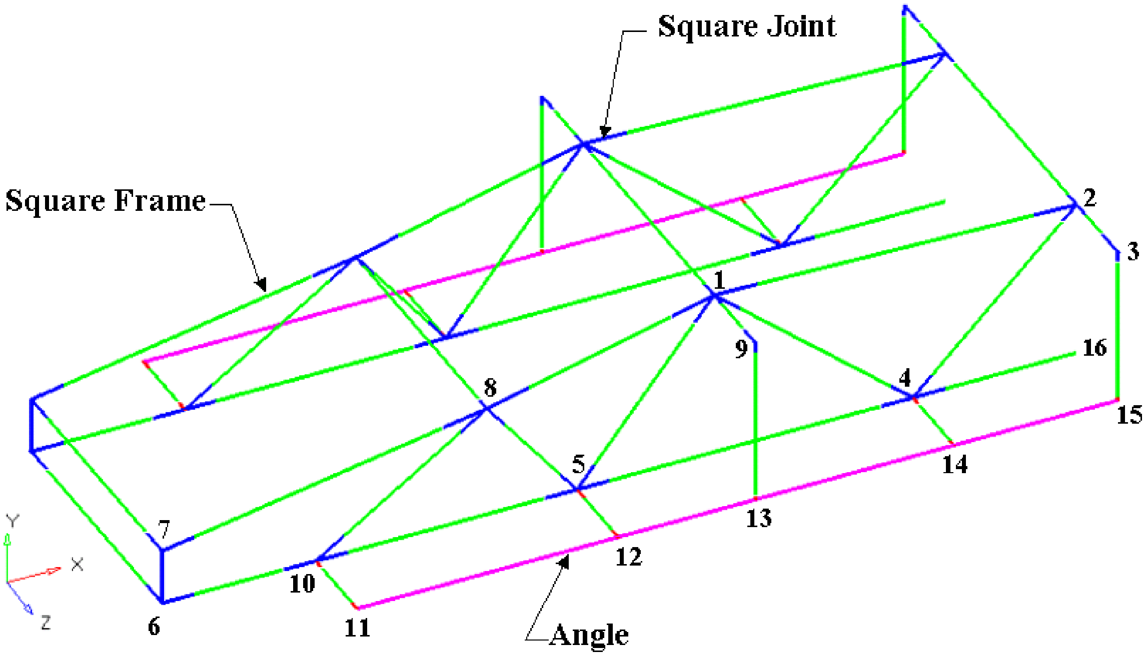

Figure 3.4: Line drawing of the internal space frame structure

Twelve geometric constraints are used to ensure realistic dimensions of the frame and armor by imposing upper and lower limits on the dimensions of the frame members and the armor (all the limits are in meters),

$$
\begin{aligned}
&0.003 \le x_1 \le 0.007 \\
&0.040 \le x_2 \le 0.110 \\
&0.003 \le x_3 \le 0.035 \\
&0.003 \le x_4 \le 0.014 \\
&0.003 \le x_5 \le 0.014 \\
&0.020 \le x_6 \le 0.040
\end{aligned}
\tag{3.6}
$$

Additionally, the stress constraint below, Equation 3.7, ensures that the plastic stress within the vehicle does not exceed a preset value, 110% of yield stress which is 418 MPa, to maintain the structural integrity of the space frame and armor. The stress limit of 418 MPa corresponds to a strain limit of 7.41%, which is slightly more than half the material failure strain, Figure 3.5.

$$\sigma_{\max} = 1.10\sigma_y \tag{3.7}$$

where,

σ_{max} maximum Von Mises stress in the military vehicle (MPa)

σ_y yield stress of the vehicle material (MPa)

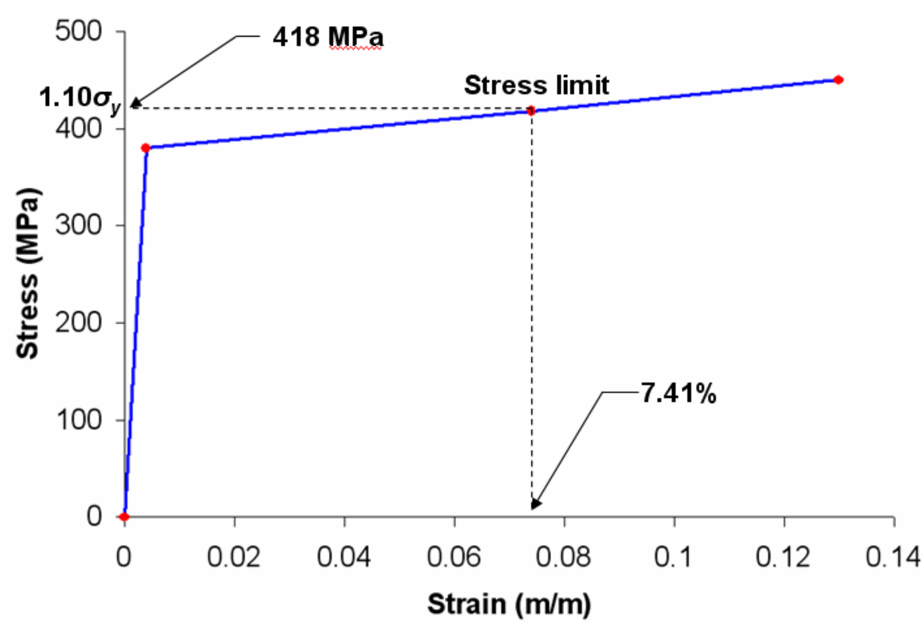

Figure 3.5: Stress-strain curve of aluminum 7039 showing the stress limit

These thirteen constraints are formulated in the standard form,

$$g_i > 0 \tag{3.8}$$

The constraints are incorporated in the objective function by using the penalty function to maintain the search within the feasible region. After including the constraints, the objective function becomes,

$$\text{Minimize, } F = A\left[M_{armor} + 2M_{11,15} + 2\sum_{j=1}^{16}\sum_{k=1}^{16}\delta_{j,k}M_{j,k} - \sum_{n=1,2,6,7,8} M_{n,n}\right] + \sum_{i=1}^{13}\Omega_i \tag{3.9}$$

As the problem is prohibitively expensive, the program starts by evaluating the penalty terms. If any is violated, the finite element program is not assessed and the objective function is assigned a large value,

$$\text{If, } g_i \le 0, \qquad A = 0 \quad \& \qquad \Omega_i = Rg_i^2 + B \tag{3.10}$$

$$\text{If, } g_i > 0, \qquad A = 1 \quad \& \qquad \Omega_i = 0 \tag{3.11}$$

R and B are the penalty parameters that are assigned values of 10^{15} and 600,000 respectively.

3.2 Shock Optimization

3.2.1 Problem Description

Eight locations on the internal space frame structure of the military vehicle, Figure 3.6, are identified as critical for the optimization studies. These points were chosen because they have relatively high accelerations during the simulated projectile impact and they could be mounting locations for critical interior components such as crew seats or control computers. It is decided not to include any node in the immediate vicinity of the impact as this may bias the results. The selected critical locations are:

- Locations on the right side of the space frame, which is subject to the projectile impact (N1, N2, and N3).
- Front hood portion (N7).
- Locations on the left side of the space frame, which is opposite to the projectile impact (N4, N5, N6, and N8).

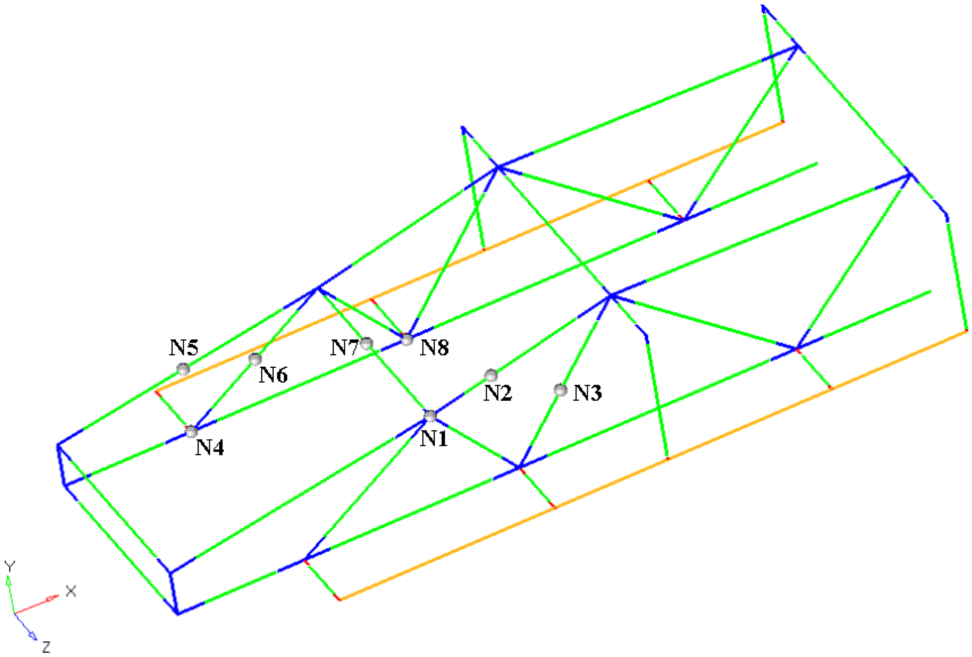

Figure 3.6: Critical locations on the space frame

The chosen locations include both joints (N1, N4, and N8) as well as mid-member locations (N2, N3, N5, N6, and N7). Figure 3.7 shows the unfiltered acceleration profiles at the critical locations for the original vehicle design. The accelerations at the joint locations (N1, N4, and N8) are comparatively less than the frame members, as the joints are acting as a medium to mitigate shock. The locations in the front of the space frame (N5, N6, and N7) exhibit much higher acceleration values than those further away from impact (critical locations N2 and N3). Hence, no location on the middle and back portions of the space frame structure is chosen as critical for optimization study. Also, none of the armor nodes were selected since there are no mounting locations on the armor as it will be subjected directly to the impact.

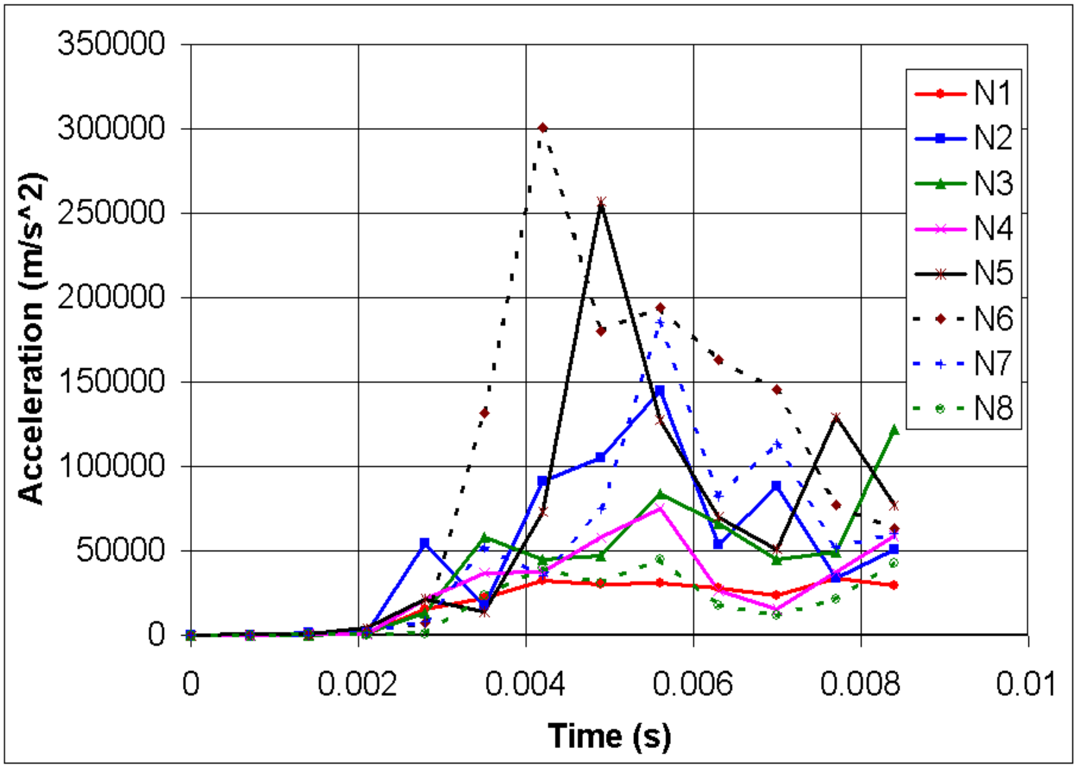

Figure 3.7: Shock profiles at the critical locations for the original vehicle design

The objective of the optimization process is to reduce shock or acceleration profiles of the aforementioned critical nodes on the space frame. This is obtained by varying the cross-sectional parameters of the space frame and the thickness of the armor, while maintaining its structural integrity.

3.2.2 Parameterization of the FE Model

Similar to the mass optimization, based on the space frame sections shown in Figure 3.8, and the armor, six independent variables are considered for optimization,

- x_1: wall thickness of the frame members.
- x_2: inner height of the frame members.
- x_3: wall thickness of the angle member.
- x_4: wall thickness of the C-joints.
- x_5: wall thickness of the joints.
- x_6: thickness of the armor plate.

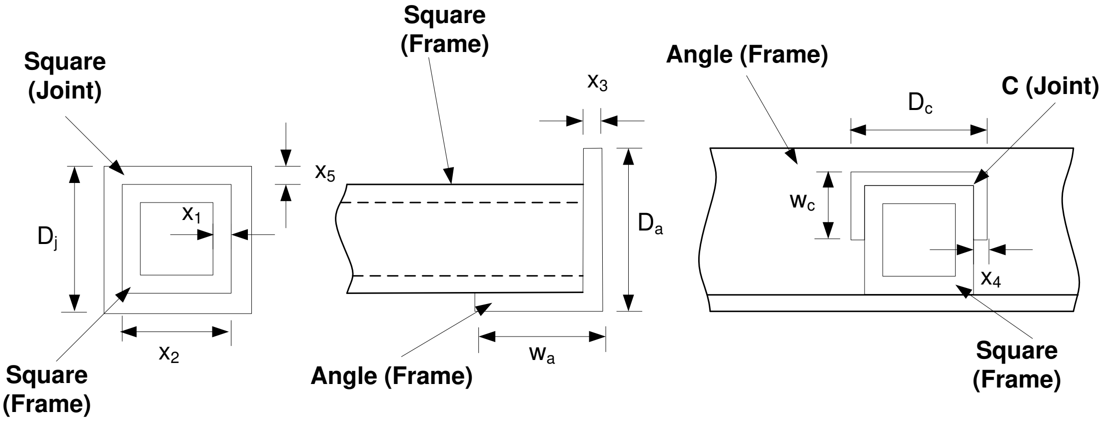

Figure 3.8: Parameterization of space frame components for shock optimization

The dependent variables, like wise to the mass optimization, are as listed in Equation 3.12,

$$\begin{aligned} D_f &= x_2 + 2x_1 \\ D_j &= x_2 + 2x_1 + 2x_5 \\ D_a &= x_2 + 2x_1 + x_3 \\ w_a &= 0.0127 + x_3 \\ D_c &= x_2 + 2x_1 + 2x_4 \\ w_c &= 0.0127 + x_4 \end{aligned} \tag{3.12}$$

3.2.3 Objective Function and Constraints

The objective function for the optimization is given as,

$$\text{Minimize, } S = \frac{\sum_{k=1}^{r} Avg(Nk)}{r} \tag{3.13}$$

where,

S	total mean acceleration of the critical nodes (m/s^2)
Nk	node at a critical location
$Avg(Nk)$	mean of the acceleration profile at node Nk (m/s^2)
r	number of critical locations

Twelve geometric constraints are used to ensure realistic dimensions of the frame and armor by imposing upper and lower limits on the dimensions of the frame members and the armor (all the limits are in meter). Additionally, the stress constraint below ensures that the Von Mises plastic stress within the vehicle does not exceed a preset value to maintain the structural integrity of the space frame and armor.

$$
\begin{aligned}
&0.003 \le x_1 \le 0.007 \\
&0.040 \le x_2 \le 0.110 \\
&0.003 \le x_3 \le 0.035 \\
&0.003 \le x_4 \le 0.014 \\
&0.003 \le x_5 \le 0.014 \\
&0.020 \le x_6 \le 0.040
\end{aligned}
\tag{3.14}
$$

$$\sigma_{\max} = 1.10\sigma_y \tag{3.15}$$

These thirteen constraints are formulated in the standard form similar to the mass optimization, Equation 3.8. The constraints are incorporated in the objective function by using the penalty function to maintain the search within the feasible region. After including the constraints, the objective function becomes,

$$\text{Minimize, } T = A\left[\frac{\sum_{k=1}^{r} Avg(Nk)}{r}\right] + \sum_{i=1}^{13}\Omega_i \tag{3.16}$$

As the problem is prohibitively computationally expensive, the program starts by evaluating the penalty terms. If any is violated, the finite element program is not assessed and the objective function is assigned a large value,

$$\text{If, } g_i \le 0, \qquad A = 0 \quad \& \qquad \Omega_i = Rg_i^2 + B \tag{3.17}$$

$$\text{If, } g_i > 0, \qquad A = 1 \quad \& \qquad \Omega_i = 0 \tag{3.18}$$

R and *B* are the penalty parameters that are assigned values of 10^{15} and 600,000 respectively, in order to assign the objective functions large values when the constraints are violated.

3.3 Organization of the FE code

LS-DYNA has the capability to write the finite element model input file in text format. The optimization code, which is written in MATLAB v2006a, is coupled with the LS-DYNA input file to run the simulation of the vessel in an iterative procedure. The entire optimization process is conducted within the MATLAB environment. The FE model of the vehicle, written in text format within MATLAB, is divided into fixed and variable code portions.

3.3.1 Fixed Code

This code comprises of all the features of the FE model that remain constant irrespective of changes in the values of the design variables. Fixed code contains components such as, nodal coordinates, element connectivity information, and material properties.

3.3.2 Variable Code

This portion of the FE code depends on the design variables. Variable code comprises of the cross-sectional properties of the space frame structure and armor plate shell elements. The variable code text is generated by the optimization program according to the values of the optimization variables.

3.4 Optimization Process

To obtain the function value at any point, the independent variables are used to create the variable FE code of the vehicle, which is added to the fixed code to form the FE input file. This input file is processed in LS-DYNA through MATLAB environment. The computational time for processing the input file is approximately five minutes. The element output file obtained from computing the input file is then read within MATLAB to calculate the Von Mises stresses, acceleration profiles at the critical locations (for shock optimization), and the objective function. This procedure roughly takes 10 minutes of the computing processor time. Hence, the total computational time for one function evaluation is approximately 15 minutes.

3.5 Optimization Algorithm

The vehicle space frame optimization problem is solved using the Successive Heuristic Quadratic Approximation (SHQA) algorithm [55]. This method was developed to reduce stress corrosion cracking effects in cylindrical containers by maximizing the compressive stress on the outer surface of the closure weld region. SHQA improved the resultant compressive hoop stress by 126% in comparison to the original design. SHQA provided results that were better than those of an off-the-shelf optimization program as well as the successive quadratic approximation.

SHQA optimizes designs of computationally intensive problems with large number of variables. This method combines successive quadratic approximation with a controlled random search. If the problem is almost quadratic, the quadratic approximation will improve the search quickly. The controlled random search is an effective tool for highly nonlinear problems.

The following is a brief overview of the optimization process. At the initial step, upper and lower bounds, L_j and U_j, of the previous section are used. Within these bounds, m initial points are generated using s equally-spaced values for the n design variables. The newly created variable code is added to the fixed FE code to form the FE input file of the vehicle. This input file is processed in LS-DYNA and the objective function is computed. The element output file is read and the Von Mises stresses are evaluated. The objective function and the variables are fed back into the SHQA algorithm. This process is repeated for all the m points. A quadratic polynomial is fitted to these data points. The minimum point of the quadratic surface is determined numerically. This solution is then input into the finite element software to obtain the objective function value for this point. This point is added to the m points already generated.

The K points in the lower half of the function value range are identified. New upper and lower bounds of the design variables that enclose these points are identified. These bounds are expanded by a factor α to avoid over-constraining the search. The minimum function value point of the quadratic curve fitting is added if it belongs to the lower half of the function value range. Additional $m+1-K$ data points are randomly generated. The finite element program calculates the function values of these points. These $m+1-K$ data points replace the ones that were in the upper half of the function value range of the previous iteration.

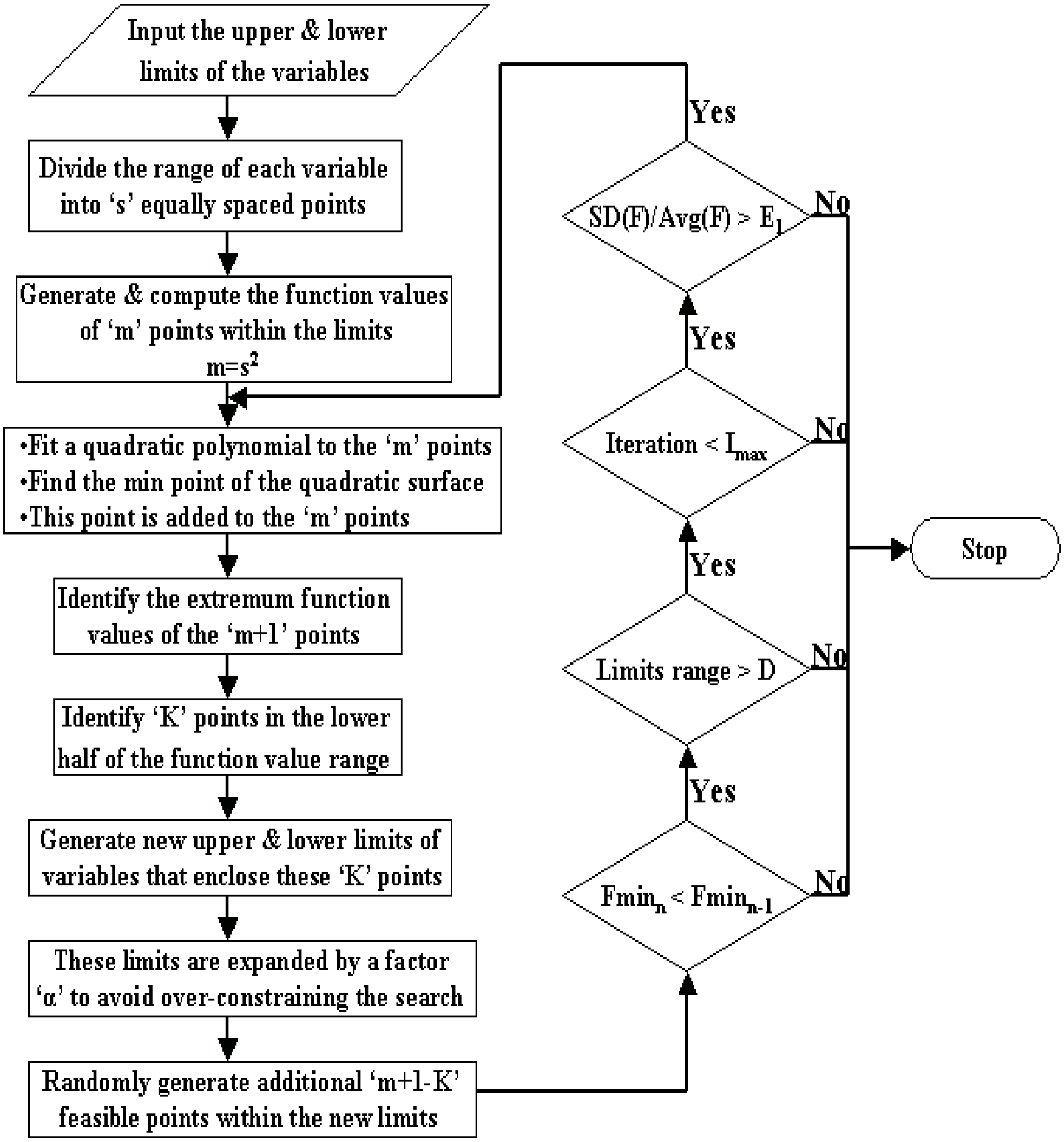

Figure 3.9: Flowchart of the optimization process

The algorithm has the following set of criteria to terminate the optimization process:

- The minimum function value in the current iteration ($Fmin_n$) is greater than the minimum function value of the previous iteration ($Fmin_{n-1}$).
- The ranges of all the independent variables are less than the specified accuracy (D).
- The maximum iteration limit (I_{max}) is reached.
- The ratio of the standard deviation (SD) of the function values to their average (Avg) function value is less than a predetermined function closeness parameter (E_1).

The entire optimization problem is solved in the MATLAB environment. Figure 3.9 depicts the flowchart of the optimization algorithm while Table 3.2 shows the SHQA parameters defined for this problem.

Table 3.2: SHQA input parameters

Parameter	Mass	Shock
No. of independent variables, n	6	6
No. of equal size spaces between data points, s	7	7
No. of initial data points, m	49	49
Factor of expansion for the range of variables, α	5e-2	5e-2
Maximum no. of iterations, Imax	2500	1000
Function value closeness parameter, E_1	1e-5	1e-3
Specified accuracy of the variables, D	1e-6	1e-6

3.6 Results

3.6.1 Mass Optimization

The optimization algorithm underwent 9817 function evaluations and 2215 iterations. The total optimization process approximately took 580 hours of computational time. The optimization process was terminated as the function value closeness parameter was reached. The results of the design variables from the optimization process are compared with the original design values in Table 3.3. All the variables, except x_6, reach the lower limits.

Table 3.3: Comparison of the variables before and after mass optimization (mm)

Parameters	Original design	Final design	Lower limit	Upper limit
x_1	6.4	3.0	3	7
x_2	57.2	40.0	40	110
x_3	15.9	3.0	3	35
x_4	12.7	3.0	3	14
x_5	12.7	3.0	3	14
x_6	32.0	28.0	20	40

An off-the-shelf optimization program was also used [Appendix B], but obtained results were poor and the off-the-shelf program was inadequate to handle the mass optimization problem. The neighborhood of the optimized design parameter x_6 was surveyed [Appendix C]. The results indicated that no neighboring point provided a better value.

Table 3.4 compares the objective function in the original and final designs. The table also lists maximum Von Mises stress values in the space frame structure and armor for these two cases. Figure 3.10, stress contour plot, shows the maximum Von Mises stress occurring at the location of impact on the armor. Due to the nature of the impact location the highest stresses are localized at the side of the vehicle and the angle frame member, located at the side of the vehicle. As expected these areas absorb most of the impact energy. While the mass of the space frame is reduced by 77%, the mass of the armor is reduced by 13%. This reduction is accompanied by an increase in armor and space frame Von Mises stresses, by 5% and 3% respectively. The results indicate that stresses in the armor and space frame are in the plastic range. Also, the armor stress has reached the stress constraint of 418 MPa, hence preventing the design variable x_6 from further reducing towards the lower limit. The overall mass of the vehicle is reduced by 25%. With this reduction in the vehicle mass, the increase in the vehicle stresses is still considerably below the failure limit of the material (450 MPa), therefore maintaining the structural integrity of the vehicle.

Table 3.4: Comparison between the optimized and original results

Parameters		Original design	Final design	% change
Mass (kg)	Armor	1119.50	979.73	-12.5
	Space frame	263.46	58.98	-77.6
Total mass (kg)		1382.96	1038.71	-24.7
Max stress (MPa)	Armor	397.14	417.97	+5.2
	Space frame	392.92	406.15	+3.4

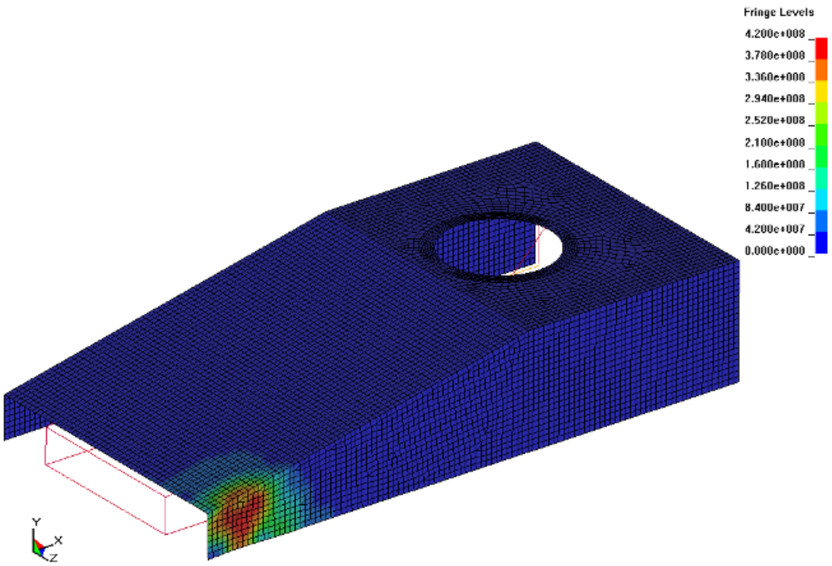

Figure 3.10: Maximum Von Mises stress contour plot for side impact

3.6.1.1Front Impact

As the vehicle can be subject to various impact locations, it may be of use to study the behavior of the optimized vehicle under different loading scenarios. The optimized military vehicle is subjected to a projectile impact on the front hood of the vehicle, Figure 3.11. The same loading time-history for side impact is applied for the front impact, Figure 3.12.

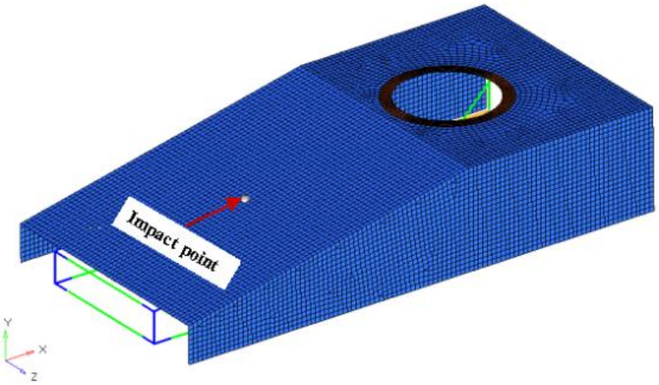

Figure 3.11: Front impact location

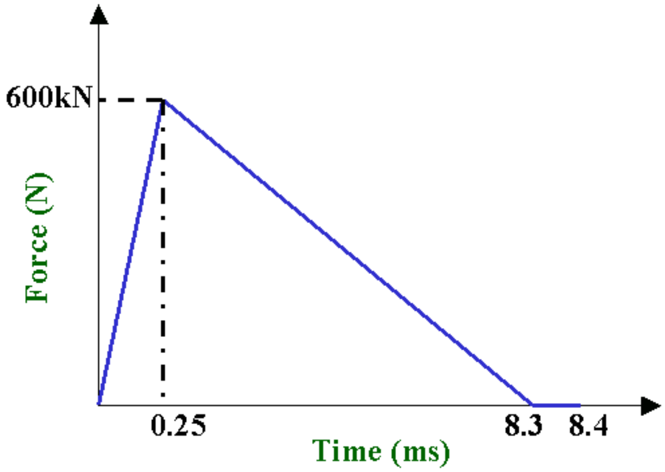

Figure 3.12: Triangular impact impulse of the projectile

The results of the front impact are shown in Table 3.5. As in the side impact case, the final design of the armor experiences increase in the maximum Von Mises stress when compared to the original design. The stress values in the space frame are almost maintained the same. The maximum stress for the space frame occurs at the back end of the structure where the frame is rigidly constrained. The impact load results in pushing the vehicle backwards, but the constraints at the back end of the space frame resist this movement and hence results in higher stressed region at the constraint locations. The stresses at the front impact location are much lesser as the impact load in this case is distributed more evenly over the entire space frame structure. Overall, there is a 17% increase of maximum Von Mises stress for the armor while for the space frame there is a miniscule decrease of 0.3%. Figure 3.13, stress contour plot, shows the region of maximum Von Mises stress on the vehicle. From the side and front impact scenarios it can be concluded that the optimized design of the vehicle is functional of different loading conditions.

Table 3.5: Stress results for the front impact case

Parameters		Original design	Final design	% change
Max stress (MPa)	Armor	252.66	295.78	+17.1
	Space frame	382.62	381.38	-0.3

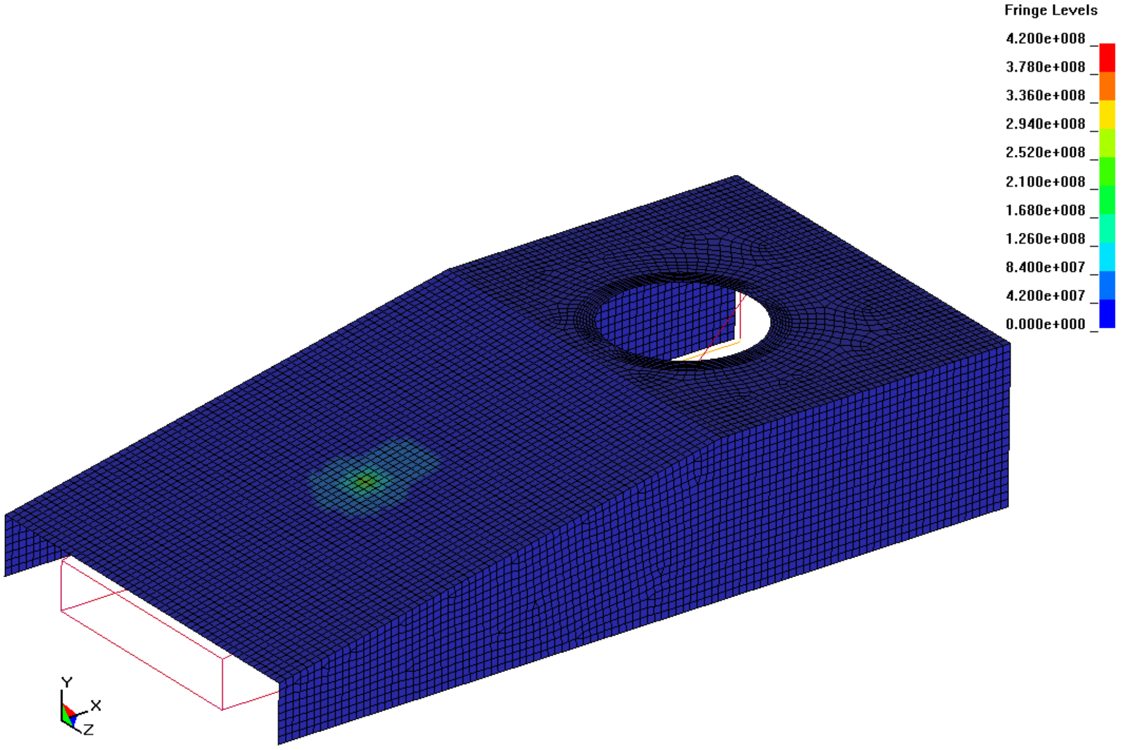

Figure 3.13: Maximum Von Mises stress contour plot for front impact

3.6.2 Shock Optimization

The optimization algorithm underwent 2960 function evaluations and 792 iterations. The total optimization process took 145 hours of computational time. The optimization process was terminated as the function value closeness parameter was reached. The results of the optimization process are compared with the original design values in Table 3.6. Unlike mass optimization, it is interesting to note, the search does not stop at any of the upper or lower limits of the variables. The optimized point was checked for optimality by surveying the neighboring points [Appendix D]. This did not result in a better point.

Table 3.6: Change in the variable values after optimization for shock optimization

Parameters	Original design	Final design	Lower limit	Upper limit
x_1	6.4	5.6	3	7
x_2	57.2	40.1	40	110
x_3	15.9	20.2	3	35
x_4	12.7	4.1	3	14
x_5	12.7	9.8	3	14
x_6	32.0	38.2	20	40

Similar to mass optimization, an off-the-shelf optimization program was also used [Appendix E], but the results obtained were poorer than SHQA results. Hence, it was concluded that the off-the-shelf program was inadequate for shock optimization of the military vehicle.

The stress contour plot in Figure 3.14 shows the maximum Von Mises stress on the armor. Due to the nature of the impact location the highest stresses are localized on the side of the vehicle, especially on the impact side angle frame member. The stresses in the armor are maintained just below the yield strength of the material while the space frame structure undergoes plastic deformation The optimization makes the armor lot more stiffer which significantly contributes in the reduction of the front end displacement of the vehicle, from 26 mm for the original design to 18 mm after optimization.

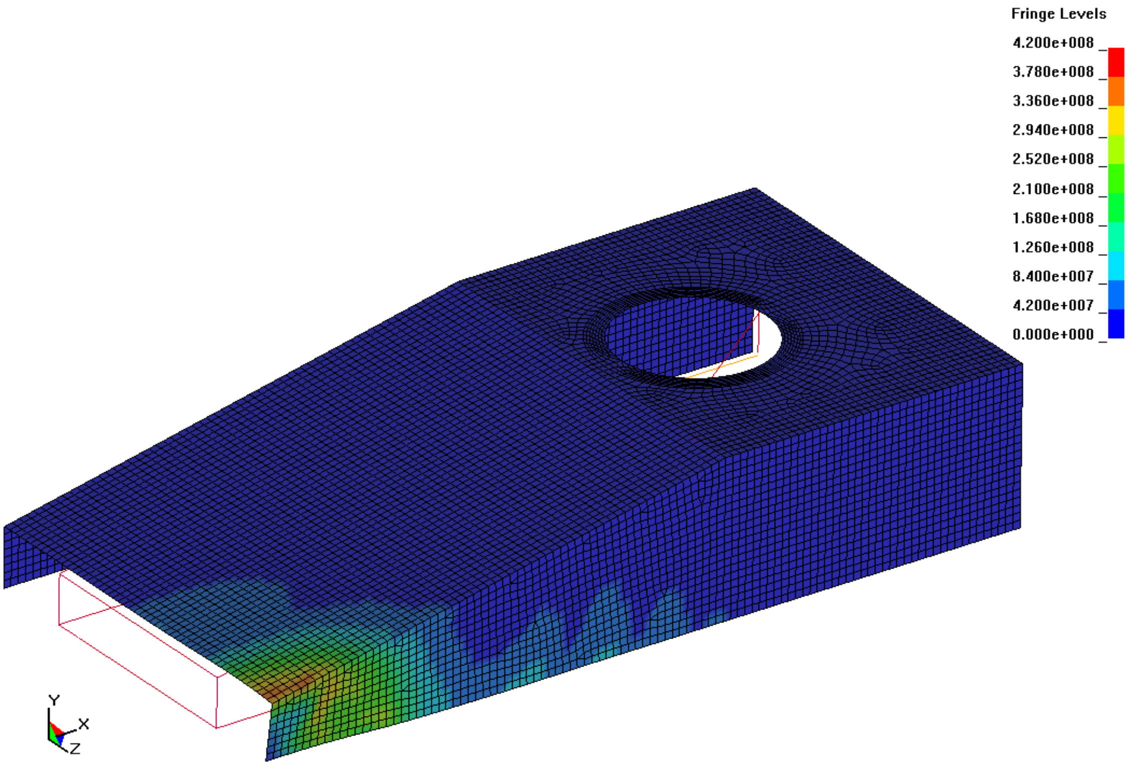

Figure 3.14: Maximum Von Mises stress contour plot after shock optimization

Table 3.7 compares the objective function in the original and final designs. The table also lists maximum Von Mises stress values in the space frame structure and armor for these two cases. A comparison of the original and final designs leads to the following observations:

- The total mean acceleration, *S*, obtained from the considered critical nodes is significantly reduced, by 95%, while there is a 9% increase in the overall mass of the vehicle
- The final design results in significant change in the area moment of inertia of the frame members (1.11E6 mm^4 in the original design versus 0.36E6 mm^4 in the final design). This makes the frame less stiff, hence allowing more energy absorption by the space frame structure.
- A joint wall thickness acts as medium of shock transmission between adjacent frame members. The optimization search results in reducing the wall thicknesses, x_4 and x_5, by more than 20%, which makes the joints less stiff than in the original design. The change also allows for increased absorption of shock by the joints.
- The angle member near the impact point experiences the maximum Von Mises stress In the final design, the wall thickness of the angle members, x_3, are slightly increased, which results in greater shock distribution along the length of the angle members and hence a reduction in the maximum stress value.
- There is a 35% decrease in the overall mass of the space frame so as to make the structure softer and hence result in more energy absorption. Since no locations on the armor were considered critical for shock reduction there is 19% increase in the mass of the armor which in turn results in making the armor stiffer and hence maintaining the overall integrity of the vehicle.

Table 3.7: Shock optimization results

Parameters		Original design	Final design	% change
Mass (kg)	Armor	1119.50	1335.70	+19.3
	Space frame	263.46	172.10	-34.7
Max stress (MPa)	Armor	397.14	373.82	-5.9
	Space frame	392.92	383.42	-2.4
Max displacement (mm)		26.00	18.00	-50.0
Total mean acceleration (m/s^2)		46,109.00	2,479.70	-94.6

Figure 3.15 and Figure 3.16 show the acceleration profiles before and after optimization for the critical locations. At all the locations the shocks are significantly reduced when compared to the original design shock profiles. Figure 3.17 compares the mean acceleration profile of the critical locations for the original design and the result obtained after optimization. The plot clearly depicts the significant reduction in the shock due to optimization.

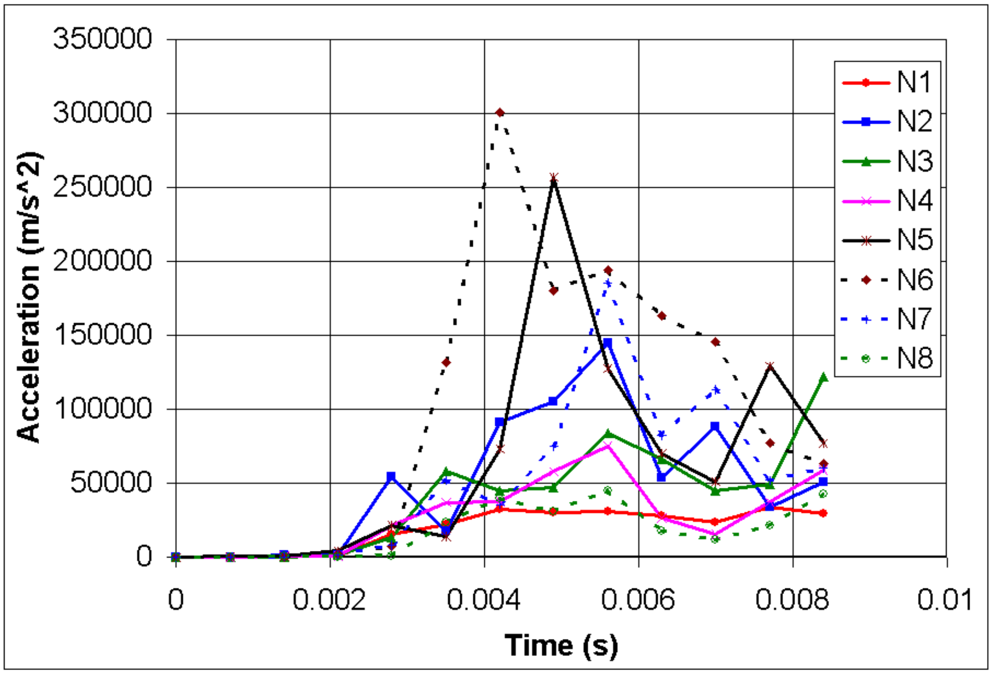

Figure 3.15: Shock profiles at the critical locations before optimization

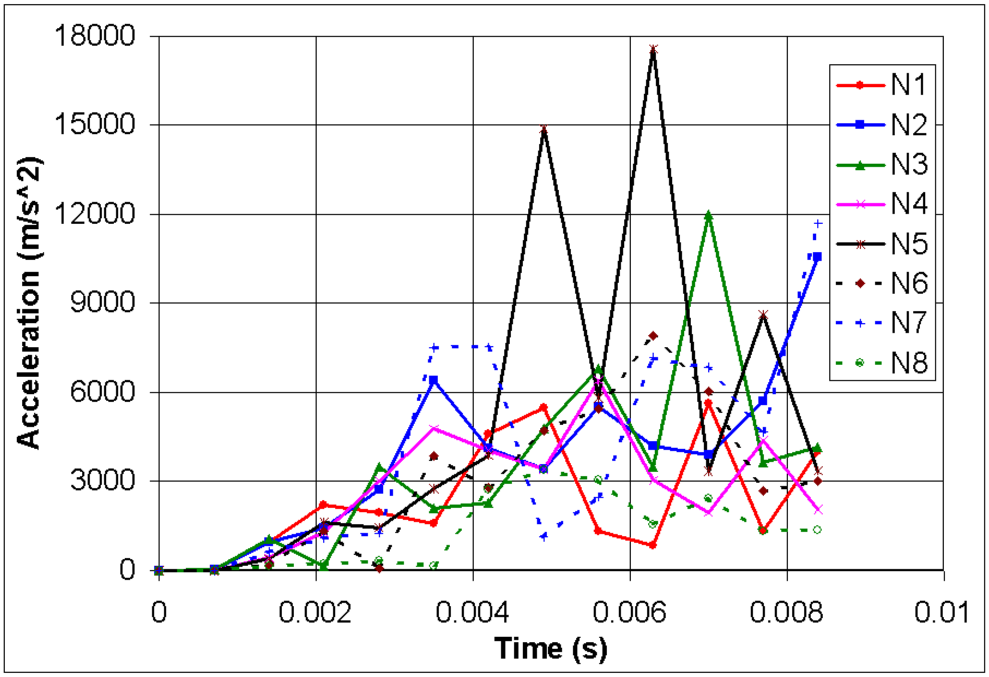

Figure 3.16: Shock profiles at the critical locations after optimization

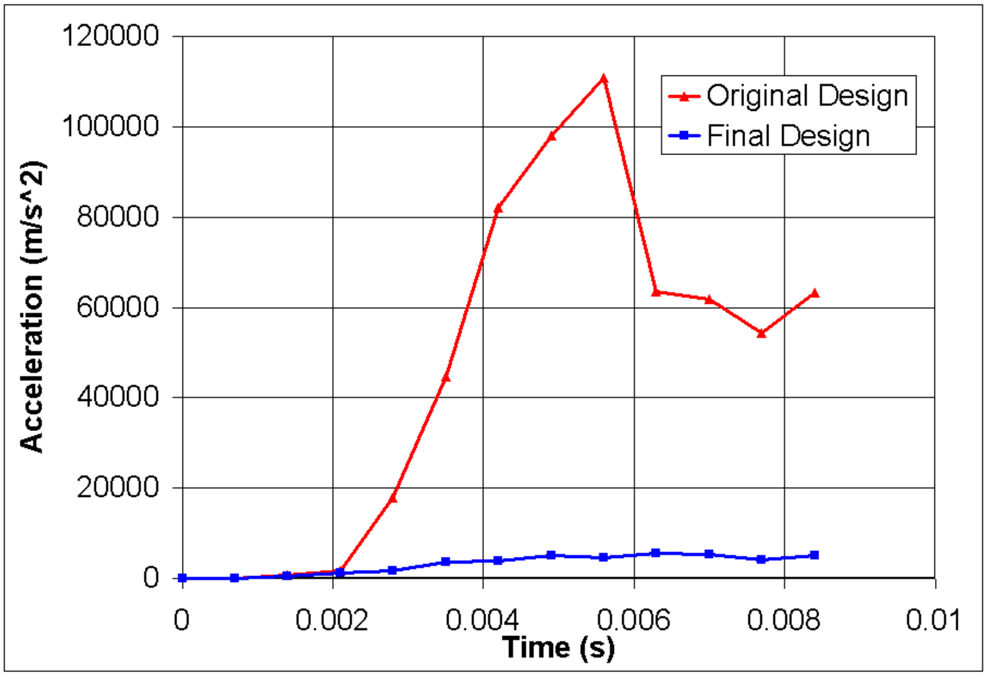

Figure 3.17: Mean shock profile for the original design and after optimization

3.6.2.1 Front Impact

Similar to the mass optimization, the shock optimized design parameters are applied to the vehicle and a front impact case, as shown in Figure 3.18, is considered. The same loading time-history for side impact is applied for the front impact, Figure 3.19.

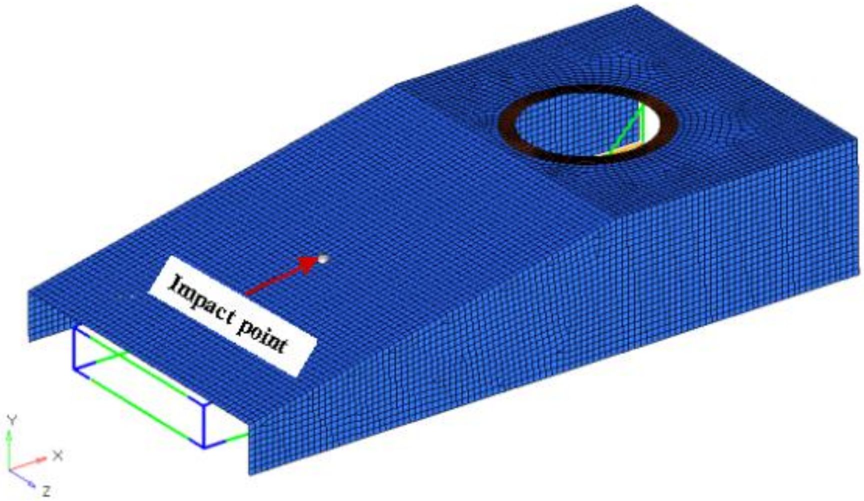

Figure 3.18: Front impact location

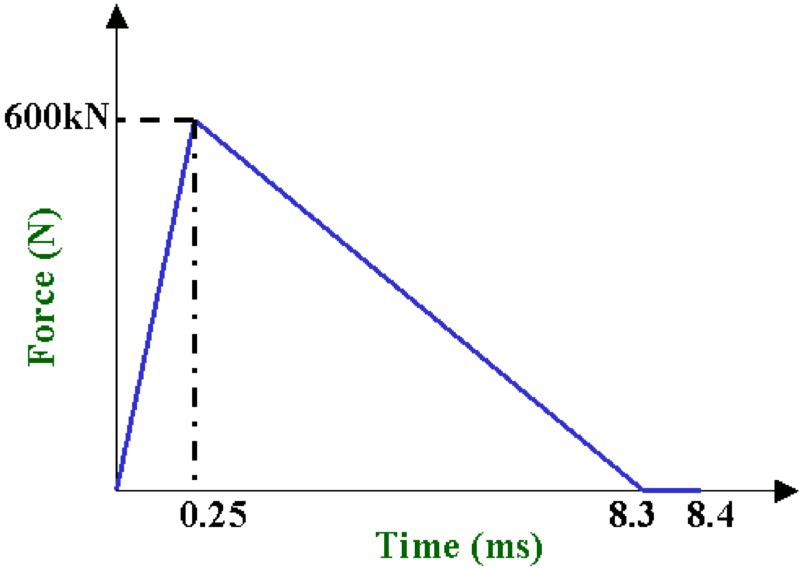

Figure 3.19: Triangular impact impulse of the projectile

The results of the front impact are shown in Table 3.5. There is decrease in the maximum stress values for both the armor, considerably, and space frame structure, miniscule, due to the significant increase in the mass of the armor. This shows that the front impact case is a function of the armor behavior, while the side impact is more dependants on the space frame structure. Figure 3.20 shows a maximum armor stress contour plot and it is clear that this impact scenario is less critical that the side hit.

Table 3.8: Stress results for the front impact case

Parameters		Original design	Final design	% change
Max stress (MPa)	Armor	252.66	205.87	-18.5
	Space frame	382.62	380.98	-0.4

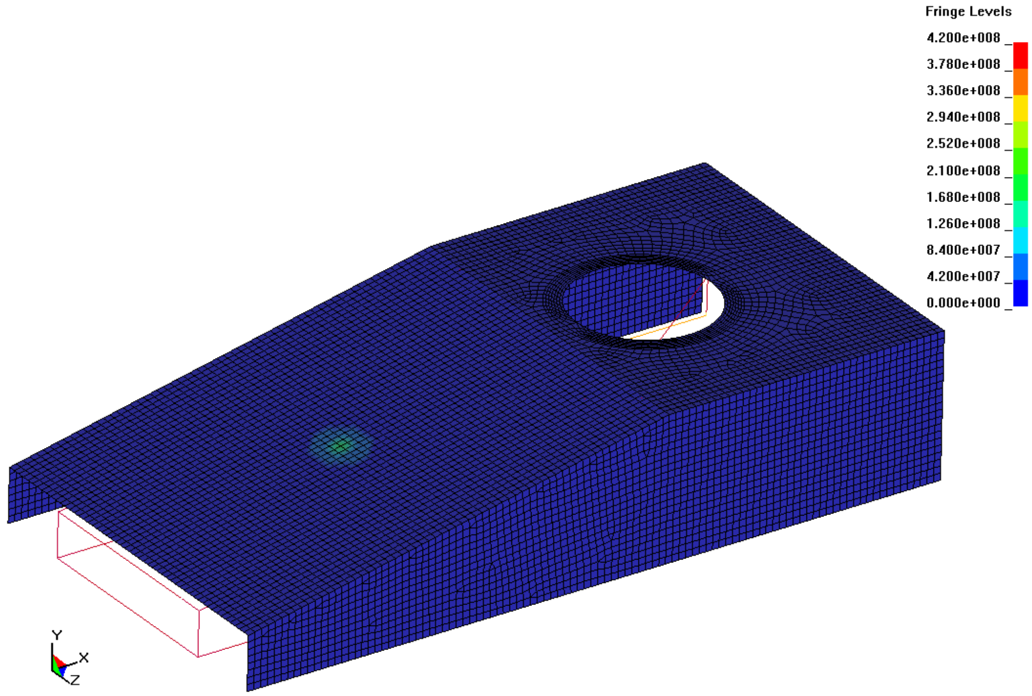

Figure 3.20: Maximum Von Mises stress contour plot for front impact

3.7 Conclusion

From the literature survey it is evident that the area involving the optimization studies regarding military vehicle and its space frame structures is very limited. There is a need for designing an optimization technique for military vehicles which are subjected to more robust loading scenarios such as projectile hits, mine blast, etc., and this research lays a platform for such a study. This chapter proposes an optimization technique and also validates it by conducting two types of optimization case studies.

The objective of the first study involved minimizing the overall mass of the military vehicle, including the internal space frame structure. The second study dealt with reducing the shock or acceleration profiles at identified critical locations on the internal space frame structure. For the case studies the FE model of the military vehicle and the internal space frame structure, detailed in Chapter 2, is parameterized. The cross-sectional parameters of the internal space frame components and the outer armor are chosen as the design variables for the optimization process. The structural integrity of the vehicle is maintained when conducting the optimization studies. Successive Heuristic Quadratic Algorithm (SHQA) [58] is utilized to solve the optimization problem. This algorithm combines successive quadratic approximation with a controlled random search. SHQA is suitable for computationally intensive and highly non-linear problems.

The mass optimization results showed 25% decrease in the overall mass of the vehicle when compared to the original design. For shock optimization there was a 9% increase in the overall mass of the vehicle, while the decrease in overall shock was 95%. These significant decreases in the objective functions of the optimization processes resulted in acceptable limits of changes in the Von Mises stress, displacement and area moment of inertia for the space frame structure and armor, thus maintaining the structural integrity of the vehicle. The SHQA algorithm was found to be computationally expensive for the optimization problem presented in this paper but very productive in reaching the objective. Hence, the optimization technique proposed in this chapter for military vehicles subjected to high impact loads is validated.

CHAPTER 4

LAB-SCALE SPACE FRAME

The works described in the previous chapters were all computational. Currently, limited research is available in assessing the adequacy of the finite element codes in modeling shock loading across structures with joints, such as the military vehicle space frame structure. Hence, it was decided to build a lab-scale space frame structure comprising of joints similar in shape to the military vehicle space frame joints. This lab-scale space frame structure is subjected to impact tests and the obtained results are compared with the simulated predictions. The objectives of this chapter are:

- Design and build a lab-scale space frame structure.
- Conduct shock transmission studies.
- Create FE model of the lab-scale structure.
- Compare FE results with the experimental data for frequency response and accelerations at strategic points.

4.1 Description

The lab-scale space frame structure is derived from the military vehicle space frame. It was decided to make the lab-scale space frame as a cube shaped structure so that during shock studies all the three global directions (x, y and z) can be considered similar to the military vehicle. Figure 4.1 shows a 3D model of the cube shaped lab-scale space frame structure. Overall length of the cube is 482.6 mm. The shape of the joint in the lab-scale structure is based on the military vehicle space frame, Figure 4.2. The joints halves are C-shaped sections, which are bolted together through the hollow square sectioned frame members.

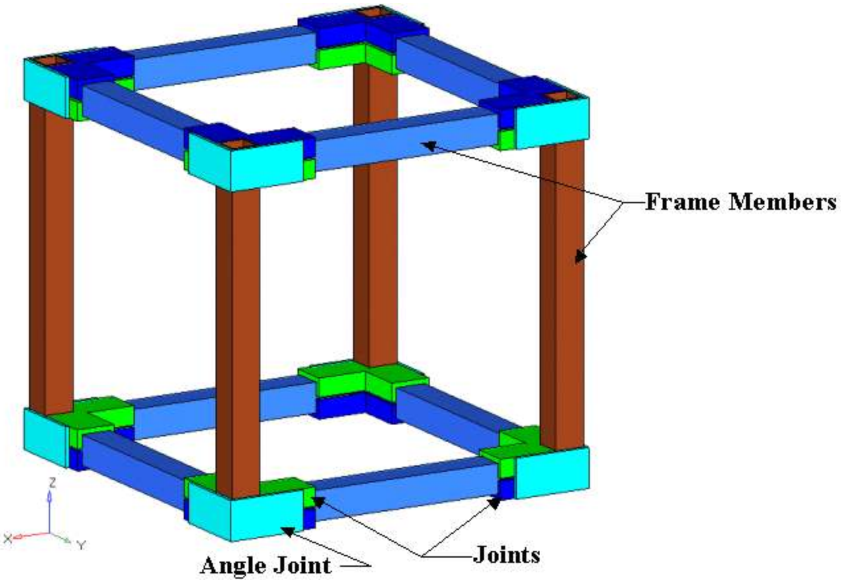

Figure 4.1: Model of the lab-scale space frame structure

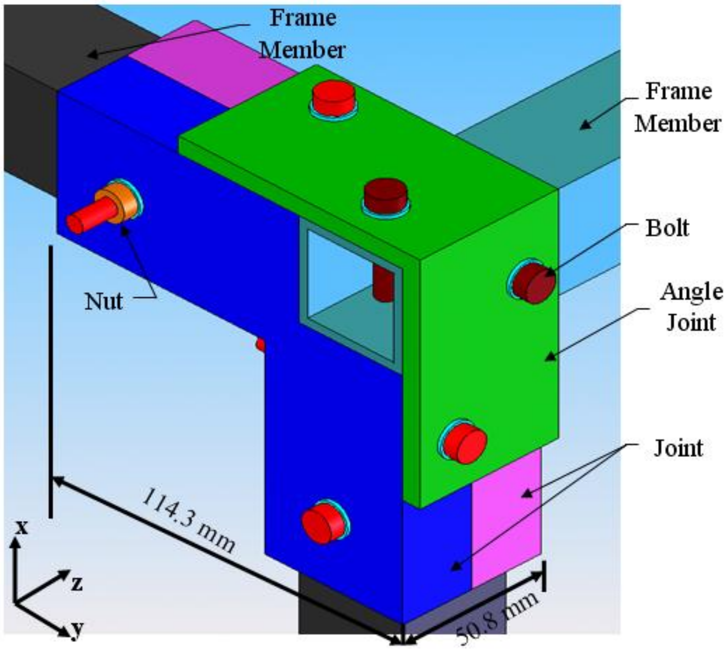

Figure 4.2: Model of the joint on the lab-scale space frame structure

Overall, the two orthogonal joint branches measure 114.3 mm, and the width of the joint is 50.8 mm. The wall thickness of the joints is 6.35 mm, while that of the frame members is 3.175 mm. Based on the length, the frame members are of two types. One set of members are 342.9 mm long. The ends of these frame members are housed in the two orthogonal joint branches. The second set of the frame members are 482.6 mm long, and their ends are enclosed by the angle joints. The angle joint legs are 100 mm in length, while the width is 50.8 mm. The wall thickness of the angle joints is 6.35 mm. Figure 4.3 shows the different sections used in the lab-scale space frame and Table 4.1 gives the dimensional parameters needed to define these sections.

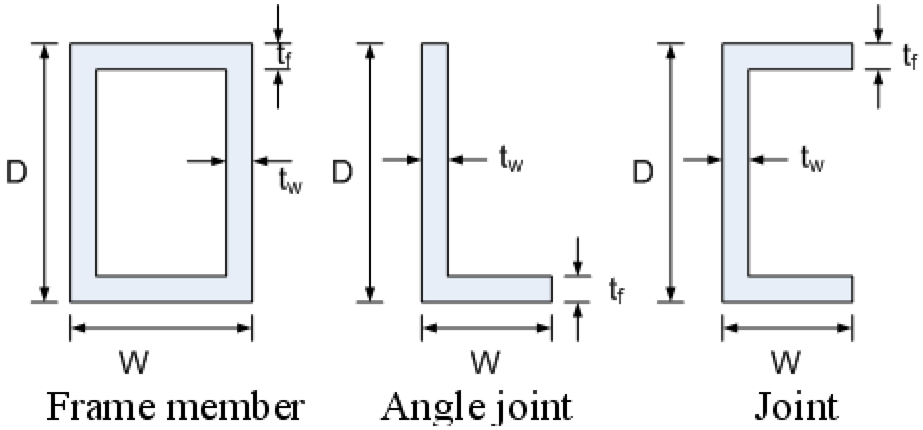

Figure 4.3: Sections comprising of the lab-scale structure

Table 4.1: Dimensional parameters of the lab-scale sections (mm)

Section Type	D	W	t_w	t_f
Frame	38.1	38.1	3.2	3.2
Joint	88.9	88.9	6.4	6.4
Angle	50.8	25.4	6.4	6.4

4.2 Material

The entire cube; frame members, square joints, and angle joints are made of Aluminum 6061 alloy. The material characteristics of this alloy are listed in Table 4.2. *MAT_PLASTIC_KINEMATIC [Appendix A] material model, present in LS-DYNA, is used to define the Aluminum 6061 alloy for computational analysis. In the material model the elastic-plastic nature of the material is defined as shown by the stress-strain in Figure 4.4. The assembled aluminum cube, including the nuts and bolts, weighed 11.4 kg and is shown in Figure 4.5.

Table 4.2: Material properties of Aluminum 6061

Property	Value
Density (kg/m^3)	2700
Modulus of Elasticity (GPa)	68.9
Poisson's Ratio	0.33
Yield Strength (MPa)	276
Tangent Modulus (MPa)	562

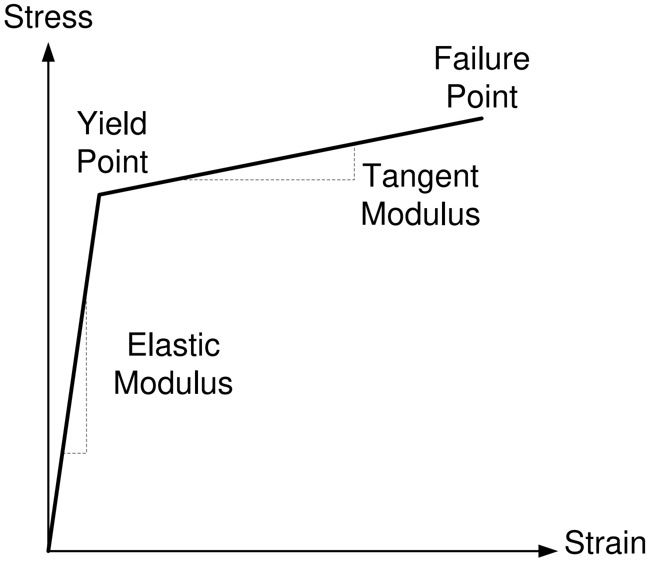

Figure 4.4: Material model for the FE analysis

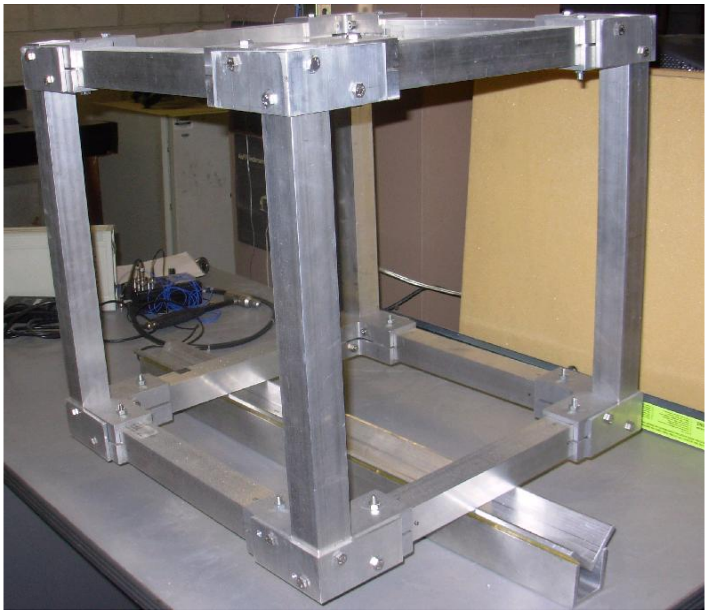

Figure 4.5: Lab-scale aluminum space frame cube

4.3 Bolt Tightening

All the bolts on the lab-scale space frame are tightened to a preload of 10.8 kN. To obtain the aforementioned preload, a torque of 12.5 N-m is applied to the bolts with the help of a torque wrench. These values were evaluated by using the standard bolt design equations shown below [59],

$$\text{Preload: } F_i = 0.9(S_p)(A_t) \tag{18}$$

$$\text{Torque: } T_i = 0.21(F_i)(d_p) \tag{19}$$

where,

S_p proof stress of the bolt material = 586 MPa

A_t tensile stress area of bolt = 2.1E-5 m^2

d_p pitch diameter of bolt treads = 5.525E-3 m

The bolts are tightened so as to reduce the noise in the output recording, and they are tightened to a standard preload to keep the experiment consistent and obtain repeatability in the result.

4.4 Joint Contact

The faces of the joint halves which meet with each other are machined off by 1.58 mm, Figure 4.6, so as to obtain a more homogenous contact between the joint and the frame members. Due to this the noise in the shock signal is removed.

Figure 4.6: Machined joint halves

4.5 Impact Experiment

Non-destructive impact testing is done on the lab-scale space frame structure to conduct shock transmission studies.

4.5.1 Experimental Equipments

4.5.1.1 Force Hammer

The impact on the cube structure is applied by PCB 086D05 [Appendix F] force hammer. It is a short-sledge impact/impulse hammer with force sensor at the tip, Figure 4.7. The salient features of the force hammer are listed in Table 4.3.

Figure 4.7:   PCB 086D05 force hammer

Table 4.3:   Characteristics of the PCB 086D05 force hammer

Sensitivity (±15%)	0.23 mV/N
Measurement range	±22000 N pk
Resonant frequency	≥ 22 kHz
Sensing element	Quartz
Hammer mass	0.32 kg
Head diameter	25 mm
Tip diameter	6.3 mm
Hammer length	227 mm

4.5.1.2 Accelerometer

A piezoelectric accelerometer is used to record shock in the form of acceleration signal, produced due to the application of the force hammer on the cube structure, at a couple of identified locations on the cube frame members. The accelerometer used is PCB 352C22 model [Appendix G], Figure 4.8. Table 4.4 lists some of the characteristics of the accelerometer.

Figure 4.8: PCB 352C22 model accelerometer

Table 4.4: Features of the PCB 352C22 accelerometer

Sensitivity (±15%)	1.0 mV/(m/s^2)
Measurement range	±4900 m/s^2 pk
Resonant frequency	≥ 50 kHz
Frequency range (±5%)	1.0 to 10,000 Hz
Sensing element	Ceramic
Sensing geometry	Shear
Size	3.6mm x 11.4mm x 6.4 mm
Weight	0.5 g
Mounting	Adhesive

4.5.1.3 SignalCalc ACE II Dynamic Signal Analyzer

Ultra-portable, SignalCalc ACE II from Data Physics features compact signal processing hardware containing 24-bit input and output channels with dedicated DSPS for each set of channels. The multiple DSP architecture allows measurements to be made at the same real-time rate regardless of the number of channels in use. This hardware is connected to the laptop by using the USB. Figure 4.9 shows the signal analyzer ACE II. Figure 4.10 shows the signal analyzer during the experimental setup. It has 4 channels for 4 inputs, a trigger and an easily configurable Tachometer [61]. This instrument is used when calibrating the force hammer or the accelerometer.

Figure 4.9: Signal analyzer

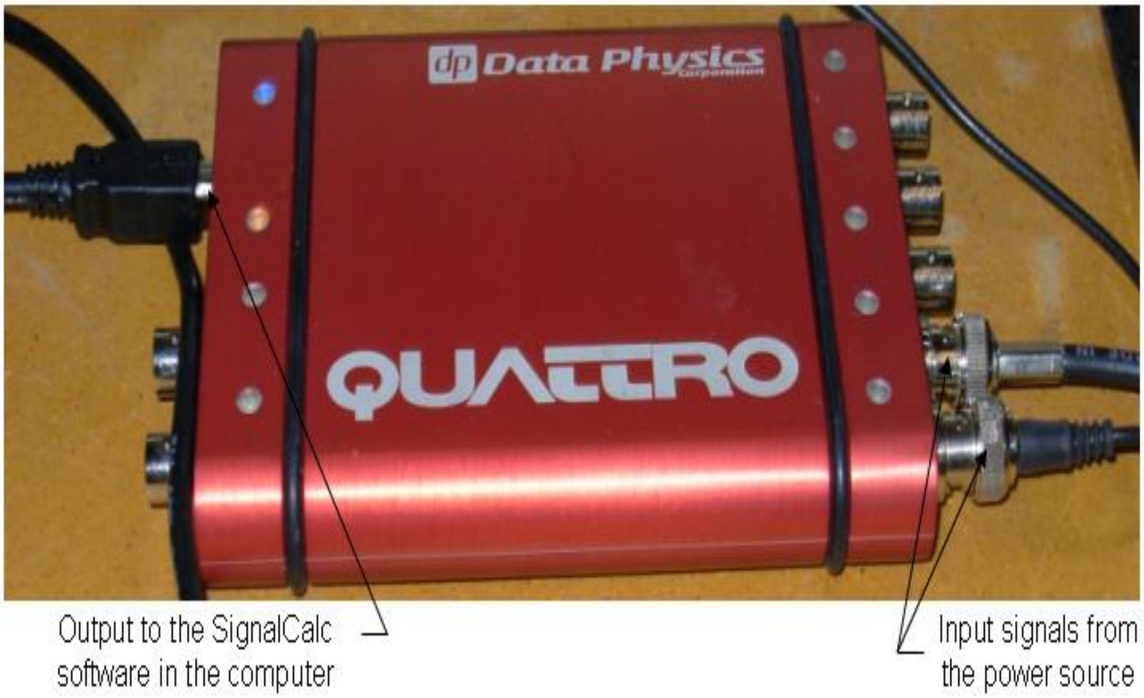

Figure 4.10: Signal analyzer during experimental setup

4.5.1.4 Signal Conditioner

A signal conditioner is a device that converts one type of electronic signal into another type of signal. Its primary use is to convert a signal that may be difficult to read by conventional instrumentation into a more easily readable format. In performing this conversion a number of functions may take place. For example, when a signal is amplified, the overall magnitude of the signal is increased. Converting a 0-10 mV signal to a 0-10 V signal is an example of amplification. The 4103C current source, Figure 4.11, power unit, manufactured from Dytran Instruments, is used as the signal conditioner, Figure 4.10. Some important specifications of the signal conditioner are listed in Table 4.5.

Figure 4.11: The 4103C current source/signal conditioner

Table 4.5: Specifications of signal conditioner [Appendix H]

Power source	9 V (two in number)
Battery life	40 hours
Size (H x W x D)	63.5 x 132.1 x 83.8 mm
Weight	0.34 kg

4.5.1.5 Calibrator

Calibrator is hand held shaker used to calibrate the accelerometers. The model number of calibrator is 394C06, Figure 4.12, and it is manufactured by PCB. Some of the specifications for the calibrator are listed in Table 4.6 [Appendix I].

Figure 4.12: PCB 394C06 Calibrator (hand held shaker)

Table 4.6: Salient features of PCB 394C06 Calibrator (hand held shaker)

Operating frequency (± 1%)	159.2 Hz
Acceleration output (± 3%)	9.81 m/s^2 rms
Maximum load	210 g
Size (diameter)	56 mm
Weight (with batteries)	900 g

4.5.1.6 Oscilloscope

The DL 750 ScopeCorder Oscilloscope is used to capture the output signals from the accelerometer and force hammer. The oscilloscope has the capability to store and display the captured output signals in voltage. The number of data points needed for each test can be adjusted by setting the sampling rate in the oscilloscope to the required value. Figure 4.13 depicts the DL 750 ScopeCorder Oscilloscope [62].

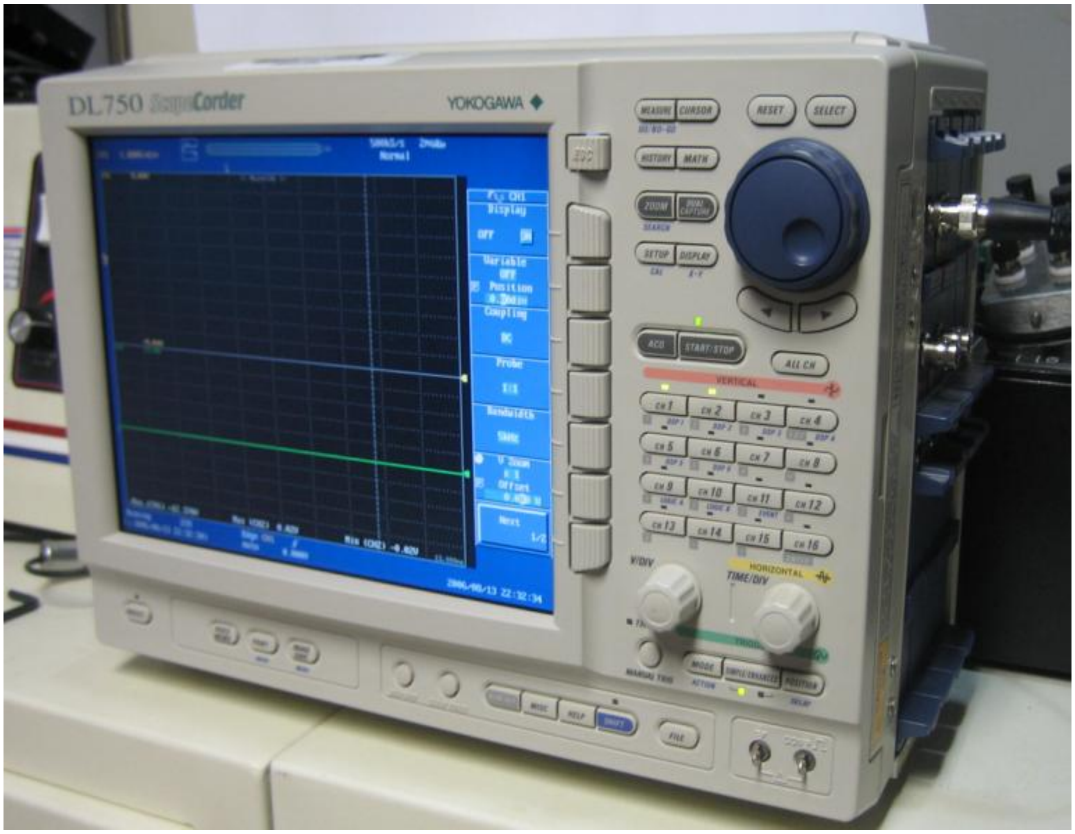

Figure 4.13: DL 750 ScopeCorder Oscilloscope

4.5.2 Experiment

During the non-destructive experiment, the lab-scale space frame is placed on an aluminum support as shown in 4.14. One of the top frame members is impacted at the mid-member location with a force hammer and the acceleration is recorded, though an accelerometer, on the opposite mid frame member location. A current source is used to supply voltage to the force hammer and the accelerometer. The output voltage obtained from the force hammer and accelerometer is converted into waveform and displayed by the oscilloscope. The sampling rate used for collecting data was 1 mega-sample/second, i.e., a data point was collected for every micro-second. Figure 4.15 depicts the flowchart of the setup for the impact testing of the cube space frame. A program, in MATLAB, was written to obtain the Fast Fourier Transform (FFT) of the outputted acceleration wave, from which the natural frequencies of the cube space frame is determined.

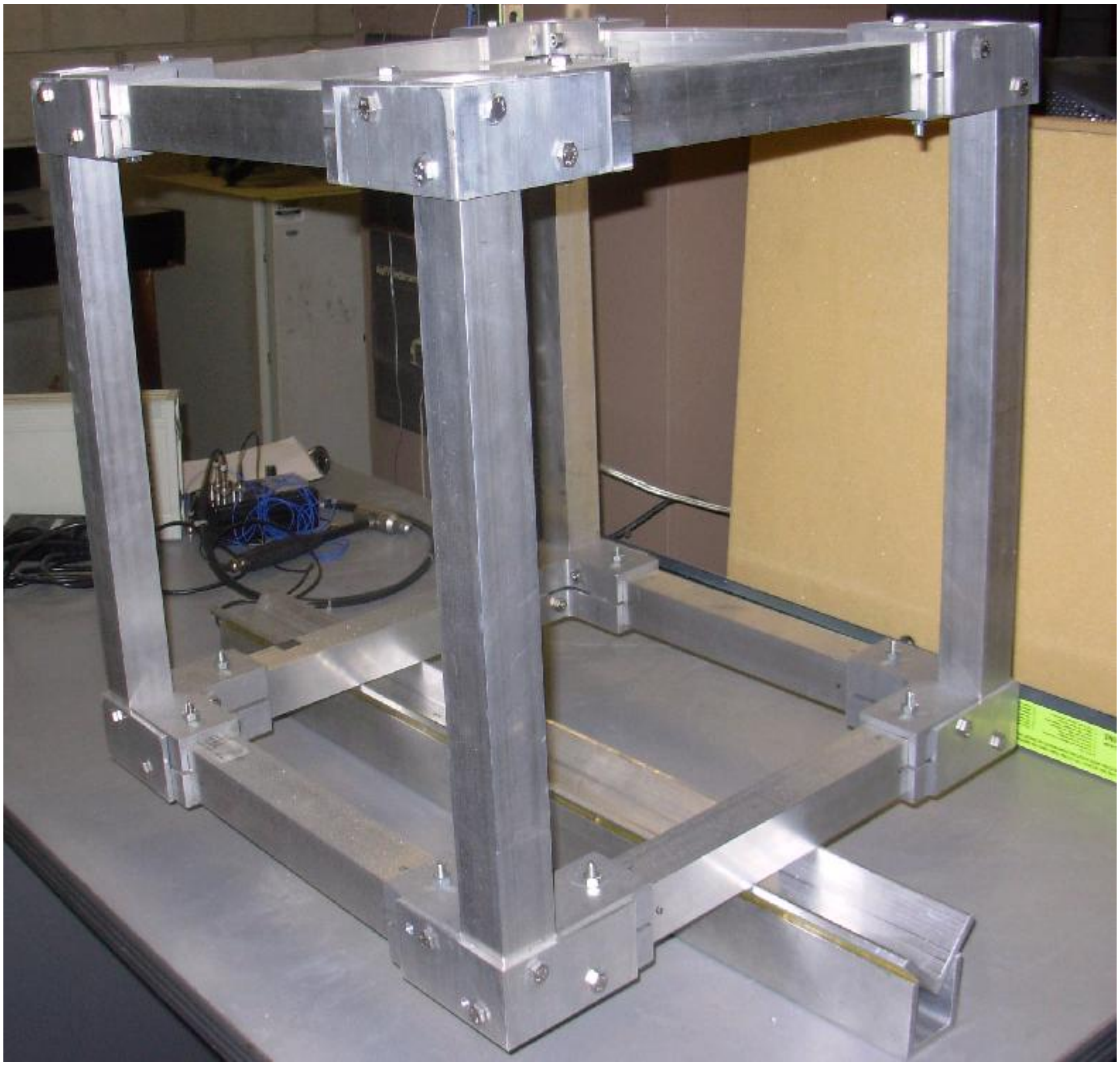

Figure 4.14: Experimental setup of the lab-scale structure

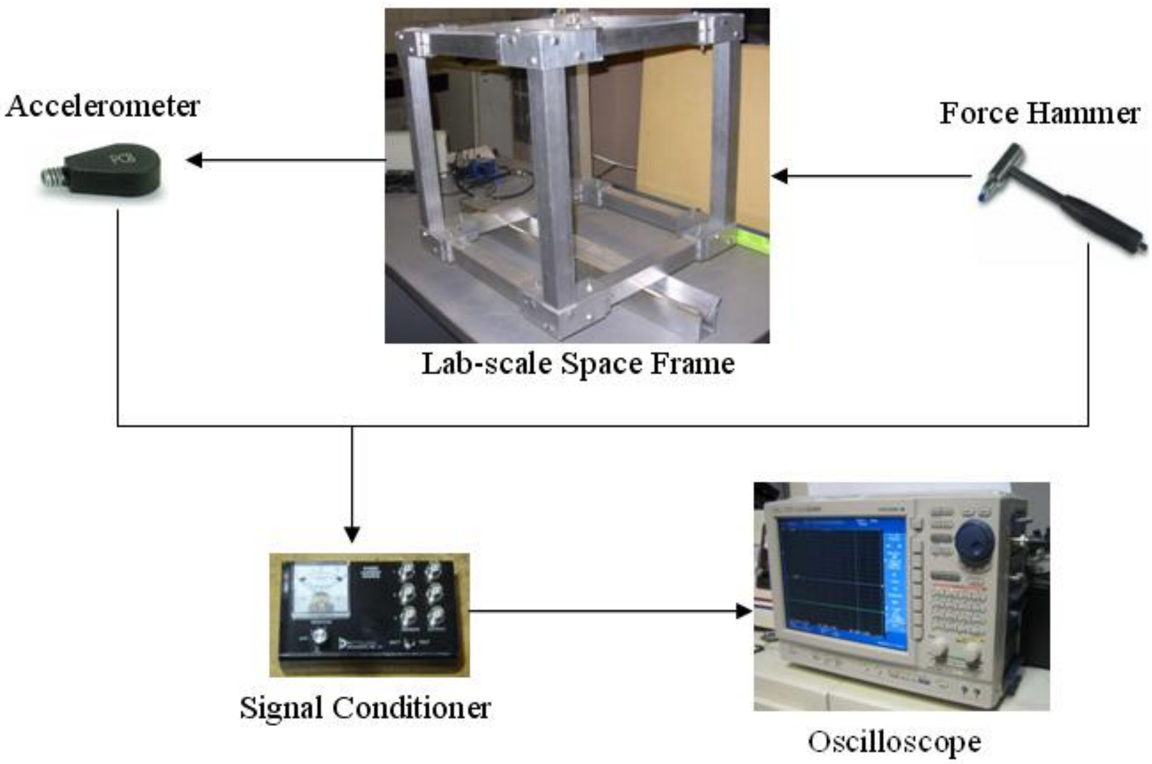

Figure 4.15: Flowchart of the impact experiment on the cube space frame

4.6 Finite Element Model

All components of the cube space frame structure are modeled using beam elements. This is done since the military vehicle space frame, from which the cube design is based on, was also modeled entirely with beam elements. Altair Hypermesh was used to create the FE model of the cube space frame, while the explicit code LS-DYNA is used to process the FE model. The same system of units and beam element type described in Chapter 2 for the military vehicle is used for the creation of cube FE model. The length of each beam element was maintained at 3.2 mm. The FE model comprises of 1,832 beam elements. Figure 4.16 shows the FE model of the cube space frame with the boundary conditions.

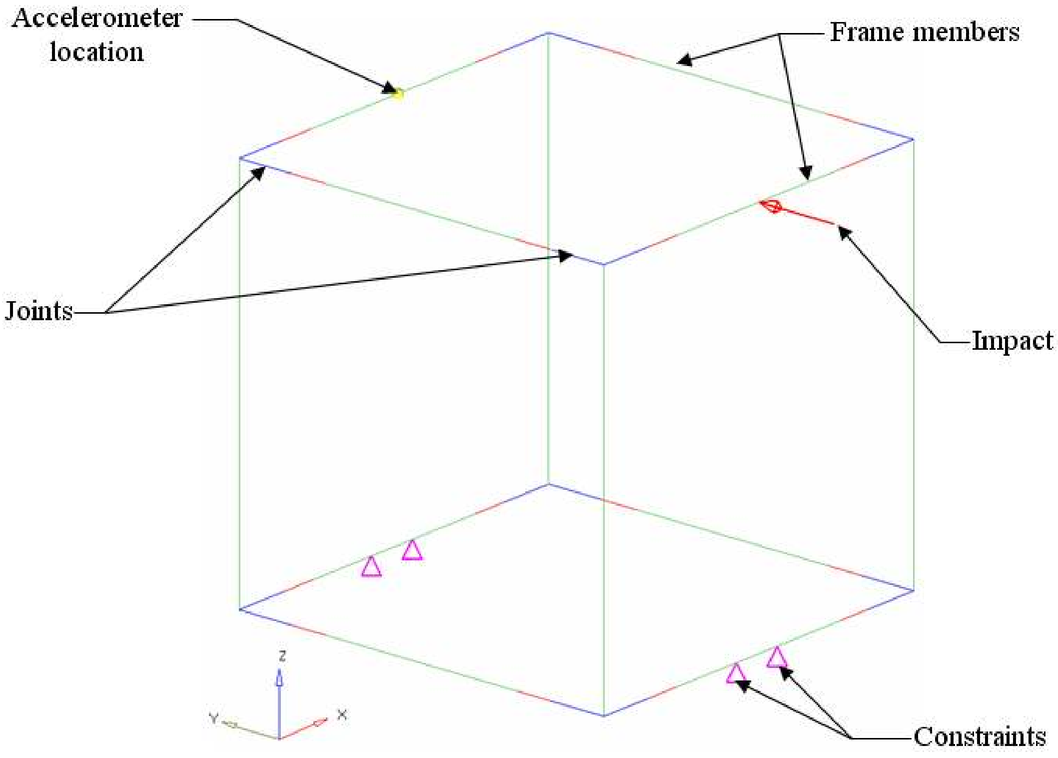

Figure 4.16: FE beam model of the lab-scale space frame

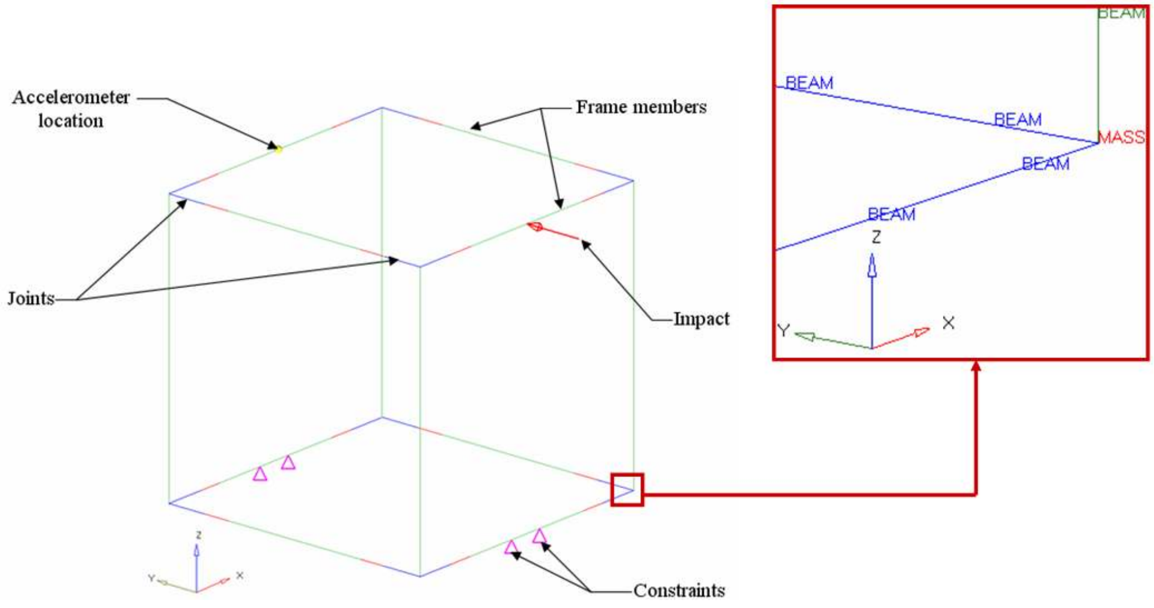

Figure 4.17: FE model depicting the mass elements at the cube corner

Elastic-plastic material model, described in section 4.2, is defined for all the structural components of the cube space frame. The common elements between the different component faces are merged to obtain contact definitions between them. Four nodes on the bottom of the cube model are constrained, as shown in Figure 4.16, to not move in the vertical direction (z-axis). The force curve obtained from the impact experiment is used to simulate the impact on the FE model and the acceleration at the accelerometer location during experiment is outputted. The bolts are not modeled in the FE model, but their mass is taken into account. This is done by adding mass elements, having the total mass of the bolts present at a joint, to each corner of the cube, Figure 4.17.

The joints in the FE model of the cube space frame structure are modeled as two parts. The first part comprises of the combined cross-section of the frame and the joint (shown in blue color in Figure 4.18). The second part consists of just the joint cross-section (shown in red color in Figure 4.18). The dynamic response of the cube space frame model was stimulated for 18 ms to keep it in tune with the experiment. The total computational time taken to run this cube FE model was 14 minutes.

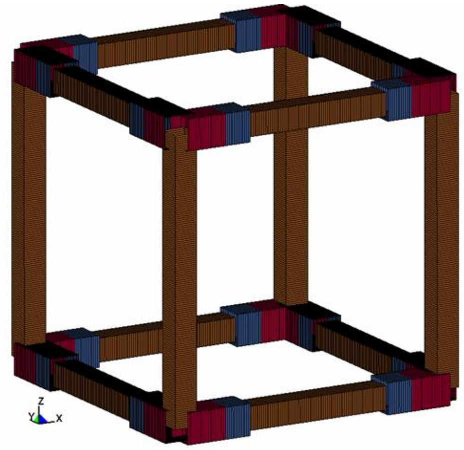

Figure 4.18: FE model of the cube space frame shown in 3D blocks

4.7 Results

The acceleration and FFT plots obtained from the impact experiment are compared with the computational results. Figure 4.19 shows the force curve obtained from the impact hammer during the experiment. The same force curve is taken for simulating the impact for the FE model.

The acceleration profiles obtained from the experiment and FE analysis of the cube space frame are filtered at 10,000 Hz. The filter type used is Butterworth with low-pass, and the frequencies above 10,000 Hz are not considered because of the limitation in accelerometer frequency range. Figure 4.20 compares the filtered acceleration signals of the experiment and the FE analysis. The predicted acceleration signal captured the first peak of the experiment, but the subsequent acceleration peaks for the FE model were smaller than the experimental ones. The frequency of the signal is good up to 8 ms, and then starts to deviate away from the experiment. After 8 ms the predicted acceleration signal gets incomparable with respect to the experimental signal which may be due to the joint effects in the cube.

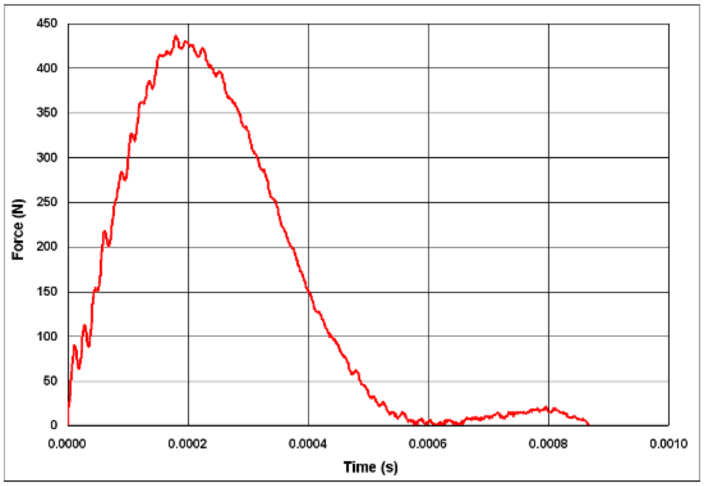

Figure 4.19: Impact force applied to the cube space frame

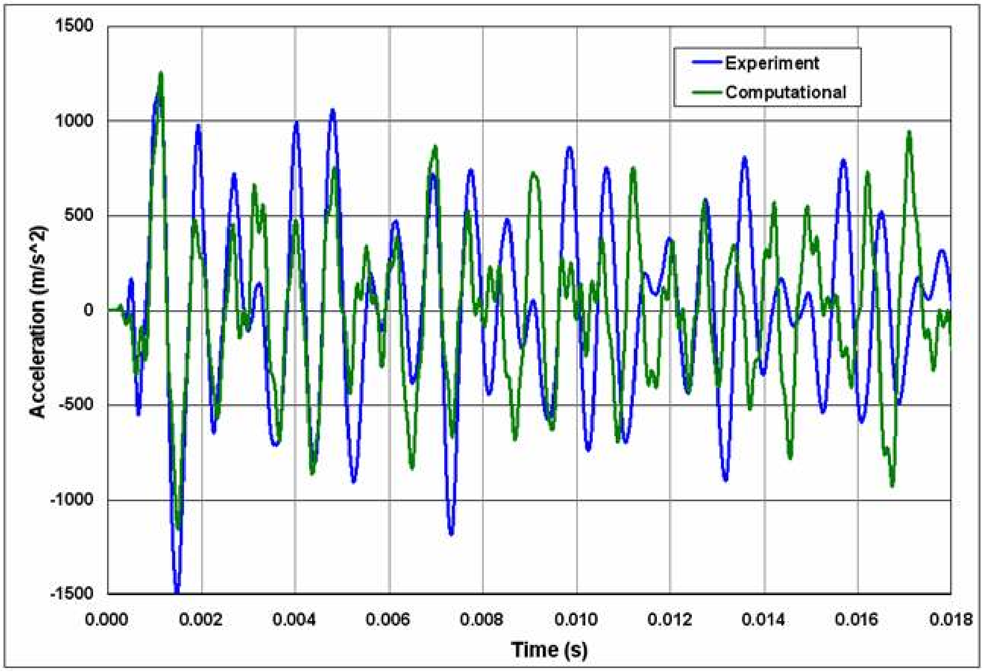

Figure 4.20: Filtered acceleration curves

FFT of both the experimental and simulated acceleration signals were computed. Figure 4.21 and Figure 4.22 show the FFT curves of the experimental and simulated acceleration signals respectively. From the FFT curves the natural frequencies of the cube space frame were determined. Since the cube space frame comprises of many components and the structure is not solid, there is more than one natural frequency. The first natural frequency from the experimental signal is 530 Hz. The simulated first natural frequency of the cube is 500 Hz, which is very close to the experimental value. The FE model of the cube predicts rest of the experimental natural frequencies, including the predominant natural frequency of 1500 Hz. There is an additional natural frequency predicted by the FE model, of 810 Hz. This may be due to the non-modeling of some structural components such as the angle joints and bolts, and also not taking into account the holes in the model. The amplitude of this additional frequency is small and hence can be ignored. Overall, for a complex structure such as the cube space frame which comprises of 48 bolts and 8 bolted joints, there is a very good match between the predicted and experimentally obtained frequency response.

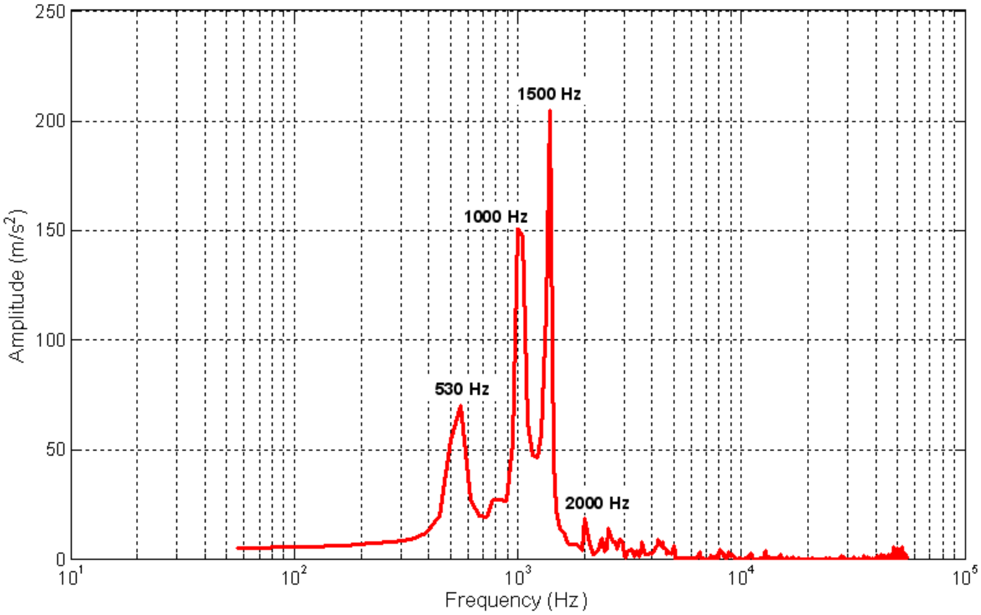

Figure 4.21: FFT of the experimental acceleration signal

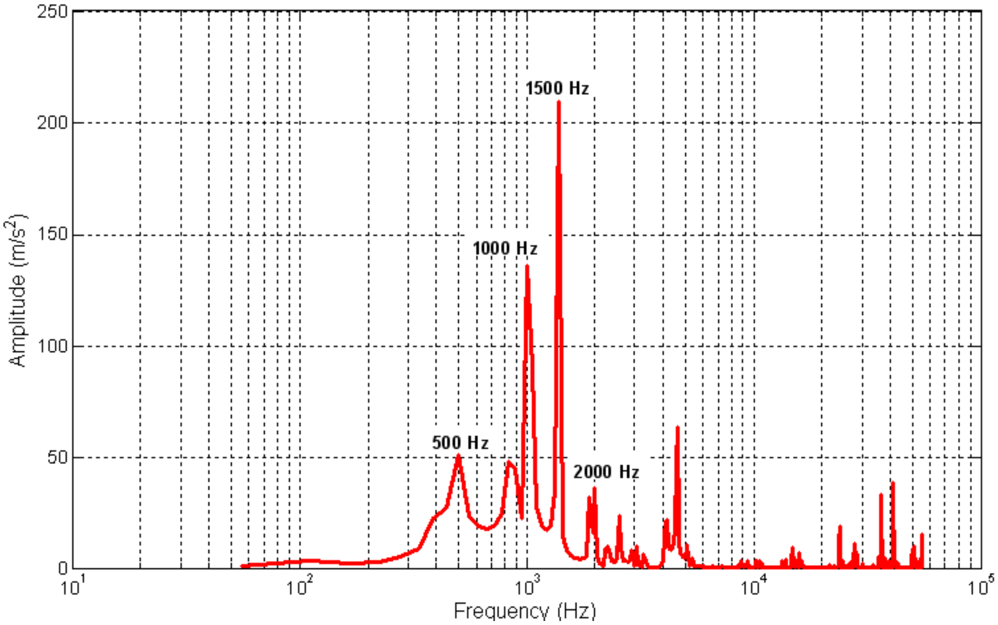

Figure 4.22: FFT of the predicted acceleration signal

4.8 Conclusions

Previous chapters looked at the computational work of the military vehicle with an internal space frame structure when subjected to a high impact hit. To check the validation of the simulated models and to conduct practical shock transmission studies a lad-scale space frame structure was derived from the military vehicle space frame. The lab-scale space frame structure was manufactured in the form of a cube. Non-destructive impact experiments were conducted on the cube shaped space frame structure, and acceleration and frequency responses were studied. A FE model of this cube space frame was created, entirely with beam elements, and the simulated results were compared to the experimental data. The initial peak of the acceleration signal was captured by the FE model, and the frequency of the predicted signal compared well with experimental signal up to 8 ms. The natural frequencies were computed by applying FFT to the acceleration signals. The FE model of the cube predicted all the experimental natural frequencies, including the predominant natural frequency. Overall, for the complex cube shaped space frame structure the simulated dynamic response was satisfactory matched with the experimental data.

CHAPTER 5

CONCLUSIONS

This chapter summarizes the work presented in this dissertation and looks at the possibility of continuity with the research. The primary objective of this dissertation was to present a methodology for the design of military vehicles with an internal space frame structures subjected to high impact or shock loadings. Based on this objective the work accomplished was threefold:

- Developed FE model of a military vehicle with an internal space frame structure.
- Parameterized this FE model, and conducted mass and shock optimization studies.
- Manufactured a lab-scale space frame structure to conduct shock transmission studies.

5.1 FE Model of the Military Vehicle

A light weight military vehicle, with an internal space frame structure, Figure 5.1, is being conceptualized by the US ARL. The research for this dissertation concentrated on the upper half of the vehicle, namely the outer armor and the internal space frame. Figure 5.2 shows a simplified model of the upper half of the vehicle. The space frame is a non-monolithic type with joints and frame members making up the entire structure. The frame members are bolted together through common components at the joints. Figure 5.3 shows a typical joint with frame members bolted to the joint branches. This arrangement allows for quick replacement of any section of the space frame that might get damaged in combat due to a projectile hit or blast impact. The entire vehicle, including the internal space frame structure with the joints, is made of Aluminum 7039 alloy heat treated to a

T64.This design of the upper half of the vehicle with the internal space frame structure was chosen as the base model for conducting the studies in this dissertation.

Figure 5.1: IS-ATD military vehicle (model supplied by US ARL)

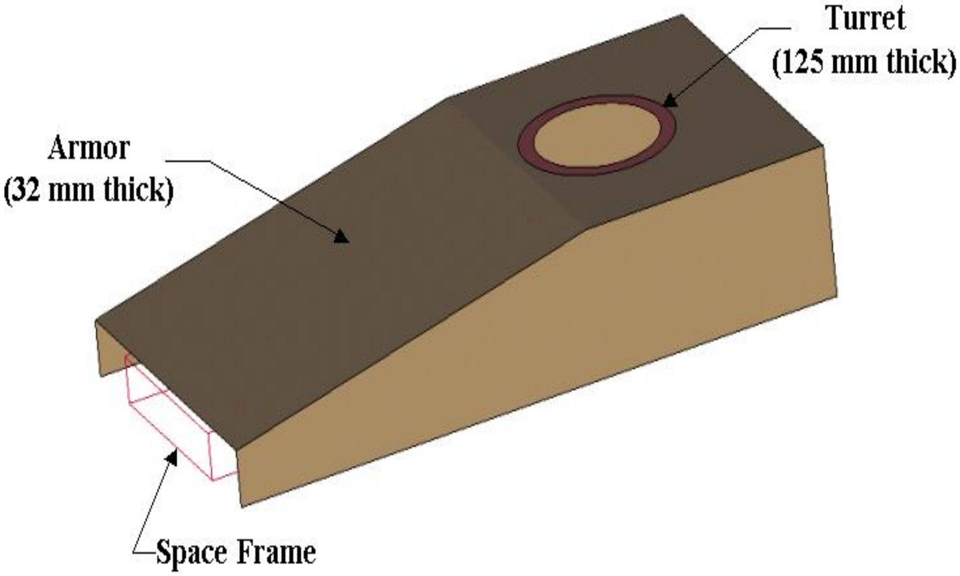

Figure 5.2: Upper half of the military vehicle with internal space frame

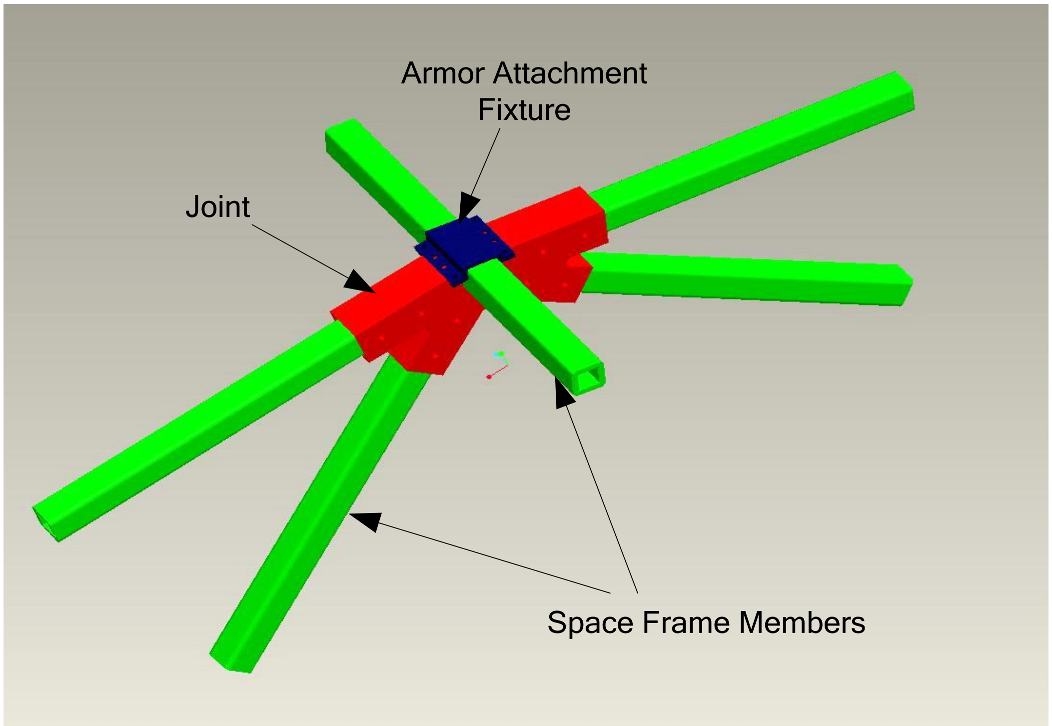

Figure 5.3: Model of a joint of the internal space frame structure

The FE model of the vehicle is as shown in Figure 5.4. The model has a total of 1192 beam elements and 8872 shell elements. The mesh of the space frame is represented in Figure 5.5. The beam elements are shown as blocks in this figure for illustration purposes only. Contact models present in the dynamic code LS-DYNA were used to define the interaction between the outer armor and inner space frame structure. It was decided to fix some locations on the vehicle to study its performance under a situation when it will absorb all of the impact energy. Four nodes on the internal space frame were selected and fixed completely. These four nodes represent the four corners at the back-end of the space frame.

Figure 5.4: FE model of the vehicle with the internal space frame structure

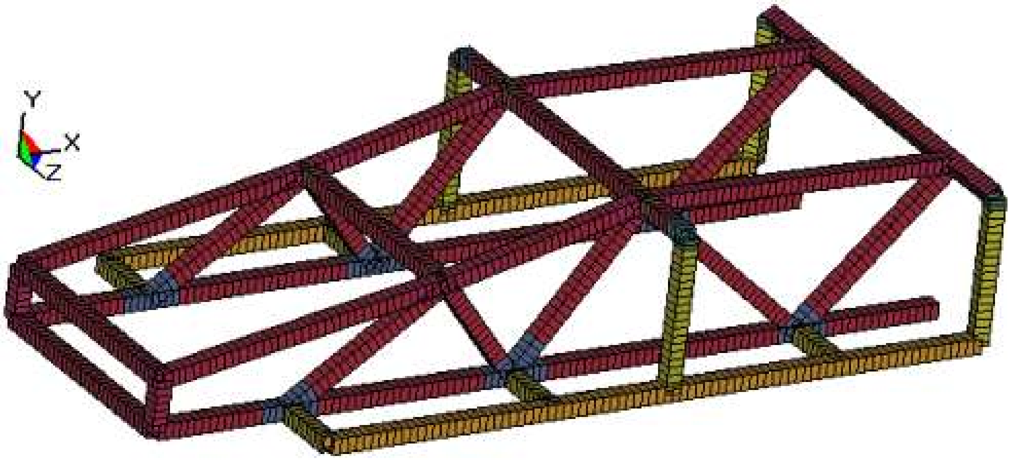

Figure 5.5: FE model of the internal space frame structure

The vehicle was subjected to projectile impact loading on the side wall, Figure 5.6. The projectile impact location was chosen to be closer to the front of the vehicle to increase the bending effect due to the fixed-displacement boundary conditions at the rear. This force impact curve was a smooth, simplified load curve approximately equivalent to force resulting from the momentum of a projectile of mass 0.8 kg hitting the side of the vehicle with an initial velocity of 938 m/s over 0.25 ms. It was assumed that the mass of the projectile was steadily disappearing through the loading phase and the force was increasing linearly. The duration of the impact load and the FE model run time was 8.4 ms. The impact impulse is shown in Figure 5.7. The total simulation run time for this FE model was approximately five minutes.

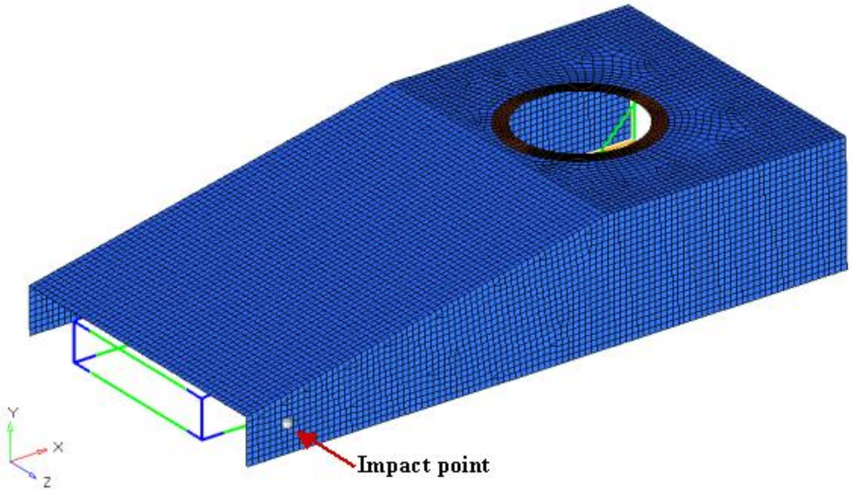

Figure 5.6: Side impact location

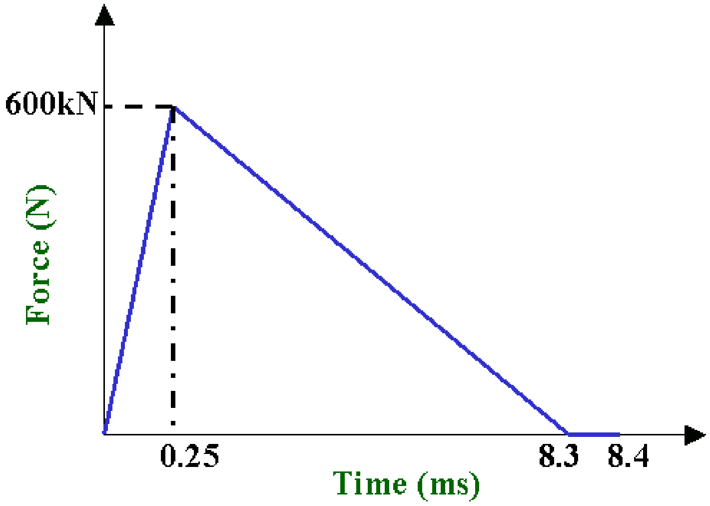

Figure 5.7: The impact impulse curve

5.2 Optimization of the FE Model

The research in the area of military vehicle space frame optimization is minimal and mostly classified. Optimization can be an important tool for the military vehicle and its internal space frame structure to minimize the overall mass, which can be an essential aspect for the mobility of the vehicle in transport and frontline. The structural integrity of the vehicle can be improved with the help of optimization technique. This can lead to mitigating shock in the vehicle due to projectile hits or explosive loads. Hence, two types of optimization studies were conducted on the FE model of the military vehicle.

The objective of the first study involved minimizing the overall mass of the military vehicle, including the internal space frame structure. The second study dealt with reducing the shock or acceleration profiles at identified critical locations on the internal space frame structure. The cross-sectional parameters of the internal space frame components, shown in Figure 5.8, and the outer armor were chosen as the design variables for the optimization process. The structural integrity of the vehicle was maintained when conducting the optimization studies. Successive Heuristic Quadratic Algorithm (SHQA) [58] was utilized to solve the optimization problem. This algorithm combines successive quadratic approximation with a controlled random search. SHQA is suitable for computationally intensive and highly non-linear problems. Figure 5.9 shows the flowchart of the optimization process.

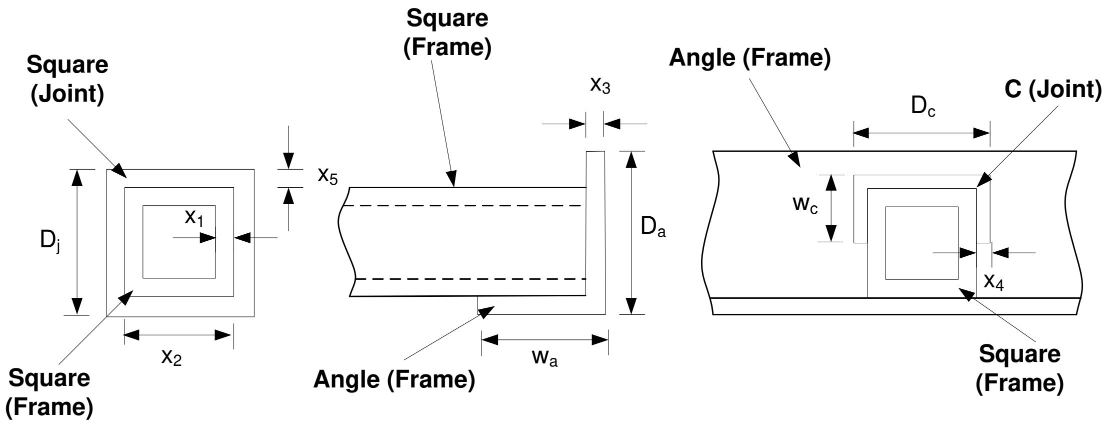

Figure 5.8: Sections of the space frame structure parameterized for optimization

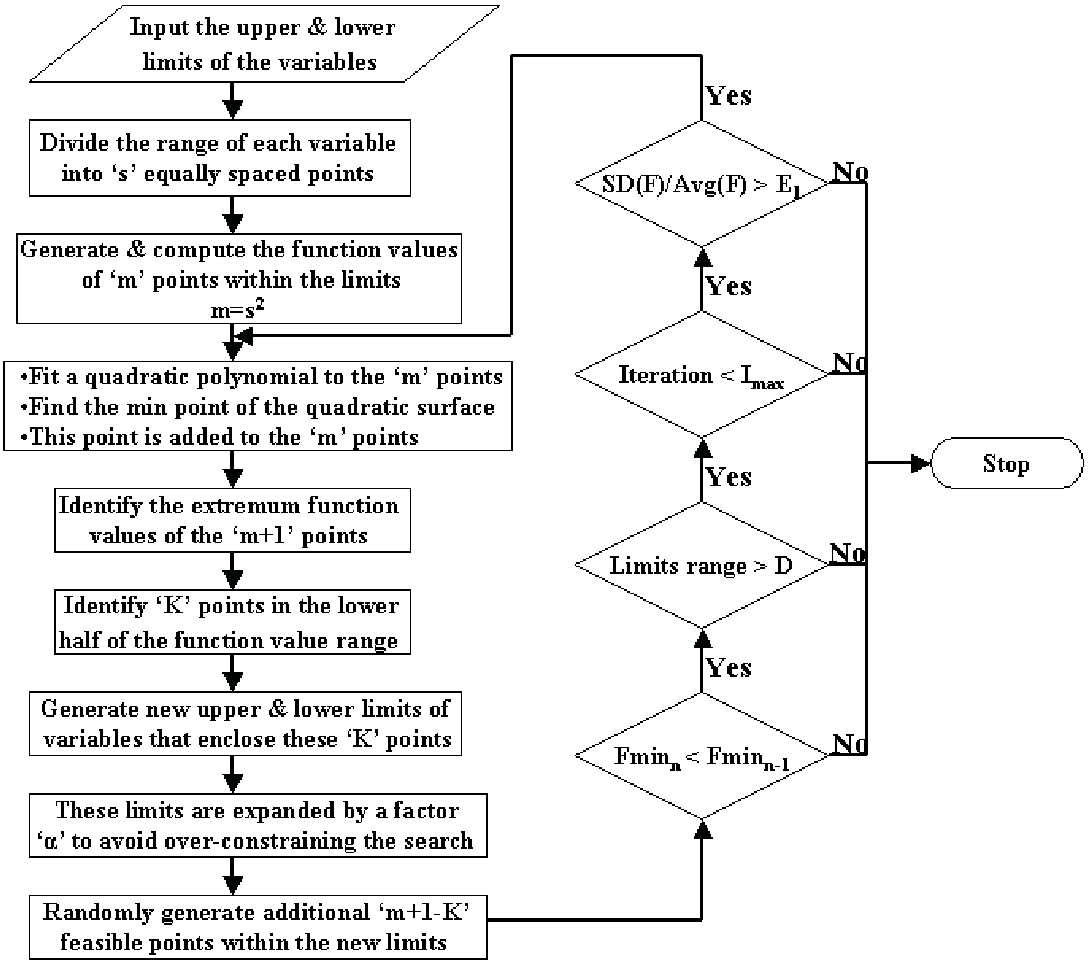

Figure 5.9: Flowchart of the optimization process using SHQA

The mass optimization results showed 25% decrease in the overall mass of the vehicle when compared to the original design. For shock optimization there was a 9% increase in the overall mass of the vehicle, while the decrease in overall shock was 95%. These significant decreases in the objective functions of the optimization processes resulted in acceptable limits of changes in the Von Mises stress, displacement and area moment of inertia for the space frame structure and armor, thus maintaining the structural integrity of the vehicle. The SHQA algorithm was found to be computationally expensive for the optimization problem presented in this paper but very productive in reaching the objective.

5.3 Lab-Scale Space Frame Structure

Currently, limited research is available in assessing the adequacy of the finite element codes in modeling shock loading across structures with joints, such as the military vehicle space frame structure. Hence, it was decided to build a lab-scale space frame structure, in the shape of a cube, comprising of joints similar in shape to the military vehicle space frame joints, Figure 5.10. The entire cube; frame members, square joints, and angle joints was made of Aluminum 6061 alloy. All the bolts on the lab-scale space frame were tightened to a preload of 10.8 kN. Non-destructive impact experiments were conducted on the cube shaped space frame structure, and acceleration and frequency responses were studied. Figure 5.11 gives a pictorial arrangement of the impact experiment. A FE model of this cube space frame was created, entirely with beam elements, Figure 5.12, and the simulated results were compared to the experimental data.

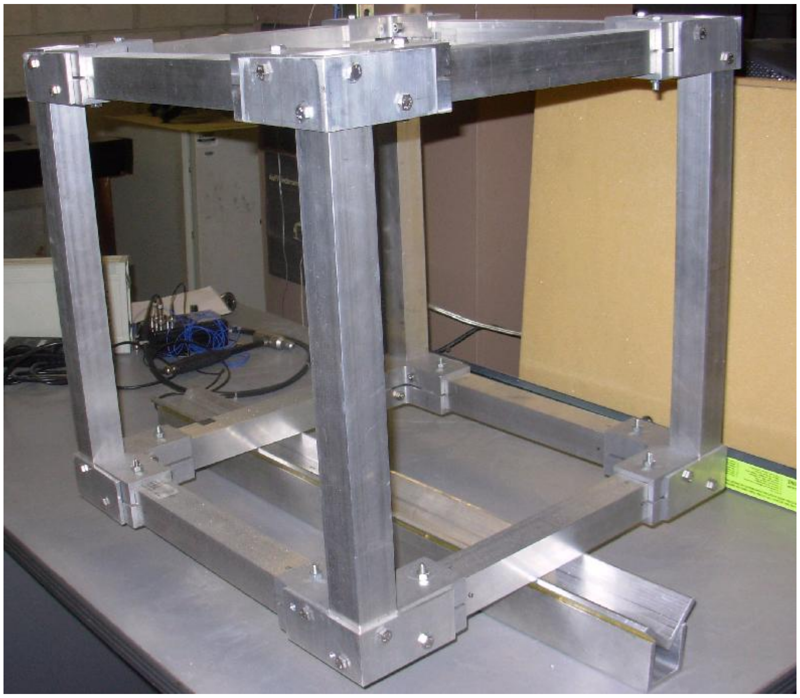

Figure 5.10: Lab-scale space frame structure in the shape of cube

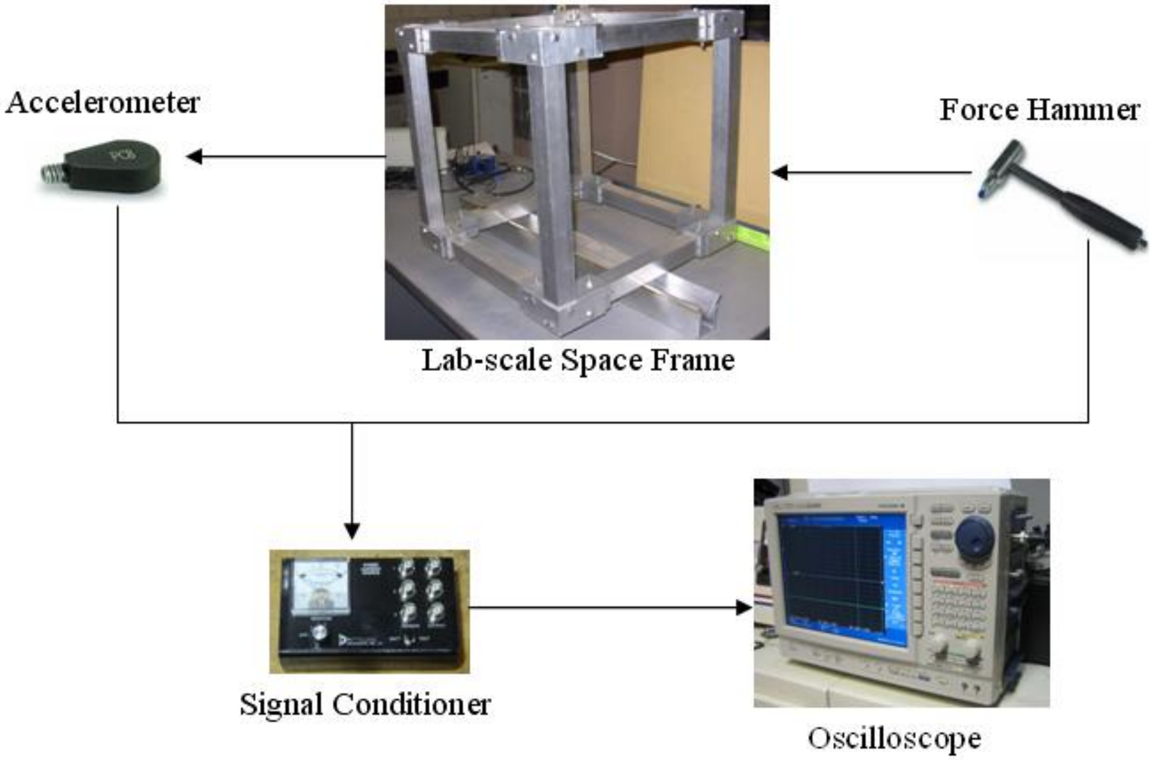

Figure 5.11: Flowchart of the impact experiment setup of the cube

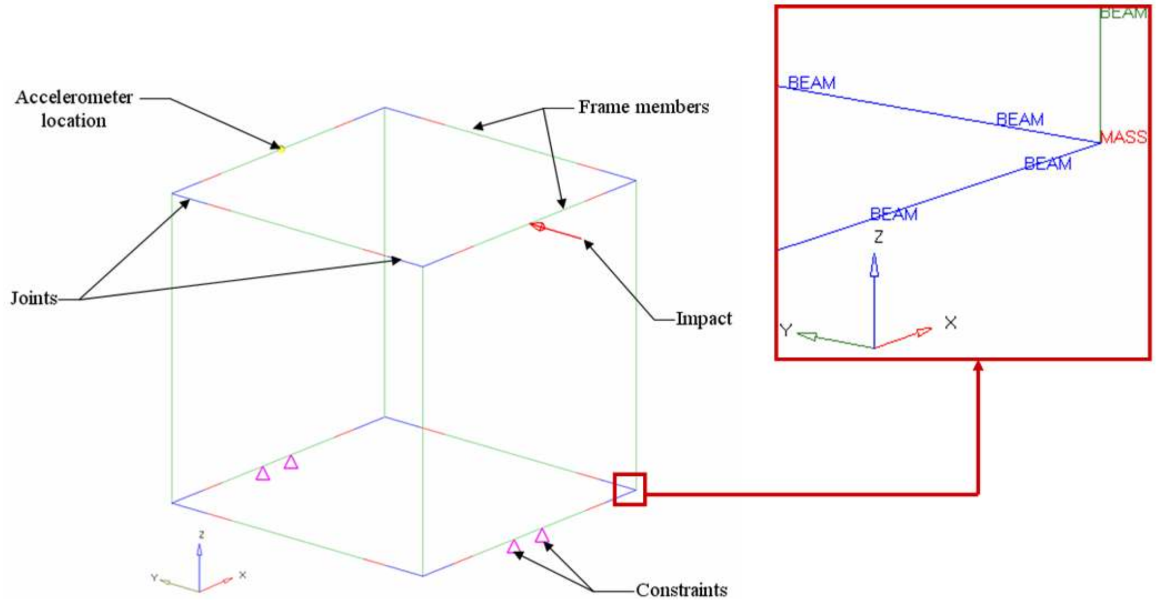

Figure 5.12: FE beam model of the cube

The initial peak of the acceleration signal matched but the simulated signal started to deteriorate after 5 ms, Figure 5.13. There was better match with the experimental and simulated natural frequencies of the cube, Figure 5.13 and Figure 5.14 respectively. The natural frequencies were computed by applying FFT to the acceleration signals. The FE model of the cube closely predicted most of the experimental natural frequencies, mainly the predominant natural frequency. Overall, for the complex cube shaped space frame structure the dynamic response was satisfactory.

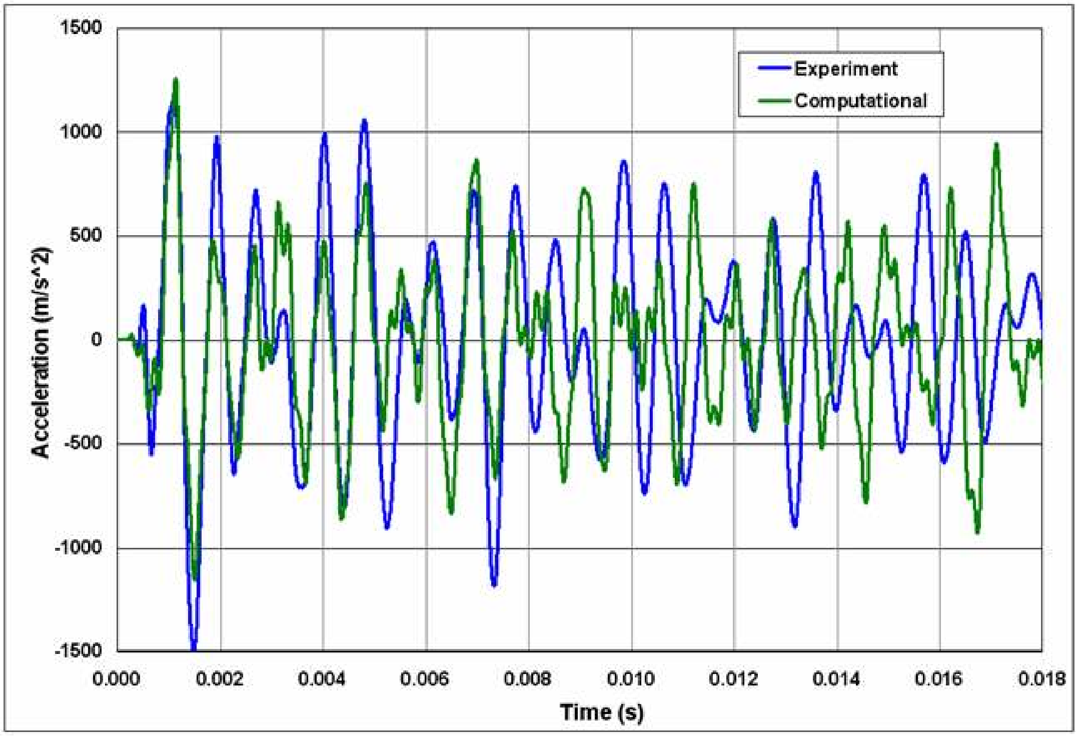

Figure 5.13: Filtered acceleration signals of the experiment and simulation

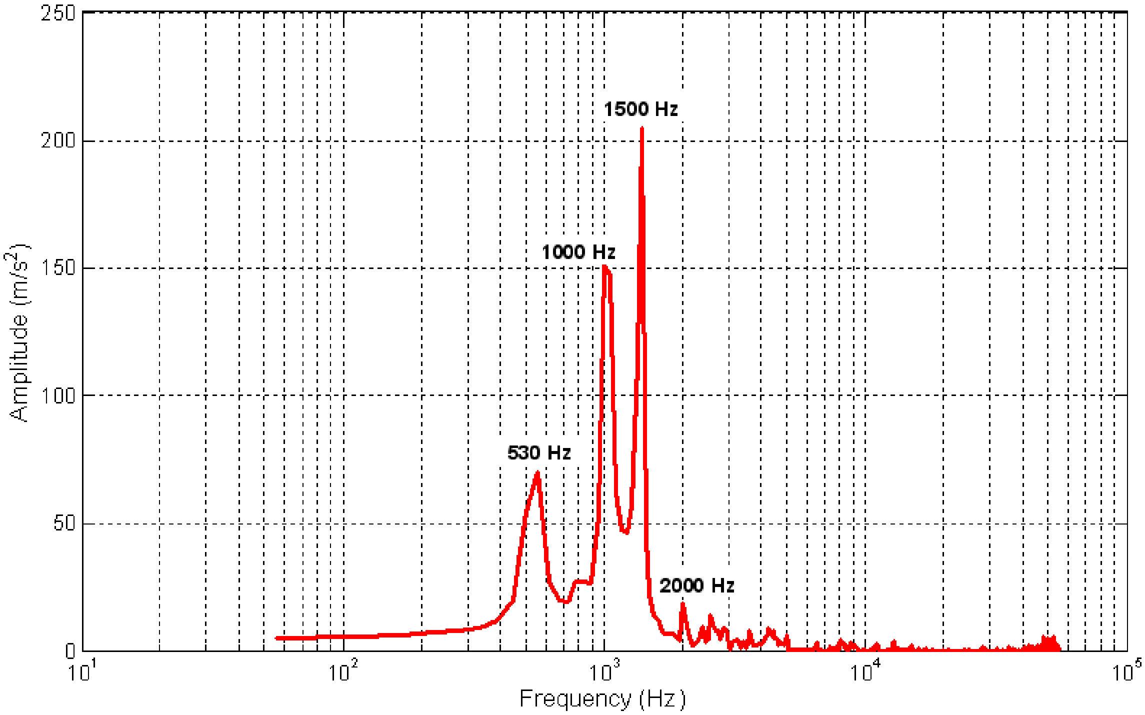

Figure 5.14: FFT of the experimental acceleration signal

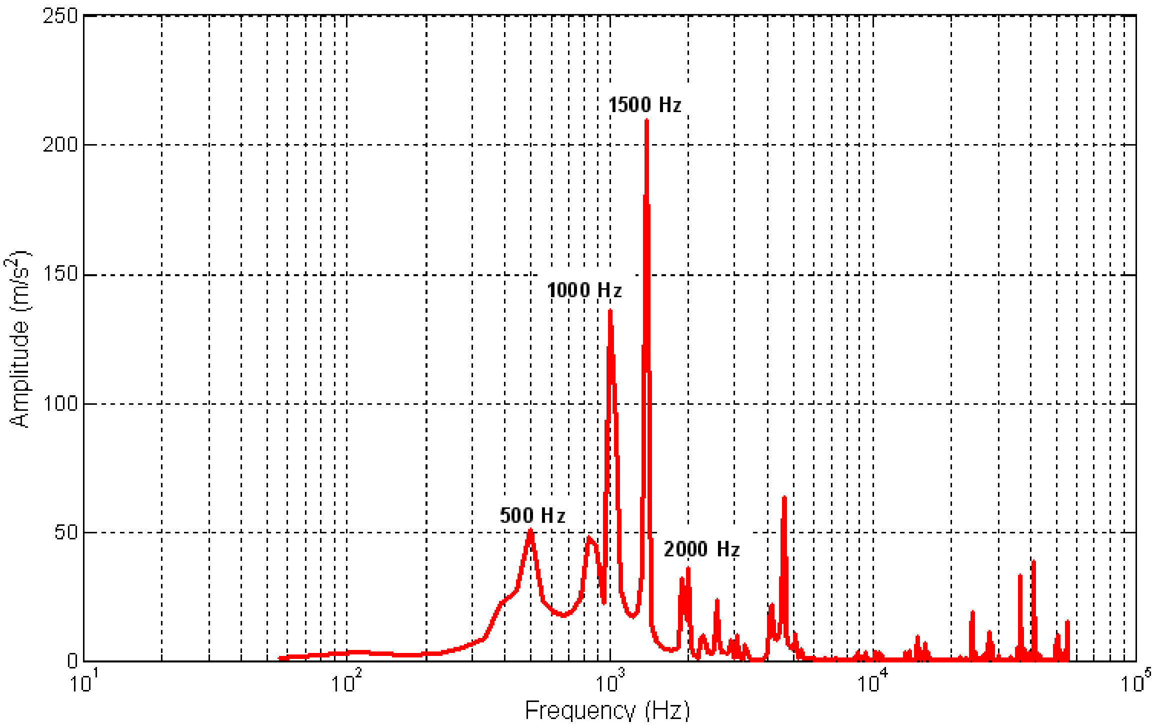

Figure 5.15: FFT of the predicted acceleration signal

5.4 Scope for Future Work

- The entire military vehicle can be considered for high impact and optimization studies.
- The use of other global optimization methods can be pursued and compared with SHQA.
- Redesigning of the vehicle for the case of mine blast loading.
- More generalization of the design process can be achieved by including additional dimensional parameters of the vehicle space frame, such as the length of the frame members and joints.
- Consider modeling the bolts on the FE model of the cube space frame structure to get a better understanding of their effect.

APPENDIX A

LS-DYNA INPUT CARDS

The dynamic software LS-DYNA is used to process the FE models listed in this dissertation. The input file for LS-DYNA is in the form of a text file. This text file comprises of sections defining each unique aspect of the FE model. These sections are known as cards. The LS-DYNA cards used to create the FE models in this dissertation are explained in this Appendix.

A.1 Material Model

The type and properties of the component materials can be defined in the MAT cards available in LS-DYNA. Material type MAT3 is used to define the isotropic properties of the vehicle and cube FE models.

A.1.1 MAT3

MAT3 card is named as *MAT_PLASTIC_KINEMATIC in the LS-DYNA input file. This material model essentially behaves like a bilinear elastic-plastic material and is used to model isotropic and kinematic hardening plasticity materials. This material model covers for the stress strain curve in the elastic region (until yield stress) and also in the plastic region (beyond yield stress). The stress-strain curve is assumed to be linear within each of these regions and hence comprises of two straight lines. Such a simplified stress strain curve is shown in Figure A.1. The slope of the stress-strain curve (from origin to the yield point) is defined as the Elastic Modulus of the material. While the slope of the stress-strain curve (beyond yield point) is defined as the Tangent Modulus for this material model. To determine the linear portion of the curve in the plastic region, a point that lies intermediate to the points corresponding to the ultimate stress and failure stress values on the stress-strain curve is selected so as to achieve a reasonable value for the Tangent Modulus.

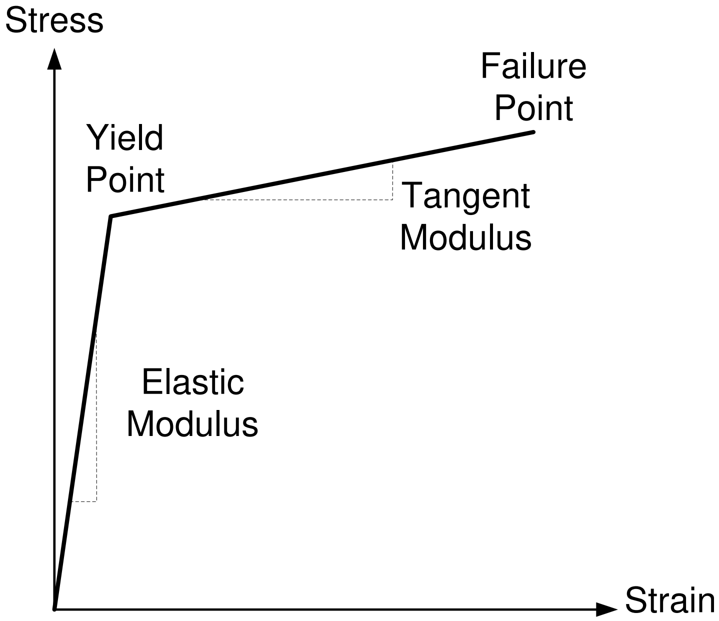

Figure A.1: Stress-strain curve for MAT3 material model in LS-DYNA

This material model can be used for beam, shell and solid elements, and is cost effective. MAT3 card is defined in the LS-DYNA input file as shown below,

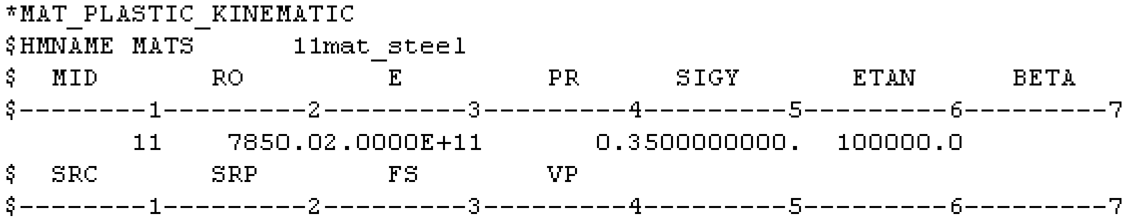

```
*MAT_PLASTIC_KINEMATIC
$HMNAME MATS      11mat_steel
$  MID       RO         E         PR      SIGY       ETAN      BETA
$--------1---------2---------3---------4---------5---------6---------7
        11    7850.02.0000E+11       0.3500000000.  100000.0
$  SRC       SRP        FS        VP
$--------1---------2---------3---------4---------5---------6---------7
```

where,

MID	Material identification number
RO	Density (kg/m^3)
E	Modulus of Elasticity (N/m^2)
PR	Poisson's Ratio
SIGY	Yield Strength (N/m^2)
ETAN	Tangent Modulus (N/m^2)

A.2 Boundary Conditions

Two sets of boundary conditions are defined for all the FE models. First set comprises of the constraints applied to the nodes to define the translational and rotational degrees of freedom. The second set of boundary conditions is the load definitions.

A.2.1 Constraints

For the vehicle the four back end nodes of the space frame are rigidly constrained, while for the cube two rows of nodes on the bottom frame members are constrained to move in the downward direction. The LS-DYNA card used to define constraints is *BOUNDARY_SPC_NODE. This card has the option of constraining a specified node or a set of nodes along the six degrees of freedom (three translational along the three coordinate axes x, y and z, and three rotational about these axes). Below is a sample of this card defined in the LS-DYNA input file,

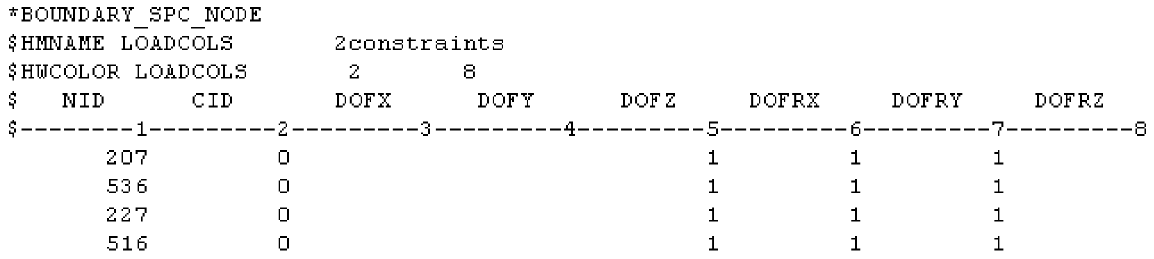

```
*BOUNDARY_SPC_NODE
$HMNAME LOADCOLS       2constraints
$HWCOLOR LOADCOLS       2       8
$   NID      CID       DOFX      DOFY      DOFZ     DOFRX     DOFRY     DOFRZ
$--------1---------2---------3---------4---------5---------6---------7---------8
       207         0                             1         1         1
       536         0                             1         1         1
       227         0                             1         1         1
       516         0                             1         1         1
```

where,

NID	Node identification number
CID	Coordinate system id
DOFX, DOFY, DOFZ	Translational constraint along the x, y and z axes
DOFRX, DOFRY, DOFRZ	Rotational constraint about the x, y and z axes

A.2.2 Load

For the vehicle the impact impulse of the side of the vehicle is applied in the form of a point load. The LS-DYNA card used is *LOAD_NODE_POINT shown below. The node on which the impact load is applied is defined in this card. The impact impulse curve is defined by using the *DEFINE_CURVE card present in LS-DYNA. This impulse curve is called in the *LOAD_NODE_POINT card.

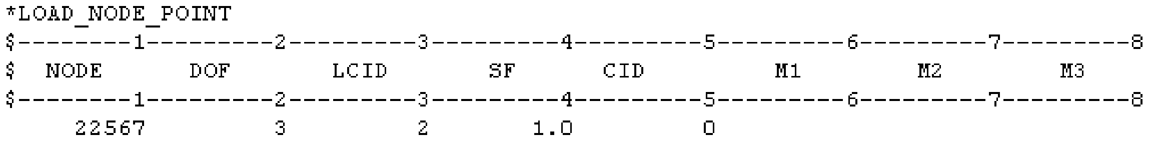

```
*LOAD_NODE_POINT
$--------1---------2---------3---------4---------5---------6---------7---------8
$  NODE      DOF       LCID       SF      CID         M1        M2        M3
$--------1---------2---------3---------4---------5---------6---------7---------8
     22567         3         2       1.0         0
```

where,

NODE	Node identification number
DOF	Applicable degrees of freedom
LCID	Load curve ID (*DEFINE_CURVE)
SF	Load curve scale factor
CID	Coordinate system ID

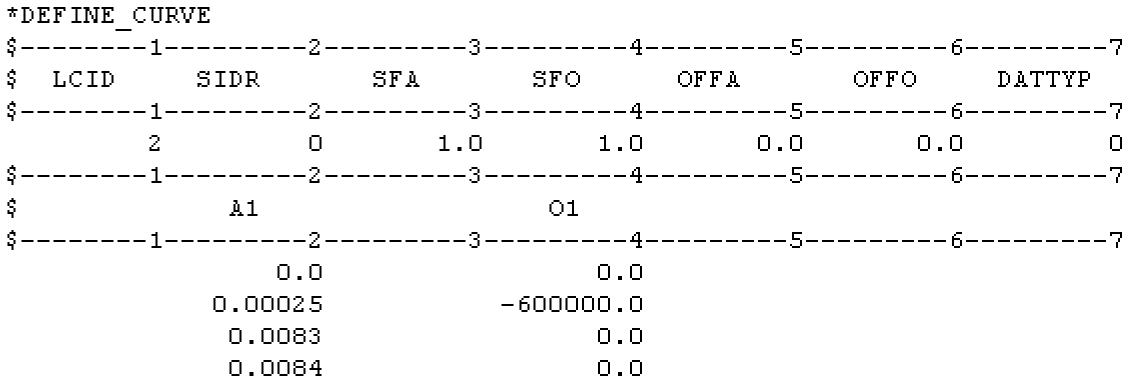

```
*DEFINE_CURVE
$--------1---------2---------3---------4---------5---------6---------7
$  LCID     SIDR       SFA       SFO      OFFA       OFFO     DATTYP
$--------1---------2---------3---------4---------5---------6---------7
         2         0       1.0       1.0       0.0       0.0         0
$--------1---------2---------3---------4---------5---------6---------7
$             A1                  O1
$--------1---------2---------3---------4---------5---------6---------7
                 0.0                 0.0
             0.00025           -600000.0
              0.0083                 0.0
              0.0084                 0.0
```

where,

LCID	Load curve id
SIDR	Stress initialization by dynamic relaxation
SFA, SFO	Scale factor for abscissa & ordinate values of the curve
OFFA, OFFO	Offset for abscissa & ordinate values of the curve
A1	Abscissa (x) values of the curve
O1	Ordinate (y) values of the curve

When the scale factors (SFA & SFO) and offset values (OFFA & OFFO) are defined in the *DEFINE_CURVE card, then the new abscissa and ordinate values are given as,

$$\text{Abscissa value} = \text{SFA}*(\text{Defined value} + \text{OFFA}) \qquad (A.1)$$

$$\text{Ordinate value} = \text{SFO} * (\text{Defined value} + \text{OFFO}) \qquad (A.2)$$

A.3 Contact Algorithms

To define interaction between the armor and the space frame componenets in the military vehicle the *CONTACT_TIED_NODES_TO_SURFACE card is used. This card ties the nodes of one component to the surface of another component. Hence, the contact obtained from this card behaves similar to a welded or bolted connection, assuming no failure in the connection.

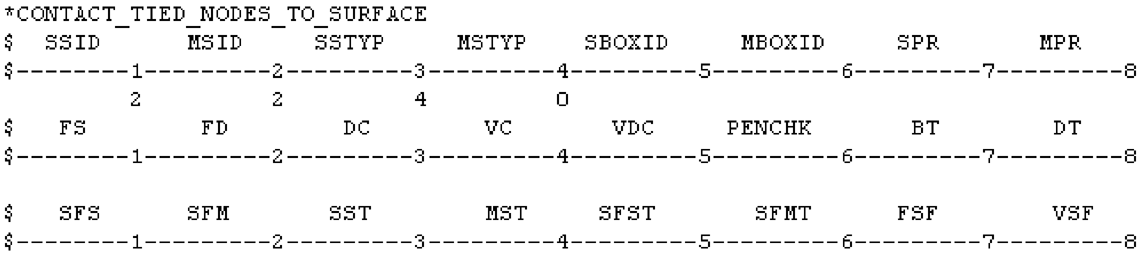

```
*CONTACT_TIED_NODES_TO_SURFACE
$  SSID      MSID     SSTYP     MSTYP    SBOXID     MBOXID      SPR       MPR
$--------1---------2---------3---------4---------5---------6---------7---------8
         2         2         4         0
$   FS        FD        DC        VC       VDC     PENCHK       BT        DT
$--------1---------2---------3---------4---------5---------6---------7---------8

$   SFS      SFM       SST        MST     SFST       SFMT      FSF        VSF
$--------1---------2---------3---------4---------5---------6---------7---------8
```

where,

SSID	Slave segment id
MSID	Master segment id
SSTYP	Slave segment type
MSTYP	Master segment type

The *CONTACT_TIED_NODES_TO_SURFACE card comprises of three mandatory rows. The first row is used to define the slave and master segments of the contact. The second row is used if there is a need to define the coefficient of friction values between the interfaces. If any scale factors are to be utilized then the third row of the card is applied.

A.4 Property Definitions

These cards give the overall property of the component, such as if the component comprises off shell elements or beam elements, the material type, nodes forming the element, etc. The *NODE card is used to define the x, y and z coordinates of the nodes present in the FE model. The format of this card is as shown below

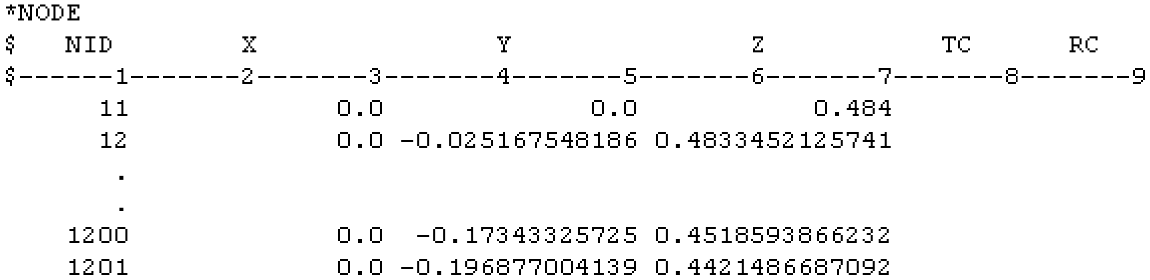

```
*NODE
$   NID        X               Y               Z           TC      RC
$------1-------2-------3-------4-------5-------6-------7-------8-------9
      11             0.0             0.0           0.484
      12             0.0 -0.025167548186 0.4833452125741
       .
       .
    1200             0.0  -0.17343325725 0.4518593866232
    1201             0.0 -0.196877004139 0.4421486687092
```

where,

NID	Node id
X, Y, Z	The global coordinates of the specified node

For LS-DYNA to know if the specified element is shell or beam, there is a need to define the *ELEMENT_SHELL or *ELEMENT_BEAM card. The former card is used if the element type is shell and the later for beam elements. The nodes associated with each element are defined in these cards. The formats of these cards are as shown below,

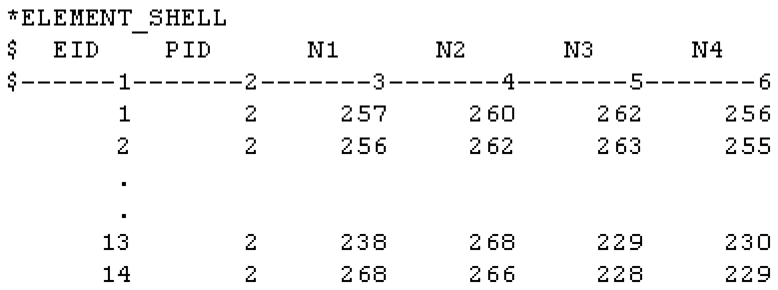

```
*ELEMENT_SHELL
$  EID    PID      N1      N2      N3      N4
$------1-------2-------3-------4-------5-------6
       1       2     257     260     262     256
       2       2     256     262     263     255
       .
       .
      13       2     238     268     229     230
      14       2     268     266     228     229
```

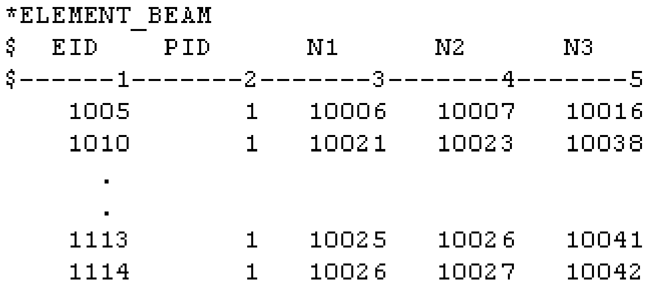

```
*ELEMENT_BEAM
$  EID    PID      N1      N2      N3
$------1-------2-------3-------4-------5
    1005       1   10006   10007   10016
    1010       1   10021   10023   10038
       .
       .
    1113       1   10025   10026   10041
    1114       1   10026   10027   10042
```

where,

EID	Element id
PID	Part id
N1, …., N8	Node id’s comprising of an element

To define the sectional properties of the shell and beam elements, *SECTION_SHELL and *SECTION_BEAM cards are respectively used. The general *SECTION_SHELL card is as shown below,

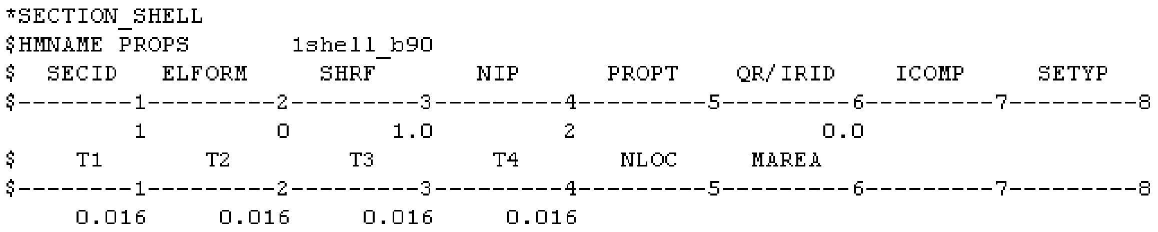

```
*SECTION_SHELL
$HMNAME PROPS       1shell_b90
$  SECID   ELFORM     SHRF       NIP      PROPT    QR/IRID    ICOMP     SETYP
$--------1---------2---------3---------4---------5---------6---------7---------8
         1         0       1.0         2                 0.0
$    T1       T2        T3        T4       NLOC     MAREA
$--------1---------2---------3---------4---------5---------6---------7---------8
     0.016     0.016     0.016     0.016
```

where,

SECID	Section id
ELFORM	Element formulation options
SHRF	Shear correction factor
NIP	Number of through thickness integration points
T1, T2, T3, T4	Shell thickness at nodes N1, N2, N3 and N4

For all the *SECTION_SHELL cards the default Belytschko-Lin-Tsay shell element formulation present in LS-DYNA is utilized. The number of integration points in the thickness direction of any shell layer is taken as two. For the *SECTION_BEAM card the Hughes-Liu with cross section integration element formulation is used. In order to define the integration rule of the beam elements the *INTEGRATION_BEAM card is used. This card has the flexibility to use user defined through the thickness integration rules for the beam element. Predetermined cross section shapes are available in this card,

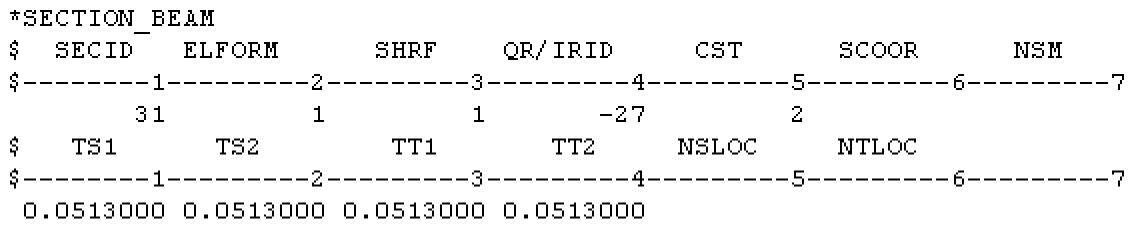

```
*SECTION_BEAM
$  SECID   ELFORM      SHRF    QR/IRID     CST      SCOOR      NSM
$--------1---------2---------3---------4---------5---------6---------7
        31         1         1       -27         2
$   TS1      TS2        TT1       TT2     NSLOC     NTLOC
$--------1---------2---------3---------4---------5---------6---------7
 0.0513000 0.0513000 0.0513000 0.0513000
```

where,

SECID	Section id
ELFORM	Element formulation options
SHRF	Shear correction factor
QR/IRID	Rule number for user defined integrated beams
CST	Cross section type

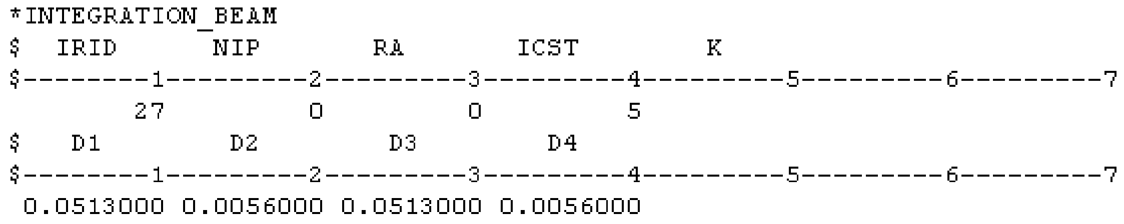

```
*INTEGRATION_BEAM
$  IRID      NIP       RA       ICST        K
$--------1---------2---------3---------4---------5---------6---------7
        27         0         0         5
$   D1        D2        D3        D4
$--------1---------2---------3---------4---------5---------6---------7
 0.0513000 0.0056000 0.0513000 0.0056000
```

where,

IRID	Integration rule ID (from *SECTION_BEAM card)
NIP	Number of integration points
RA	Relative area of cross section
ICST	Standard cross section type
D1, D2, D3, D4	Cross section dimensions

APPENDIX B

OFF-THE-SHELF PROGRAM FOR MASS OPTIMIZATION

The optimization problem presented in this dissertation was also solved using an off-the-shelf optimization program from Matlab Optimization Toolbox. The optimization program used from the toolbox is called *fmincon*. This algorithm is useful in finding the minimum of a constrained nonlinear multivariable function. The *fmincon* is a medium scale optimization algorithm and uses a sequential quadratic programming method. This algorithm computes the Lagrange multipliers of the Kuhn-Tucker (KT) equations [60] directly. A constrained Quasi-Newton line search method is used for convergence by accumulating second order information of the KT equations. The algorithm solves a quadratic program sub-problem at each iteration. When the optimization problem becomes infeasible, *fmincon* algorithm attempts to minimize the maximum constraint value. The default termination tolerances for *fmincon* algorithm are 1e-6. This is less than or equal to the SHQA termination tolerances. Hence, during the *fmincon* optimization process the default termination tolerances are maintained.

The same upper and lower bounds that were used for SHQA are used for *fmincon* algorithm, Table B.1. The *fmincon* optimization algorithm underwent 606 function evaluations and 24 iterations to reach the minimum. The optimization process took 45 hours of computational time. Table B.2 compares the results before and after optimization using the *fmincon* algorithm. While the computational time of *fmincon* is less than that of SHQA, it resulted in greater minimum than SHQA. There is a 16% decrease in the vehicle mass with the *fmincon* algorithm whereas SHQA resulted in 25%

decrease. This shows that the off-the-shelf optimization program is inadequate to solve an optimization problem like the one detailed in this dissertation.

Table B.1: Comparison of variables before and after optimization using the *fmincon* algorithm

Parameters	Original design	Final design	Lower limit	Upper limit
x_1	6.4	5.2	3	7
x_2	57.2	51.4	40	110
x_3	15.9	11.6	3	35
x_4	12.7	9.5	3	14
x_5	12.7	9.5	3	14
x_6	32.0	28.0	20	40

Table B.2: Optimization results using the *fmincon* algorithm

Parameters		Original design	Final design	% change
Mass (kg)	Armor	1119.50	979.6	-12.5
	Space frame	263.46	180.6	-31.5
Total mass (kg)		1382.96	1160.1	-16.1
Max Von Mises stress (MPa)	Armor	397.14	418.0	+5.3
	Space frame	392.92	401.2	+2.1

APPENDIX C

OPTIMALITY CHECK FOR MASS OPTIMIZATION

Since the variable x_6, thickness of the armor, did not reach the lower or upper bounds after optimization, the final design variables obtained after optimization, shown in Table C.1, is checked for optimality. This is done by varying the optimized value of the design variable by a sensitivity parameter, ϵ, in the positive and negative direction. While varying x_6, the rest of the variables are maintained at the optimized values. The value of ϵ is taken to be ±0.25 mm. Table C.2 shows the results of this optimality check, and from this table it is clear that the SHQA optimized value for x_6 is optimum, since increasing the armor thickness by the value ϵ results in increasing the overall mass, while decreasing x_6 by the parameter ϵ leads to increase of the armor stress beyond the stress limit of 418 MPa.

Table C.1: Comparison between optimized results and the original variables for mass optimization

Parameters	Original design	Final design	Lower limit	Upper limit
x_1	6.4	3.0	3	7
x_2	57.2	40.0	40	110
x_3	15.9	3.0	3	35
x_4	12.7	3.0	3	14
x_5	12.7	3.0	3	14
x_6	32.0	28.0	20	40

Table C.2: Results of the optimality check

Optimized variable	ϵ (mm)	Armor stress (MPa)	Space frame stress (MPa)	Total mass (kg)
x_6	+0.25	416.1	404.5	1047.2
	-0.25	420.1	407.9	1029.8
Original design		397.1	392.9	1383.0
Final design		418.0	406.1	1038.8

APPENDIX D

OPTIMALITY CHECK FOR SHOCK OPTIMIZATION

The minimum point; the final design variables obtained after shock optimization, shown in Table D.1, is checked for optimality. Sensitivity analysis at the SHQA minimum point is conducted by varying each design variable by a value ϵ in the positive and negative direction. While varying one design variable, the rest of the variables are maintained at the optimized values. The value of ϵ is taken to be ±0.5 mm. Since the shock optimization problem comprises of six design variables, a total of 12 points in the neighborhood of the SHQA minimum point are checked for optimality. Table D.2 shows the results at these 12 points and their comparison to the SHQA minimum point. From Table D.2 it is clear that the total mean acceleration of the identified critical points on the space frame, S, is less for the minimum point obtained from SHQA algorithm when compared to the rest of the 12 neighboring points. Hence, the final design, which is a result of optimization using SHQA algorithm, is the optimum point.

Table D.1: Comparison of optimized variables with the original design values for shock optimization

Parameters	Original design	Final design	Lower limit	Upper limit
x_1	6.4	5.6	3	7
x_2	57.2	40.1	40	110
x_3	15.9	20.2	3	35
x_4	12.7	4.1	3	14
x_5	12.7	9.8	3	14
x_6	32.0	38.2	20	40

Table D.2: Results of the optimality check for shock optimization

Optimized variable	ϵ (mm)	Armor stress (MPa)	Space frame stress (MPa)	S (m/s^2)
x_1	+0.5	374.1	383.4	2533.0
	-0.5	373.4	383.3	2757.9
x_2	+0.5	373.8	383.4	2539.0
	-0.5	373.7	383.5	2706.9
x_3	+0.5	374.2	383.2	2701.6
	-0.5	373.3	383.5	2678.5
x_4	+0.5	373.9	383.0	2615.1
	-0.5	373.5	384.4	2552.6
x_5	+0.5	373.8	383.6	2572.5
	-0.5	373.8	383.3	2542.5
x_6	+0.5	366.8	382.7	2724.2
	-0.5	379.4	383.7	2840.0
Original design		397.1	392.9	46109.0
Final design		373.8	383.4	2479.7

APPENDIX E

OFF-THE-SHELF PROGRAM FOR SHOCK OPTIMIZATION

The shock optimization problem was also solved using an off-the-shelf optimization program from Matlab Optimization Toolbox. Similar to mass optimization, the optimization program used from the toolbox was *fmincon* [Appendix B].

The same upper and lower bounds that were used for SHQA are used for *fmincon* algorithm, Table E.1. The *fmincon* optimization algorithm underwent 28 function evaluations and 2 iterations to reach the minimum. The optimization process approximately took 18 hours of computational time. Table E.2 compares the results before and after optimization using the *fmincon* algorithm. While the computational time of *fmincon* is much lesser than that of SHQA, the resulted minimum was higher than SHQA optimized result. Hence, SHQA is a better option to conduct shock optimization on the military vehicle

Table E.1: Comparison of design variables before and after shock optimization using *fmincon* algorithm

Parameters	Original design	Final design	Lower limit	Upper limit
x_1	6.4	7.0	3	7
x_2	57.2	110.0	40	110
x_3	15.9	35.0	3	35
x_4	12.7	14.0	3	14
x_5	12.7	14.0	3	14
x_6	32.0	40.0	20	40

Table E.2: Optimization results using the *fmincon* algorithm

Parameters		Original design	Final design	% change
Mass (kg)	Armor	1119.50	1399.40	+25.0
	Space frame	263.46	565.59	+114.7
Max stress (MPa)	Armor	397.14	381.02	-4.1
	Space frame	392.92	380.18	-3.2
Total mean acceleration (m/s^2)		46,109.00	3145.5	-93.2

APPENDIX F

FORCE HAMMER

The specifications of the force hammer listed in this appendix are from [63].

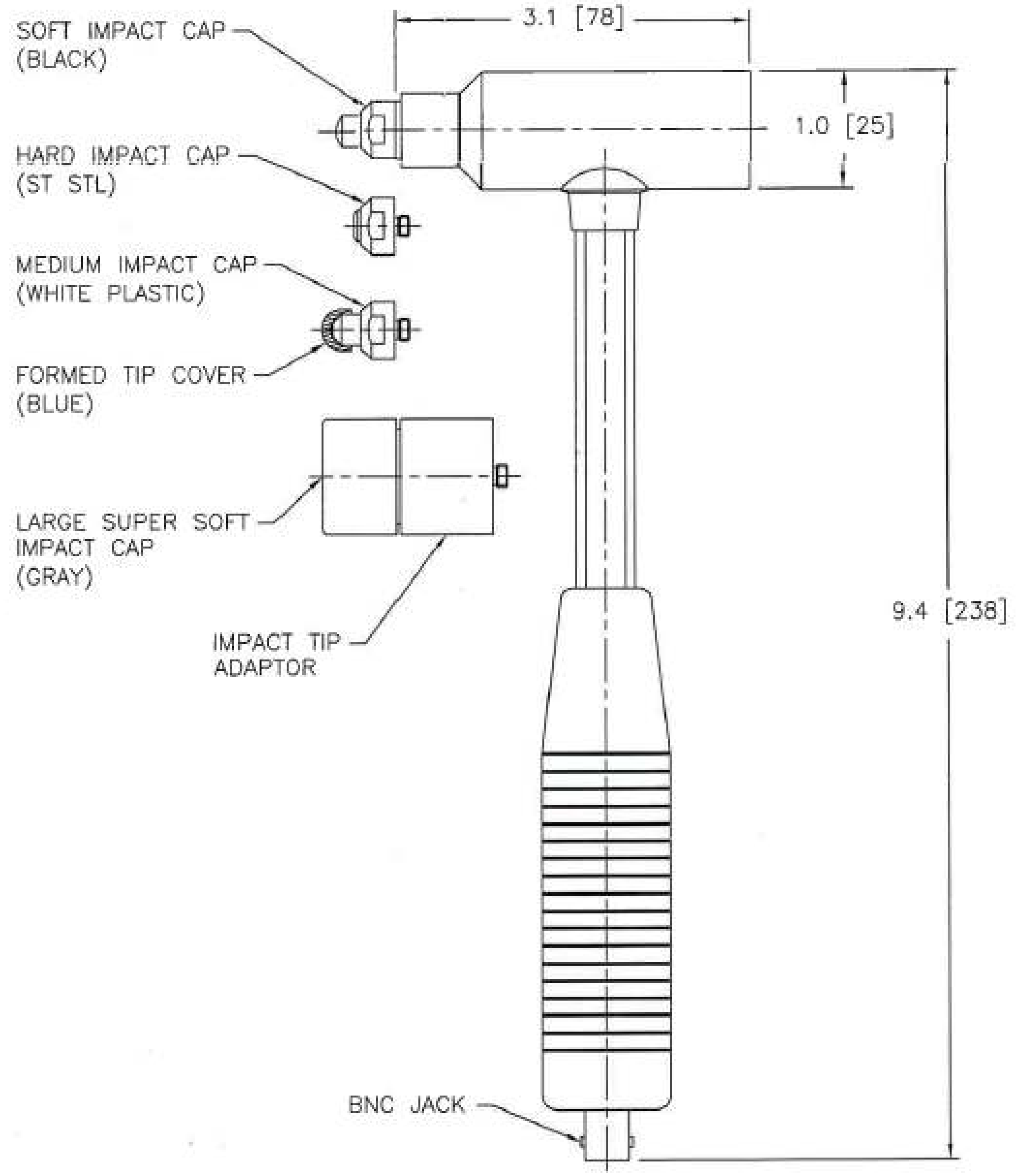

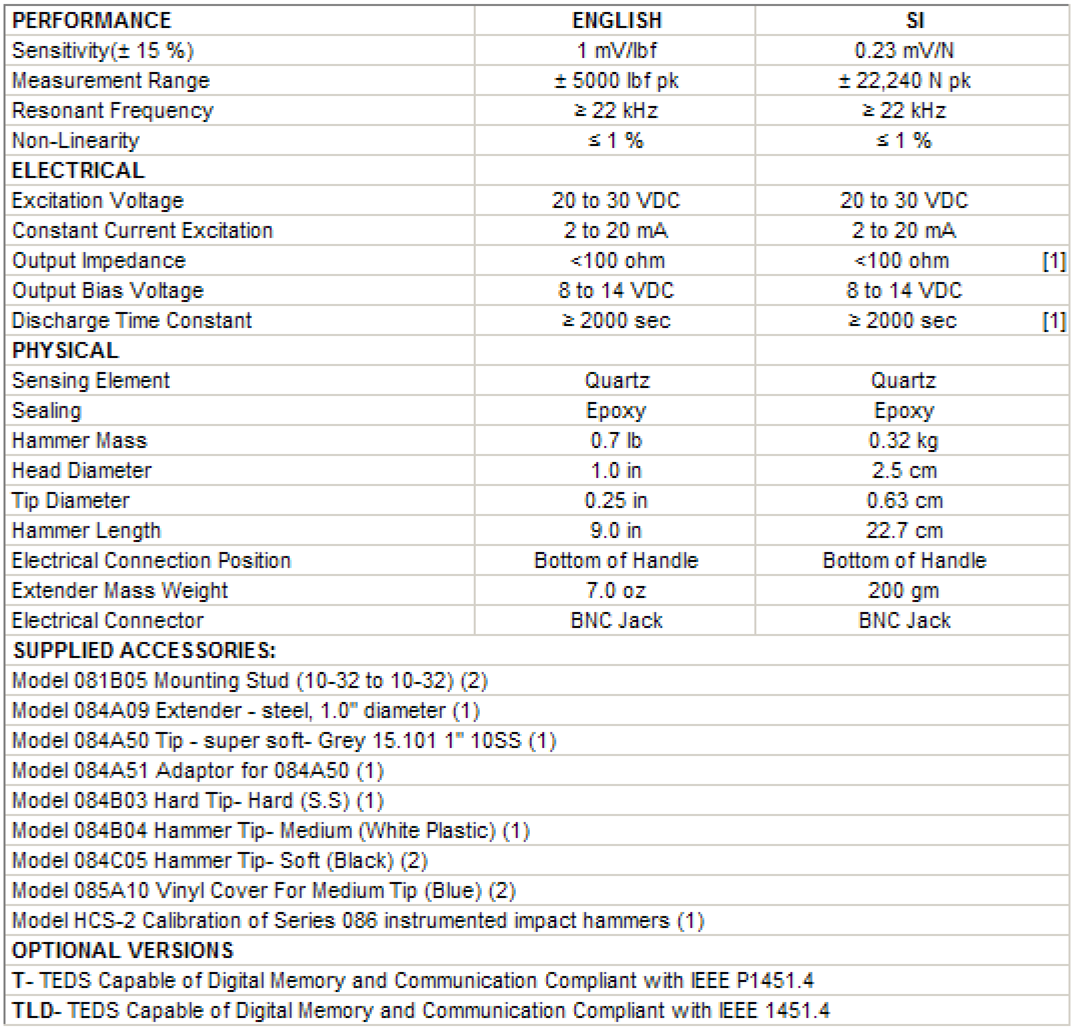

PERFORMANCE	ENGLISH	SI
Sensitivity(± 15 %)	1 mV/lbf	0.23 mV/N
Measurement Range	± 5000 lbf pk	± 22,240 N pk
Resonant Frequency	≥ 22 kHz	≥ 22 kHz
Non-Linearity	≤ 1 %	≤ 1 %
ELECTRICAL		
Excitation Voltage	20 to 30 VDC	20 to 30 VDC
Constant Current Excitation	2 to 20 mA	2 to 20 mA
Output Impedance	<100 ohm	<100 ohm [1]
Output Bias Voltage	8 to 14 VDC	8 to 14 VDC
Discharge Time Constant	≥ 2000 sec	≥ 2000 sec [1]
PHYSICAL		
Sensing Element	Quartz	Quartz
Sealing	Epoxy	Epoxy
Hammer Mass	0.7 lb	0.32 kg
Head Diameter	1.0 in	2.5 cm
Tip Diameter	0.25 in	0.63 cm
Hammer Length	9.0 in	22.7 cm
Electrical Connection Position	Bottom of Handle	Bottom of Handle
Extender Mass Weight	7.0 oz	200 gm
Electrical Connector	BNC Jack	BNC Jack
SUPPLIED ACCESSORIES:		
Model 081B05 Mounting Stud (10-32 to 10-32) (2)		
Model 084A09 Extender - steel, 1.0" diameter (1)		
Model 084A50 Tip - super soft- Grey 15.101 1" 10SS (1)		
Model 084A51 Adaptor for 084A50 (1)		
Model 084B03 Hard Tip- Hard (S.S) (1)		
Model 084B04 Hammer Tip- Medium (White Plastic) (1)		
Model 084C05 Hammer Tip- Soft (Black) (2)		
Model 085A10 Vinyl Cover For Medium Tip (Blue) (2)		
Model HCS-2 Calibration of Series 086 instrumented impact hammers (1)		
OPTIONAL VERSIONS		
T- TEDS Capable of Digital Memory and Communication Compliant with IEEE P1451.4		
TLD- TEDS Capable of Digital Memory and Communication Compliant with IEEE 1451.4		

APPENDIX G

ACCELEROMETER

The specifications of the accelerometer shown in this appendix are from [64].

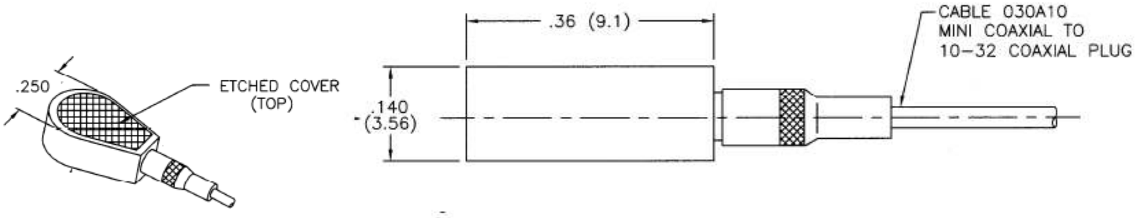

PERFORMANCE	ENGLISH	SI
Sensitivity(± 15 %)	10 mV/g	1.0 mV/(m/s^2)
Measurement Range	± 500 g pk	± 4900 m/s^2 pk
Frequency Range(± 5 %)	1.0 to 10,000 Hz	1.0 to 10,000 Hz
Frequency Range(± 10 %)	0.7 to 13,000 Hz	0.7 to 13,000 Hz
Frequency Range(± 3 dB)	0.3 to 20,000 Hz	0.3 to 20,000 Hz
Resonant Frequency	≥ 50 kHz	≥ 50 kHz
Broadband Resolution(1 to 10,000 Hz)	0.002 g rms	0.02 m/s^2 rms [1]
Non-Linearity	≤ 1 %	≤ 1 % [2]
Transverse Sensitivity	≤ 5 %	≤ 5 %
ENVIRONMENTAL		
Overload Limit(Shock)	± 10,000 g pk	± 98,000 m/s^2 pk
Temperature Range(Operating)	-65 to +250 °F	-54 to +121 °C
Temperature Response	See Graph	See Graph [1]
ELECTRICAL		
Excitation Voltage	18 to 30 VDC	18 to 30 VDC
Constant Current Excitation	2 to 20 mA	2 to 20 mA
Output Impedance	≤ 300 ohm	≤ 300 ohm
Output Bias Voltage	7 to 11 VDC	7 to 11 VDC
Discharge Time Constant	1.0 to 3.5 sec	1.0 to 3.5 sec
Settling Time(within 10% of bias)	<3 sec	<3 sec
Spectral Noise(1 Hz)	800 µg/√Hz	7840 (µm/sec^2)/√Hz [1]
Spectral Noise(10 Hz)	250 µg/√Hz	2450 (µm/sec^2)/√Hz [1]
Spectral Noise(100 Hz)	60 µg/√Hz	590 (µm/sec^2)/√Hz [1]
Spectral Noise(1 kHz)	20 µg/√Hz	196 (µm/sec^2)/√Hz [1]
Spectral Noise(10 kHz)	10 µg/√Hz	98 (µm/sec^2)/√Hz [1]
Electrical Isolation(Base)	>10^8 ohm	>10^8 ohm
PHYSICAL		
Sensing Element	Ceramic	Ceramic
Sensing Geometry	Shear	Shear
Housing Material	Anodized Aluminum	Anodized Aluminum
Sealing	Epoxy	Epoxy
Size (Height x Length x Width)	0.14 in x 0.45 in x 0.25 in	3.6 mm x 11.4 mm x 6.4 mm
Weight	0.017 oz	0.5 gm [1]
Electrical Connector	3-56 Coaxial Jack	3-56 Coaxial Jack
Electrical Connection Position	Side	Side
Mounting	Adhesive	Adhesive
SUPPLIED ACCESSORIES:		
Model 030A10 Coax Cable, 10 ft (3 m), 3-56 plug to 10-32 plug. (1)		
Model 039A27 One-piece removal tool for Models 352C22, 357C10, 352A21, & 357A09 (1)		
Model 080A109 Petro Wax (1)		
Model ACS-1 NIST traceable frequency response (10 Hz to upper 5% point). (1)		

APPENDIX H

SIGNAL CONDITIONER

The specifications of the signal conditioner are taken from [65].

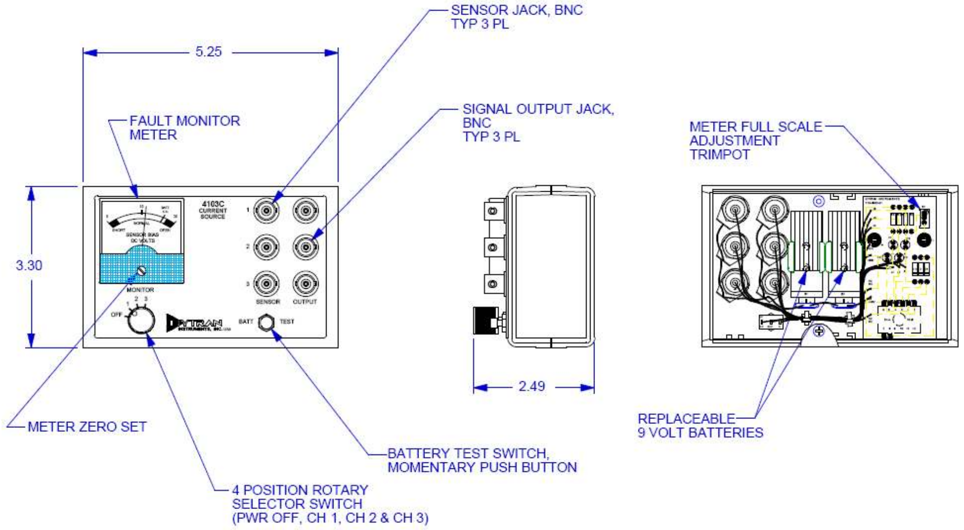

SPECIFICATION	VALUE	UNITS
COMMON SPECIFICATIONS, EACH CHANNEL		
SENSOR SUPPLY CURRENT, FIXED,	2.0	mA
COMPLIANCE VOLTAGE	+18	VDC
VOLTAGE GAIN	UNITY	
COUPLING TIME CONSTANT INTO 10 MEGOHM LOAD	10	SEC
COUPLING TIME CONSTANT INTO 1 MEGOHM LOAD	5	SEC
LOW FREQUENCY -3db FREQ., 10 MEGOHM LOAD	0.016	Hz
LOW FREQUENCY -3db FREQ., 1 MEGOHM LOAD	.032	Hz
HIGH FREQUENCY RESPONSE	DETERMINED BY SENSOR, CABLE LENGTH AND SIGNAL LEVEL	
COUPLING CAPACITOR, NOM.	10	μF
PULLDOWN RESISTOR	1.0	MEGOHMS
MONITOR VOLTMETER RANGE, F.S.	20	VDC
ELECTRICAL NOISE, WIDEBAND	60	μV, RMS
SENSOR CONNECTOR	BNC	JACK
OUTPUT CONNECTOR	BNC	JACK
GENERAL SPECIFICATIONS		
POWER SOURCE △1	9 VOLT BATTERIES	2
BATTERY LIFE, TYP.	40	HOURS
SIZE (H x W x D)	2.5 x 5.2 x 3.3	INCHES
WEIGHT	12	OUNCES

APPENDIX I

CALIBRATOR (HAND HELD SHAKER)

The information of the Calibrator shown below is taken from [66].

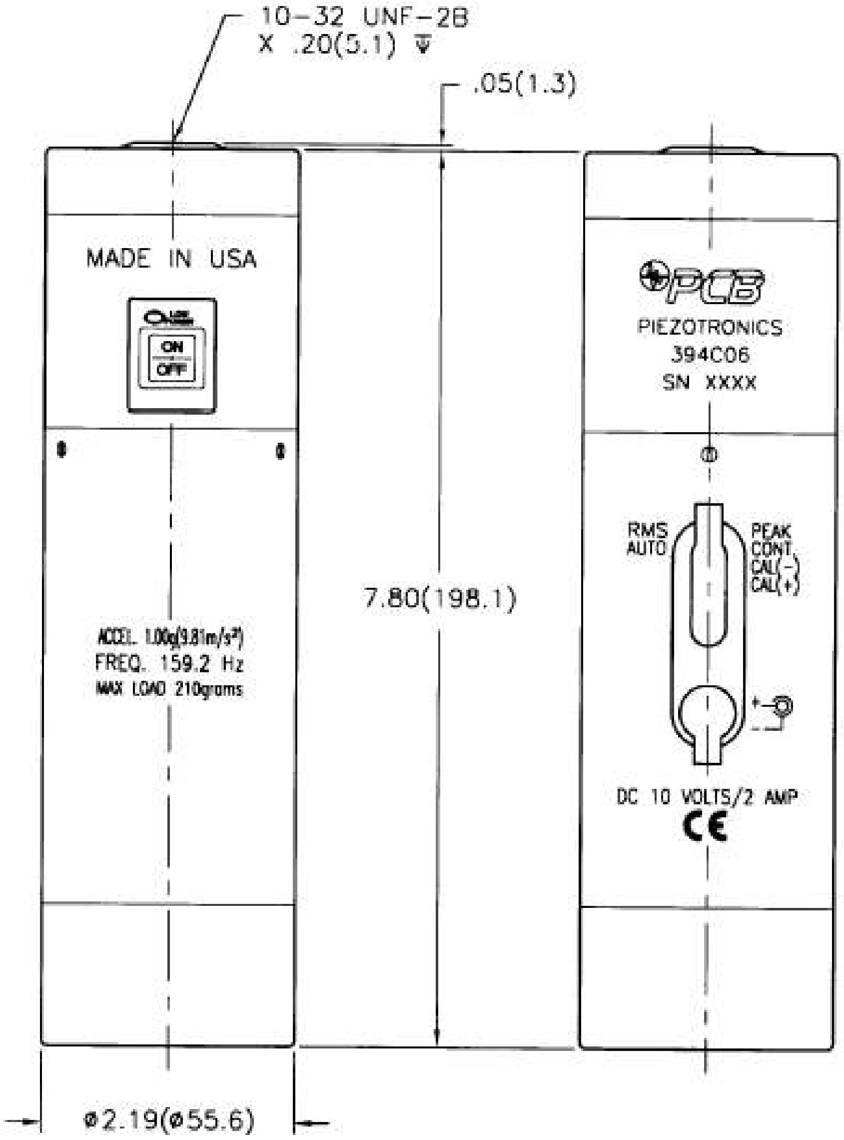

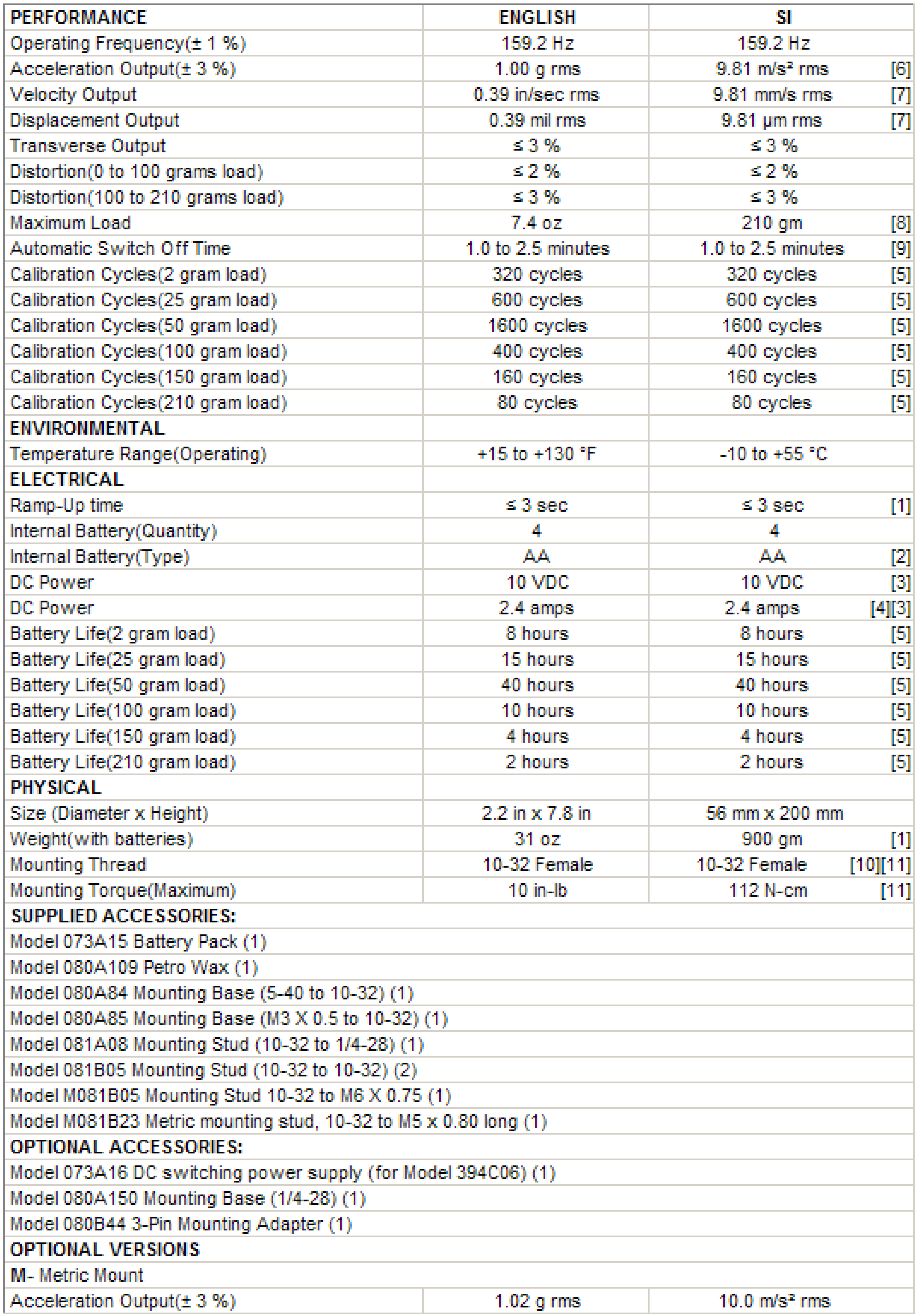

PERFORMANCE	ENGLISH	SI	
Operating Frequency(± 1 %)	159.2 Hz	159.2 Hz	
Acceleration Output(± 3 %)	1.00 g rms	9.81 m/s² rms	[6]
Velocity Output	0.39 in/sec rms	9.81 mm/s rms	[7]
Displacement Output	0.39 mil rms	9.81 µm rms	[7]
Transverse Output	≤ 3 %	≤ 3 %	
Distortion(0 to 100 grams load)	≤ 2 %	≤ 2 %	
Distortion(100 to 210 grams load)	≤ 3 %	≤ 3 %	
Maximum Load	7.4 oz	210 gm	[8]
Automatic Switch Off Time	1.0 to 2.5 minutes	1.0 to 2.5 minutes	[9]
Calibration Cycles(2 gram load)	320 cycles	320 cycles	[5]
Calibration Cycles(25 gram load)	600 cycles	600 cycles	[5]
Calibration Cycles(50 gram load)	1600 cycles	1600 cycles	[5]
Calibration Cycles(100 gram load)	400 cycles	400 cycles	[5]
Calibration Cycles(150 gram load)	160 cycles	160 cycles	[5]
Calibration Cycles(210 gram load)	80 cycles	80 cycles	[5]
ENVIRONMENTAL			
Temperature Range(Operating)	+15 to +130 °F	-10 to +55 °C	
ELECTRICAL			
Ramp-Up time	≤ 3 sec	≤ 3 sec	[1]
Internal Battery(Quantity)	4	4	
Internal Battery(Type)	AA	AA	[2]
DC Power	10 VDC	10 VDC	[3]
DC Power	2.4 amps	2.4 amps	[4][3]
Battery Life(2 gram load)	8 hours	8 hours	[5]
Battery Life(25 gram load)	15 hours	15 hours	[5]
Battery Life(50 gram load)	40 hours	40 hours	[5]
Battery Life(100 gram load)	10 hours	10 hours	[5]
Battery Life(150 gram load)	4 hours	4 hours	[5]
Battery Life(210 gram load)	2 hours	2 hours	[5]
PHYSICAL			
Size (Diameter x Height)	2.2 in x 7.8 in	56 mm x 200 mm	
Weight(with batteries)	31 oz	900 gm	[1]
Mounting Thread	10-32 Female	10-32 Female	[10][11]
Mounting Torque(Maximum)	10 in-lb	112 N-cm	[11]
SUPPLIED ACCESSORIES:			
Model 073A15 Battery Pack (1)			
Model 080A109 Petro Wax (1)			
Model 080A84 Mounting Base (5-40 to 10-32) (1)			
Model 080A85 Mounting Base (M3 X 0.5 to 10-32) (1)			
Model 081A08 Mounting Stud (10-32 to 1/4-28) (1)			
Model 081B05 Mounting Stud (10-32 to 10-32) (2)			
Model M081B05 Mounting Stud 10-32 to M6 X 0.75 (1)			
Model M081B23 Metric mounting stud, 10-32 to M5 x 0.80 long (1)			
OPTIONAL ACCESSORIES:			
Model 073A16 DC switching power supply (for Model 394C06) (1)			
Model 080A150 Mounting Base (1/4-28) (1)			
Model 080B44 3-Pin Mounting Adapter (1)			
OPTIONAL VERSIONS			
M- Metric Mount			
Acceleration Output(± 3 %)	1.02 g rms	10.0 m/s² rms	

APPENDIX J

CALIBRATION OF THE ACCELEROMETER

In order to calibrate the accelerometer, it is stuck on top of the calibrator. The wire attached to the accelerometer is connected to the input sensor port of the signal conditioner. The output of the signal conditioner is connected to one of the input channels of the signal analyzer. The output signal obtained from the signal analyzer is viewed on a computer having the SignalCalc software, by connecting the signal analyzer to the computer. Figure J.1 shows the flowchart of the experimental setup for calibrating the accelerometer.

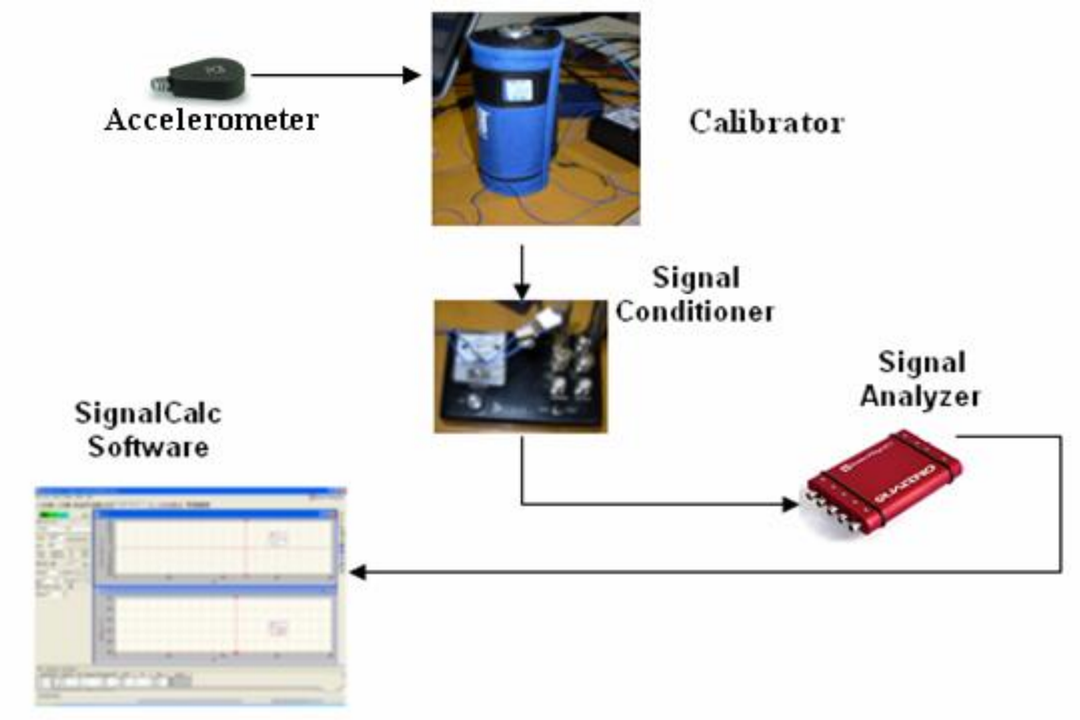

Figure J.1: Flowchart of the setup for accelerometer calibration

When the calibrator is switched on, it starts vibrating and the accelerometer captures the acceleration of the vibrations, which are then processed through the signal conditioner and signal analyzer. The SignalCalc software gives the sensitivity value of the accelerometer based on the recorded acceleration signal. This is then compared with the specified sensitivity, from the data sheet provided, of the accelerometer.

APPENDIX K

CALIBRATION OF THE FORCE HAMMER

A cylindrical block of metal of known mass is hung from and A-shaped frame by means of rope as shown in Figure K.1. An accelerometer is glued onto one end of the metal block, while the other end is impacted by the force hammer to be calibrated. The force and acceleration signals from the hammer and accelerometer respectively are recorded onto the SignalCalc software, after going through the signal conditioner and signal analyzer boxes. In the SignalCalc software, from the force and acceleration signals obtained, the accelerance value is obtained. Accelerance is measure of ratio of acceleration and force. Hence, by taking the inverse of accelerance the mass of the metal block can be obtained. This obtained mass of the block is compared with the known value. If the experimentally obtained mass of the block does not match with the known value, the sensitivity of the force hammer is changed and the experiment is repeated. This is carried out till there is good match between the experimental value and known value of mass. Figure K.2 gives the flowchart of the experimental setup for calibration of the force hammer.

Figure K.1: Cylindrical metal block hanging from an A-frame

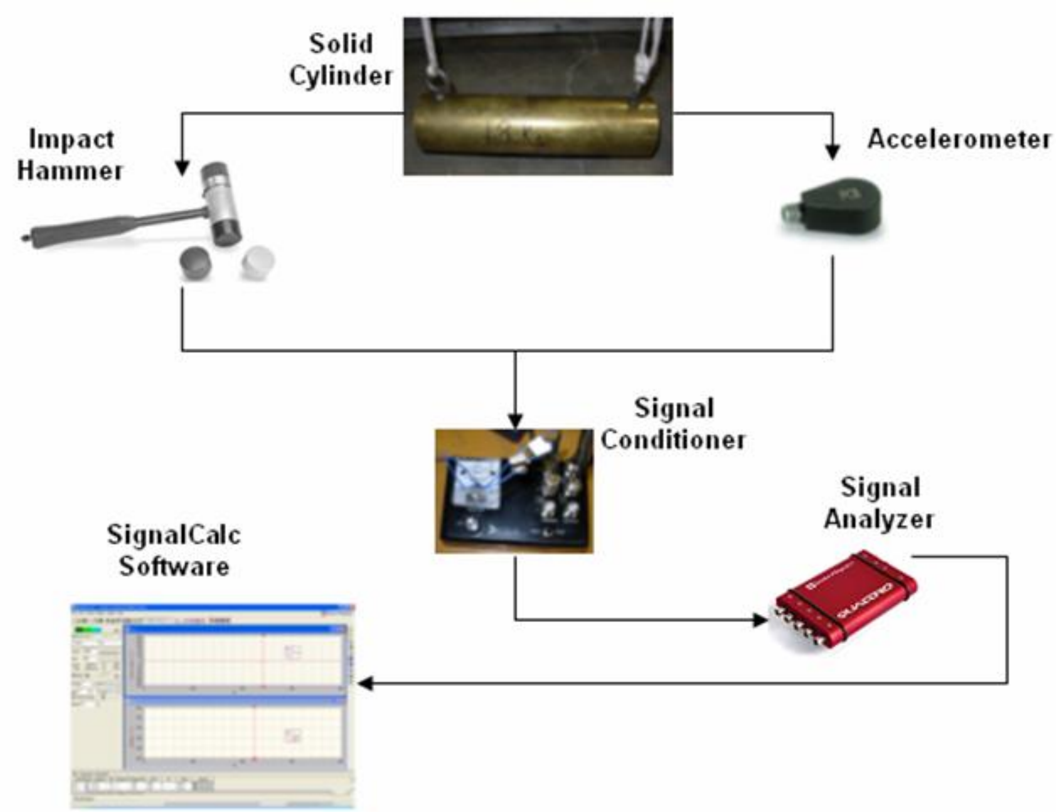

Figure K.2: Flowchart of the setup for force hammer calibration

APPENDIX L

MATLAB PROGRAM FOR CREATING THE VARIABLE CODE

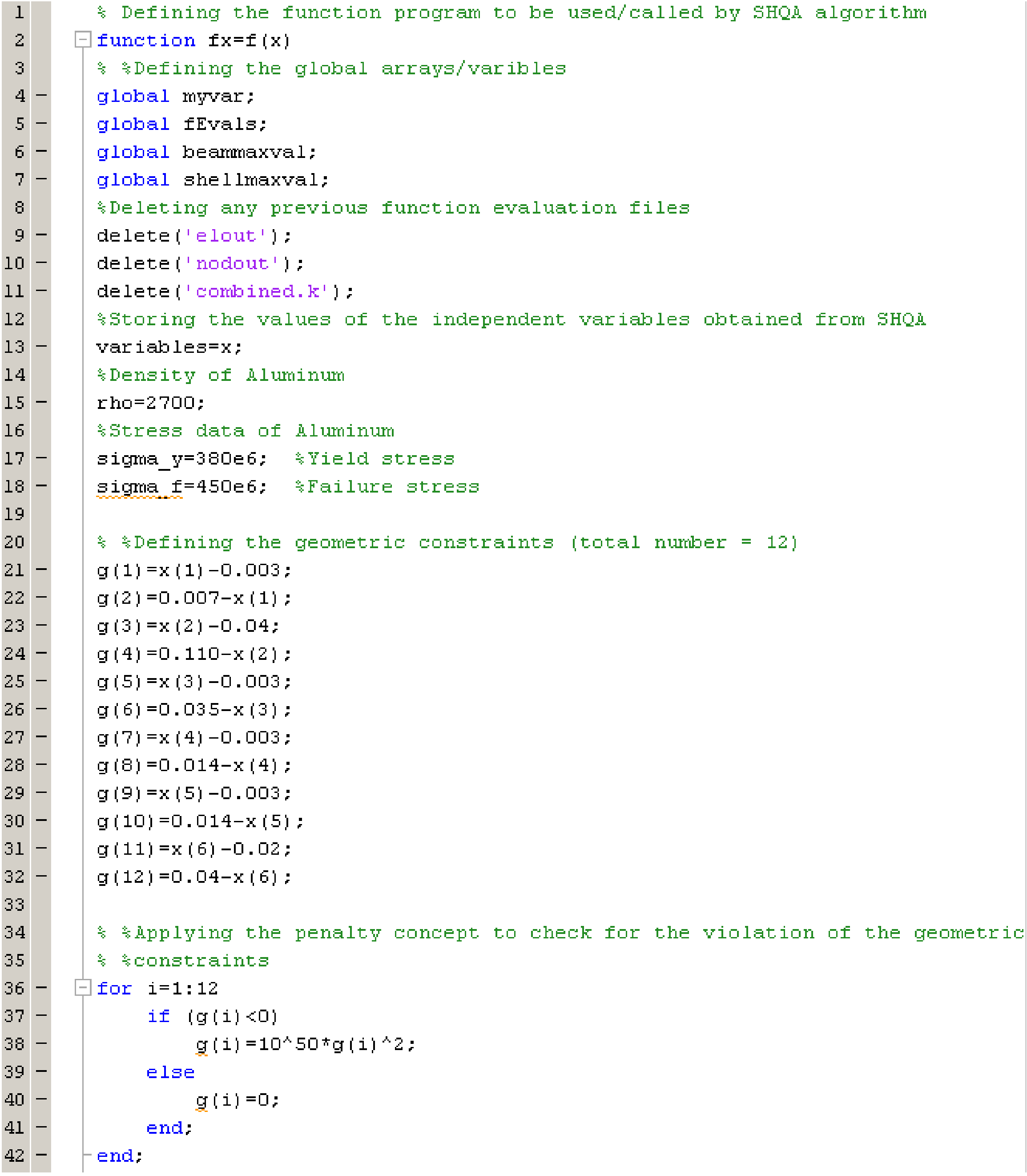

```
% Defining the function program to be used/called by SHQA algorithm
function fx=f(x)
% %Defining the global arrays/varibles
global myvar;
global fEvals;
global beammaxval;
global shellmaxval;
%Deleting any previous function evaluation files
delete('elout');
delete('nodout');
delete('combined.k');
%Storing the values of the independent variables obtained from SHQA
variables=x;
%Density of Aluminum
rho=2700;
%Stress data of Aluminum
sigma_y=380e6;  %Yield stress
sigma_f=450e6;  %Failure stress

% %Defining the geometric constraints (total number = 12)
g(1)=x(1)-0.003;
g(2)=0.007-x(1);
g(3)=x(2)-0.04;
g(4)=0.110-x(2);
g(5)=x(3)-0.003;
g(6)=0.035-x(3);
g(7)=x(4)-0.003;
g(8)=0.014-x(4);
g(9)=x(5)-0.003;
g(10)=0.014-x(5);
g(11)=x(6)-0.02;
g(12)=0.04-x(6);

% %Applying the penalty concept to check for the violation of the geometric
% %constraints
for i=1:12
    if (g(i)<0)
        g(i)=10^50*g(i)^2;
    else
        g(i)=0;
    end;
end;
```

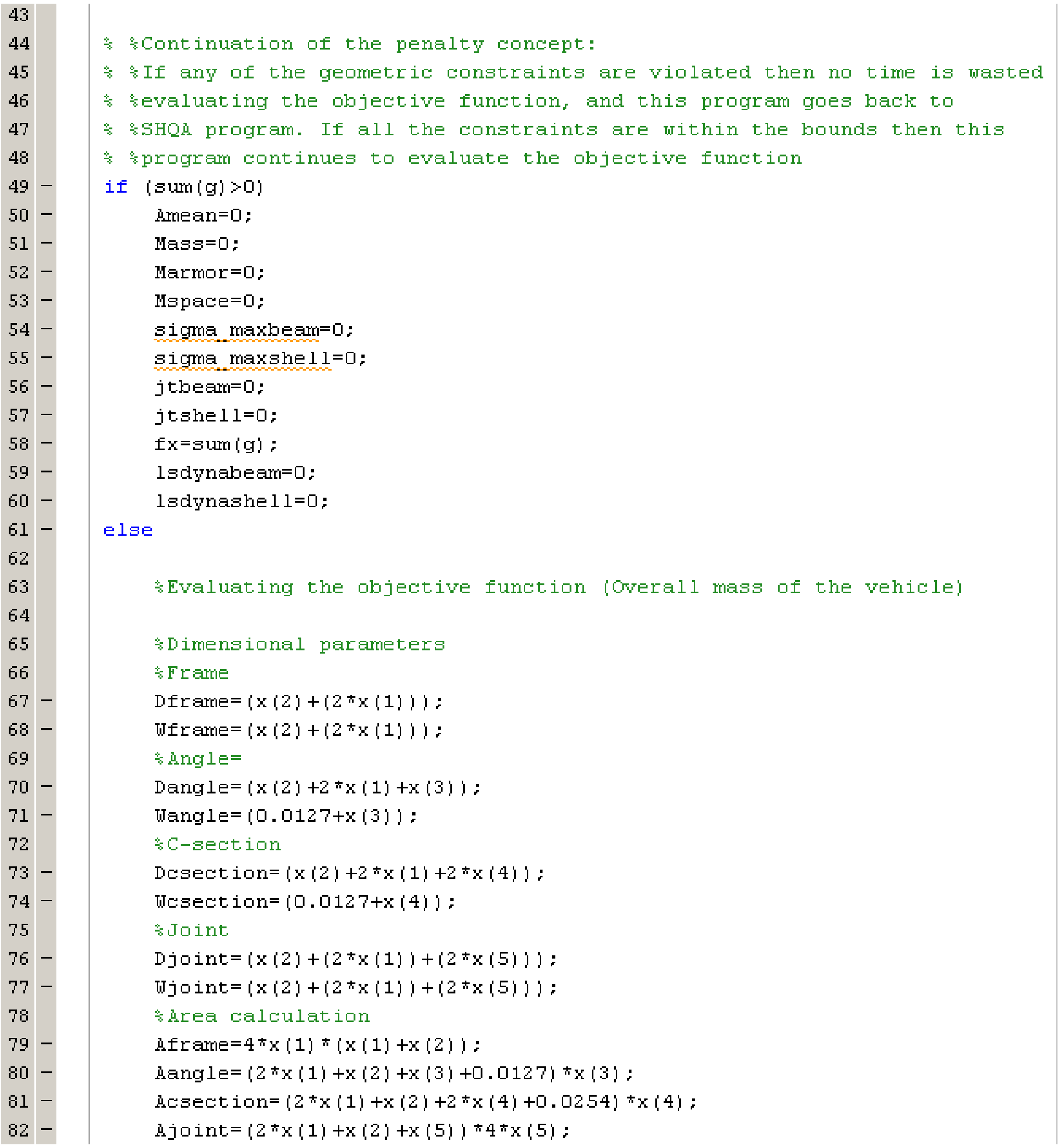

```
% %Continuation of the penalty concept:
% %If any of the geometric constraints are violated then no time is wasted
% %evaluating the objective function, and this program goes back to
% %SHQA program. If all the constraints are within the bounds then this
% %program continues to evaluate the objective function
if (sum(g)>0)
    Amean=0;
    Mass=0;
    Marmor=0;
    Mspace=0;
    sigma_maxbeam=0;
    sigma_maxshell=0;
    jtbeam=0;
    jtshell=0;
    fx=sum(g);
    lsdynabeam=0;
    lsdynashell=0;
else

    %Evaluating the objective function (Overall mass of the vehicle)

    %Dimensional parameters
    %Frame
    Dframe=(x(2)+(2*x(1)));
    Wframe=(x(2)+(2*x(1)));
    %Angle=
    Dangle=(x(2)+2*x(1)+x(3));
    Wangle=(0.0127+x(3));
    %C-section
    Dcsection=(x(2)+2*x(1)+2*x(4));
    Wcsection=(0.0127+x(4));
    %Joint
    Djoint=(x(2)+(2*x(1))+(2*x(5)));
    Wjoint=(x(2)+(2*x(1))+(2*x(5)));
    %Area calculation
    Aframe=4*x(1)*(x(1)+x(2));
    Aangle=(2*x(1)+x(2)+x(3)+0.0127)*x(3);
    Acsection=(2*x(1)+x(2)+2*x(4)+0.0254)*x(4);
    Ajoint=(2*x(1)+x(2)+x(5))*4*x(5);
```

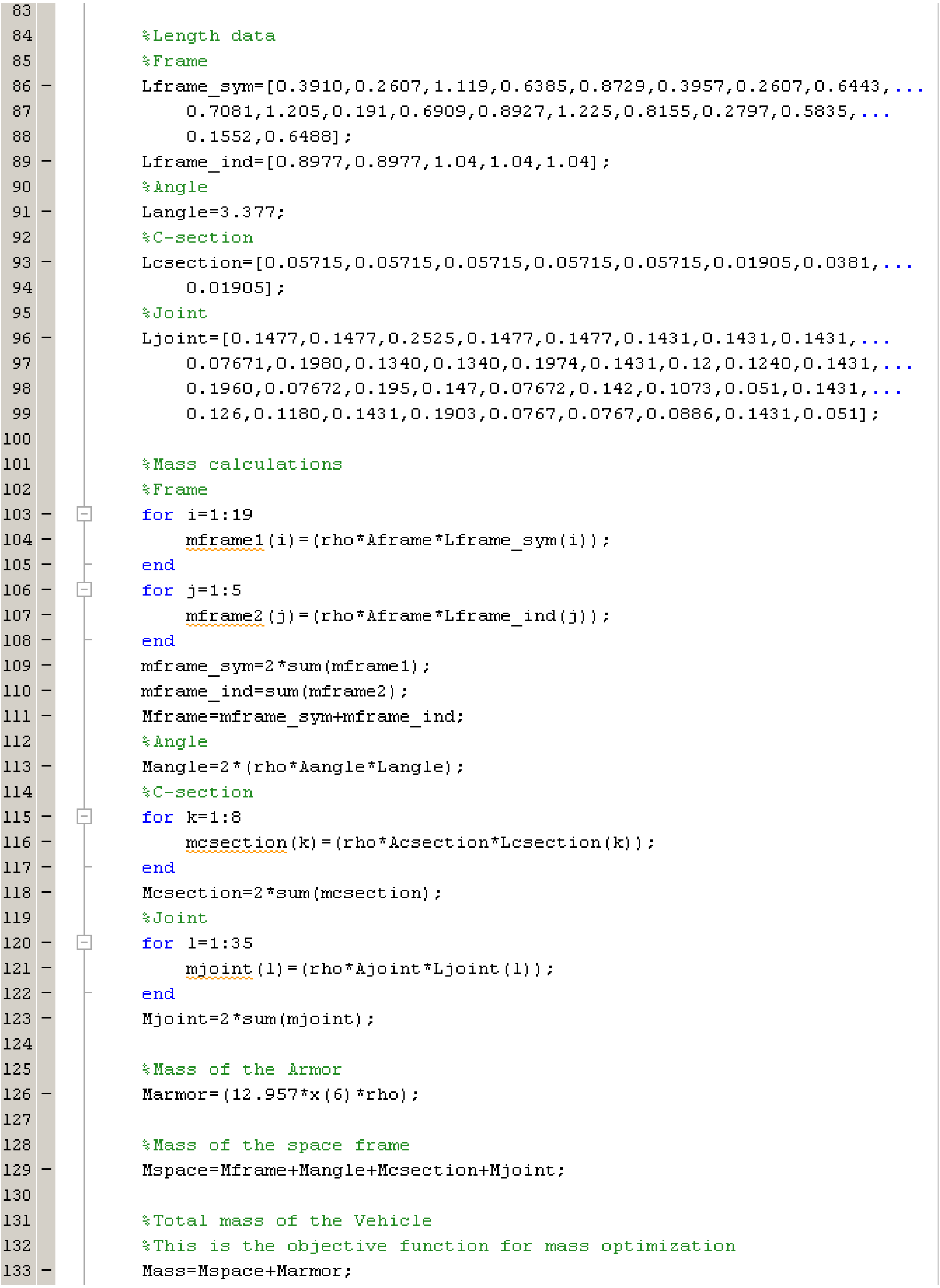

```

%Length data
%Frame
Lframe_sym=[0.3910,0.2607,1.119,0.6385,0.8729,0.3957,0.2607,0.6443,...
    0.7081,1.205,0.191,0.6909,0.8927,1.225,0.8155,0.2797,0.5835,...
    0.1552,0.6488];
Lframe_ind=[0.8977,0.8977,1.04,1.04,1.04];
%Angle
Langle=3.377;
%C-section
Lcsection=[0.05715,0.05715,0.05715,0.05715,0.05715,0.01905,0.0381,...
    0.01905];
%Joint
Ljoint=[0.1477,0.1477,0.2525,0.1477,0.1477,0.1431,0.1431,0.1431,...
    0.07671,0.1980,0.1340,0.1340,0.1974,0.1431,0.12,0.1240,0.1431,...
    0.1960,0.07672,0.195,0.147,0.07672,0.142,0.1073,0.051,0.1431,...
    0.126,0.1180,0.1431,0.1903,0.0767,0.0767,0.0886,0.1431,0.051];

%Mass calculations
%Frame
for i=1:19
    mframe1(i)=(rho*Aframe*Lframe_sym(i));
end
for j=1:5
    mframe2(j)=(rho*Aframe*Lframe_ind(j));
end
mframe_sym=2*sum(mframe1);
mframe_ind=sum(mframe2);
Mframe=mframe_sym+mframe_ind;
%Angle
Mangle=2*(rho*Aangle*Langle);
%C-section
for k=1:8
    mcsection(k)=(rho*Acsection*Lcsection(k));
end
Mcsection=2*sum(mcsection);
%Joint
for l=1:35
    mjoint(l)=(rho*Ajoint*Ljoint(l));
end
Mjoint=2*sum(mjoint);

%Mass of the Armor
Marmor=(12.957*x(6)*rho);

%Mass of the space frame
Mspace=Mframe+Mangle+Mcsection+Mjoint;

%Total mass of the Vehicle
%This is the objective function for mass optimization
Mass=Mspace+Marmor;
```

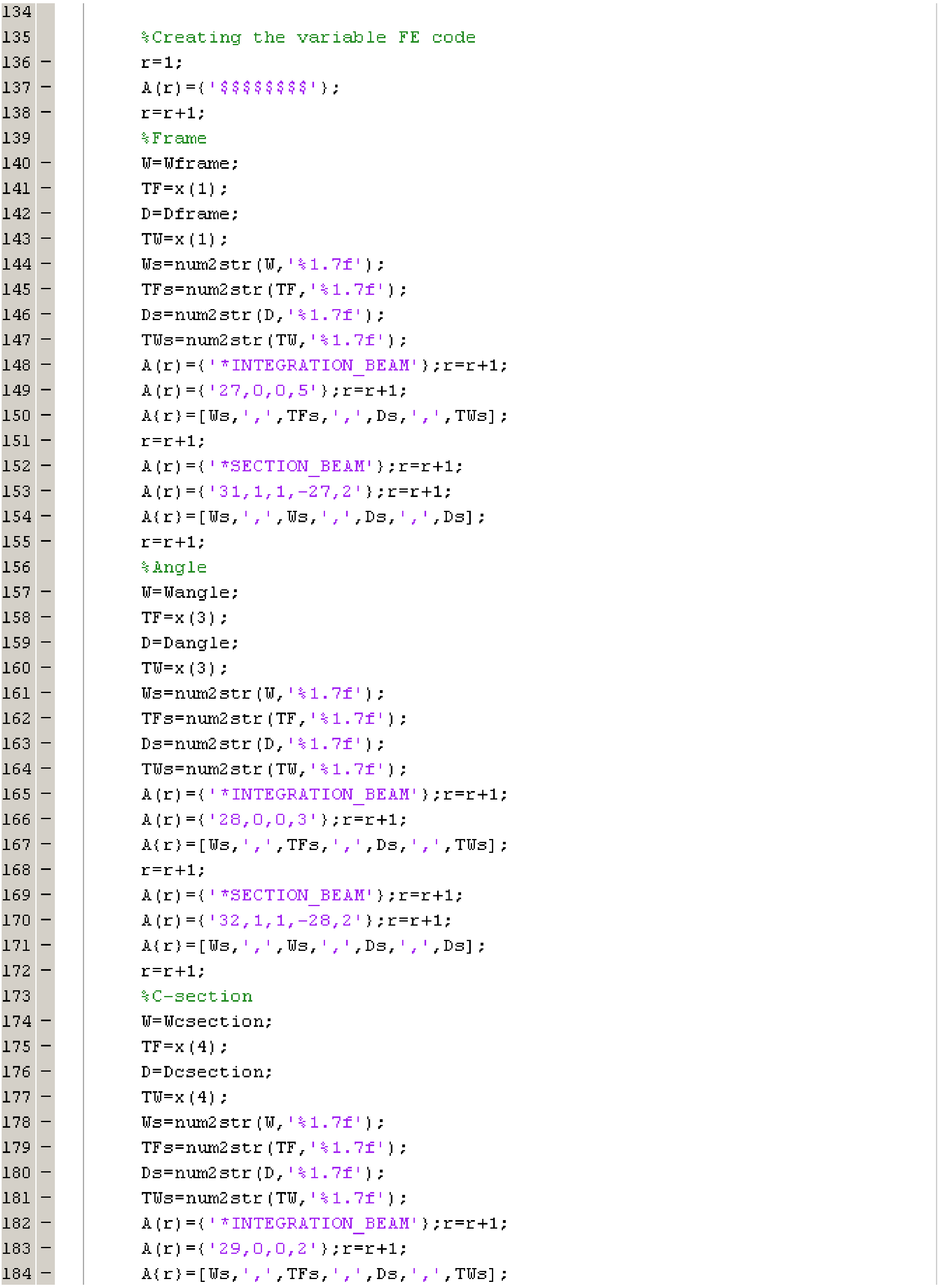

```

%Creating the variable FE code
r=1;
A(r)={'$$$$$$$$'};
r=r+1;
%Frame
W=Wframe;
TF=x(1);
D=Dframe;
TW=x(1);
Ws=num2str(W,'%1.7f');
TFs=num2str(TF,'%1.7f');
Ds=num2str(D,'%1.7f');
TWs=num2str(TW,'%1.7f');
A(r)={'*INTEGRATION_BEAM'};r=r+1;
A(r)={'27,0,0,5'};r=r+1;
A{r}=[Ws,',',TFs,',',Ds,',',TWs];
r=r+1;
A(r)={'*SECTION_BEAM'};r=r+1;
A(r)={'31,1,1,-27,2'};r=r+1;
A{r}=[Ws,',',Ws,',',Ds,',',Ds];
r=r+1;
%Angle
W=Wangle;
TF=x(3);
D=Dangle;
TW=x(3);
Ws=num2str(W,'%1.7f');
TFs=num2str(TF,'%1.7f');
Ds=num2str(D,'%1.7f');
TWs=num2str(TW,'%1.7f');
A(r)={'*INTEGRATION_BEAM'};r=r+1;
A(r)={'28,0,0,3'};r=r+1;
A{r}=[Ws,',',TFs,',',Ds,',',TWs];
r=r+1;
A(r)={'*SECTION_BEAM'};r=r+1;
A(r)={'32,1,1,-28,2'};r=r+1;
A{r}=[Ws,',',Ws,',',Ds,',',Ds];
r=r+1;
%C-section
W=Wcsection;
TF=x(4);
D=Dcsection;
TW=x(4);
Ws=num2str(W,'%1.7f');
TFs=num2str(TF,'%1.7f');
Ds=num2str(D,'%1.7f');
TWs=num2str(TW,'%1.7f');
A(r)={'*INTEGRATION_BEAM'};r=r+1;
A(r)={'29,0,0,2'};r=r+1;
A{r}=[Ws,',',TFs,',',Ds,',',TWs];
```

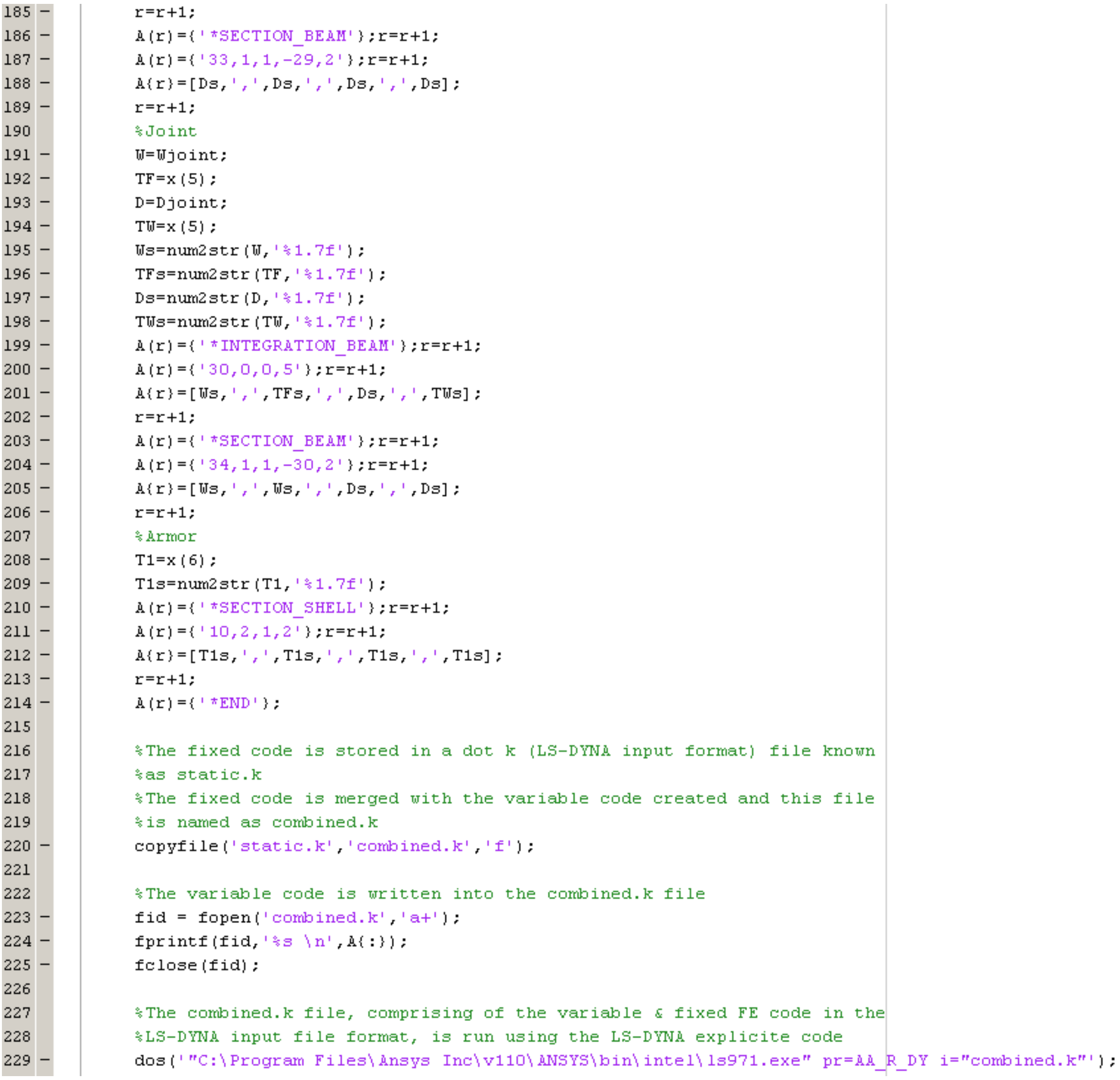

```
r=r+1;
A(r)={'*SECTION_BEAM'};r=r+1;
A(r)={'33,1,1,-29,2'};r=r+1;
A(r)=[Ds,',',Ds,',',Ds,',',Ds];
r=r+1;
%Joint
W=Wjoint;
TF=x(5);
D=Djoint;
TW=x(5);
Ws=num2str(W,'%1.7f');
TFs=num2str(TF,'%1.7f');
Ds=num2str(D,'%1.7f');
TWs=num2str(TW,'%1.7f');
A(r)={'*INTEGRATION_BEAM'};r=r+1;
A(r)={'30,0,0,5'};r=r+1;
A(r)=[Ws,',',TFs,',',Ds,',',TWs];
r=r+1;
A(r)={'*SECTION_BEAM'};r=r+1;
A(r)={'34,1,1,-30,2'};r=r+1;
A(r)=[Ws,',',Ws,',',Ds,',',Ds];
r=r+1;
%Armor
T1=x(6);
T1s=num2str(T1,'%1.7f');
A(r)={'*SECTION_SHELL'};r=r+1;
A(r)={'10,2,1,2'};r=r+1;
A(r)=[T1s,',',T1s,',',T1s,',',T1s];
r=r+1;
A(r)={'*END'};

%The fixed code is stored in a dot k (LS-DYNA input format) file known
%as static.k
%The fixed code is merged with the variable code created and this file
%is named as combined.k
copyfile('static.k','combined.k','f');

%The variable code is written into the combined.k file
fid = fopen('combined.k','a+');
fprintf(fid,'%s \n',A{:});
fclose(fid);

%The combined.k file, comprising of the variable & fixed FE code in the
%LS-DYNA input file format, is run using the LS-DYNA explicite code
dos('"C:\Program Files\Ansys Inc\v110\ANSYS\bin\intel\ls971.exe" pr=AA_R_DY i="combined.k"');
```

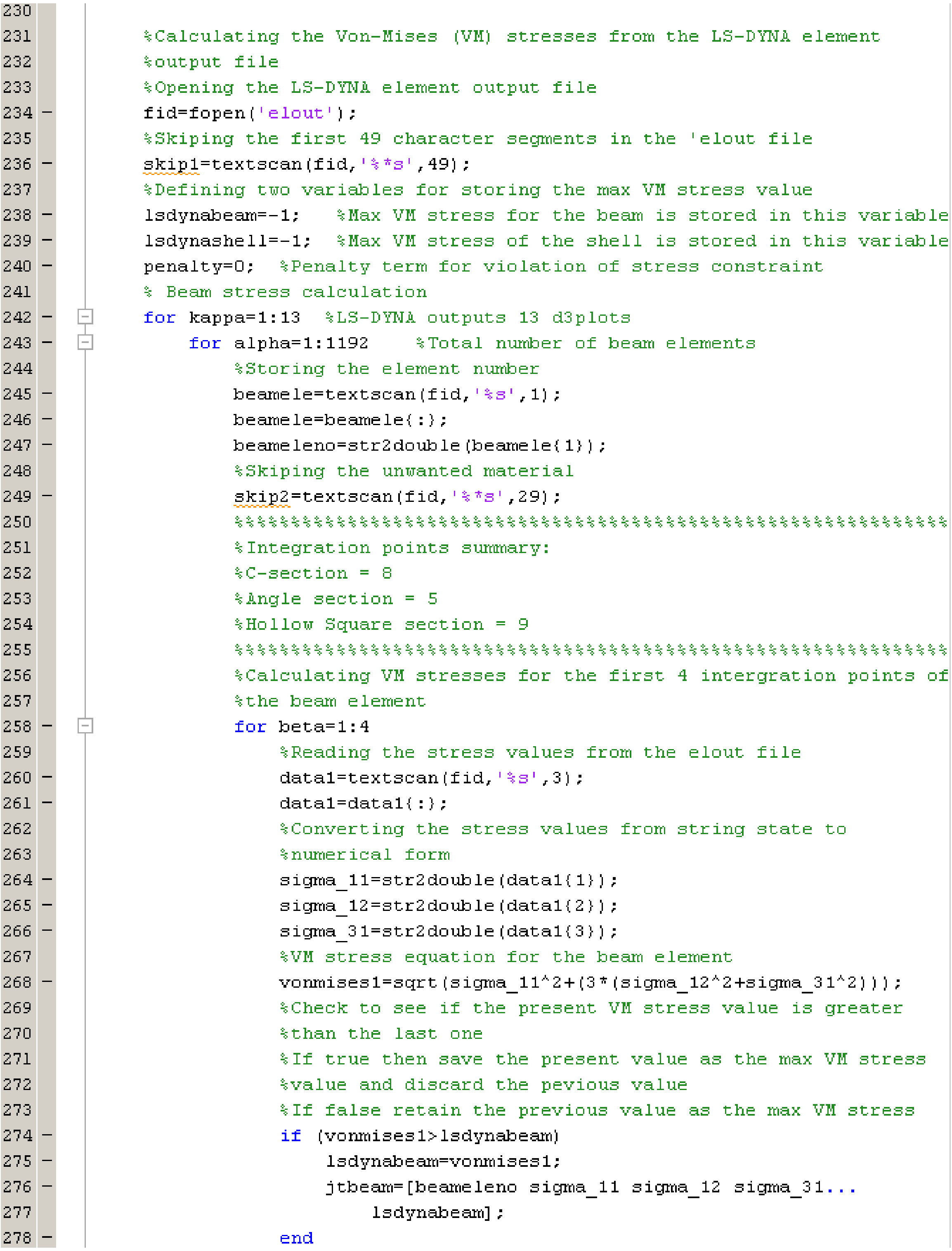

```
%Calculating the Von-Mises (VM) stresses from the LS-DYNA element
%output file
%Opening the LS-DYNA element output file
fid=fopen('elout');
%Skiping the first 49 character segments in the 'elout file
skip1=textscan(fid,'%*s',49);
%Defining two variables for storing the max VM stress value
lsdynabeam=-1;   %Max VM stress for the beam is stored in this variable
lsdynashell=-1;  %Max VM stress of the shell is stored in this variable
penalty=0;  %Penalty term for violation of stress constraint
% Beam stress calculation
for kappa=1:13  %LS-DYNA outputs 13 d3plots
    for alpha=1:1192    %Total number of beam elements
        %Storing the element number
        beamele=textscan(fid,'%s',1);
        beamele=beamele{:};
        beameleno=str2double(beamele{1});
        %Skiping the unwanted material
        skip2=textscan(fid,'%*s',29);
        %%%%%%%%%%%%%%%%%%%%%%%%%%%%%%%%%%%%%%%%%%%%%%%%%%%%%%%%%%%%%%%
        %Integration points summary:
        %C-section = 8
        %Angle section = 5
        %Hollow Square section = 9
        %%%%%%%%%%%%%%%%%%%%%%%%%%%%%%%%%%%%%%%%%%%%%%%%%%%%%%%%%%%%%%%
        %Calculating VM stresses for the first 4 intergration points of
        %the beam element
        for beta=1:4
            %Reading the stress values from the elout file
            data1=textscan(fid,'%s',3);
            data1=data1{:};
            %Converting the stress values from string state to
            %numerical form
            sigma_11=str2double(data1{1});
            sigma_12=str2double(data1{2});
            sigma_31=str2double(data1{3});
            %VM stress equation for the beam element
            vonmises1=sqrt(sigma_11^2+(3*(sigma_12^2+sigma_31^2)));
            %Check to see if the present VM stress value is greater
            %than the last one
            %If true then save the present value as the max VM stress
            %value and discard the pevious value
            %If false retain the previous value as the max VM stress
            if (vonmises1>lsdynabeam)
                lsdynabeam=vonmises1;
                jtbeam=[beameleno sigma_11 sigma_12 sigma_31...
                    lsdynabeam];
            end
```

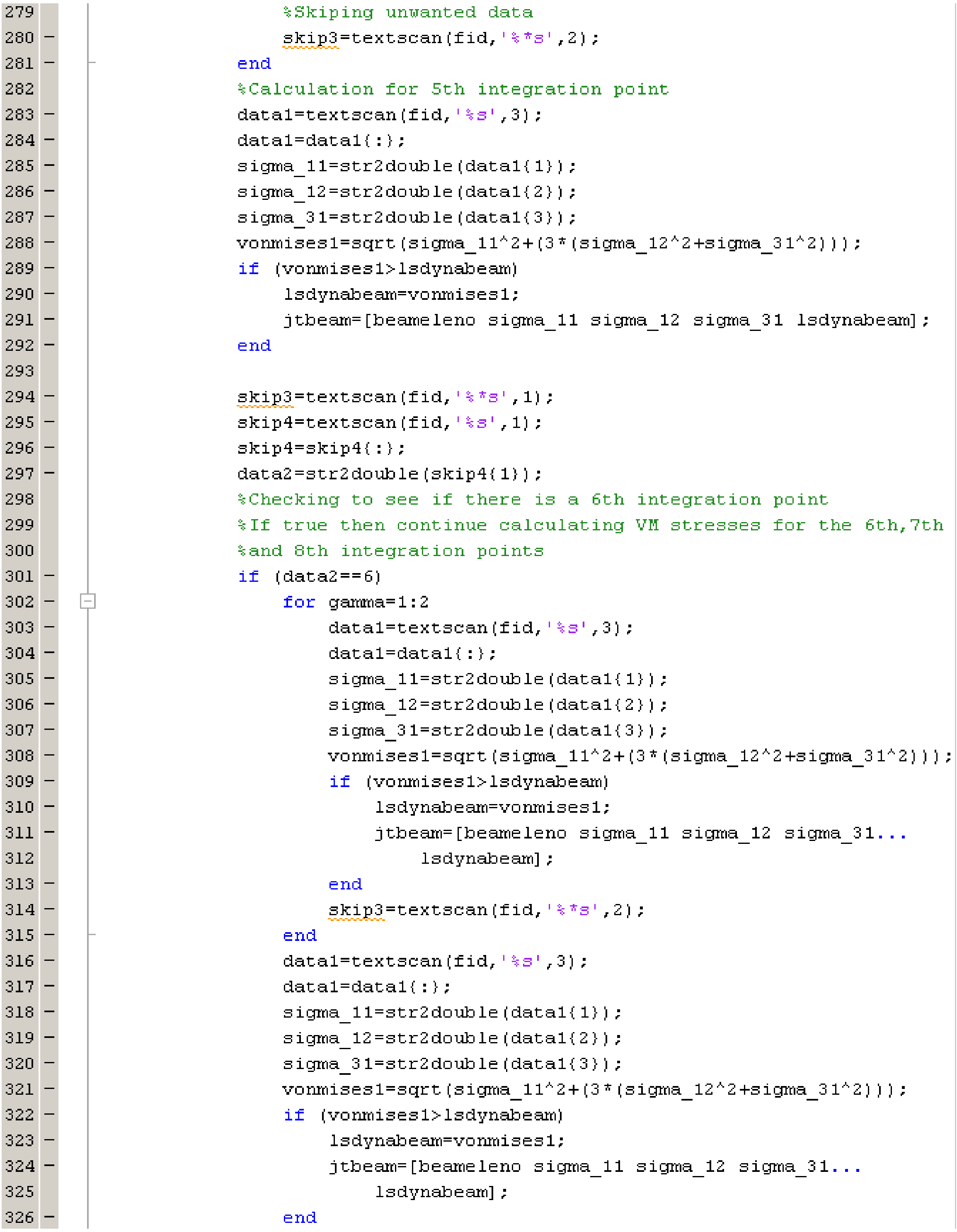

```
    %Skiping unwanted data
    skip3=textscan(fid,'%*s',2);
end
%Calculation for 5th integration point
data1=textscan(fid,'%s',3);
data1=data1{:};
sigma_11=str2double(data1{1});
sigma_12=str2double(data1{2});
sigma_31=str2double(data1{3});
vonmises1=sqrt(sigma_11^2+(3*(sigma_12^2+sigma_31^2)));
if (vonmises1>lsdynabeam)
    lsdynabeam=vonmises1;
    jtbeam=[beameleno sigma_11 sigma_12 sigma_31 lsdynabeam];
end

skip3=textscan(fid,'%*s',1);
skip4=textscan(fid,'%s',1);
skip4=skip4{:};
data2=str2double(skip4{1});
%Checking to see if there is a 6th integration point
%If true then continue calculating VM stresses for the 6th,7th
%and 8th integration points
if (data2==6)
    for gamma=1:2
        data1=textscan(fid,'%s',3);
        data1=data1{:};
        sigma_11=str2double(data1{1});
        sigma_12=str2double(data1{2});
        sigma_31=str2double(data1{3});
        vonmises1=sqrt(sigma_11^2+(3*(sigma_12^2+sigma_31^2)));
        if (vonmises1>lsdynabeam)
            lsdynabeam=vonmises1;
            jtbeam=[beameleno sigma_11 sigma_12 sigma_31...
                lsdynabeam];
        end
        skip3=textscan(fid,'%*s',2);
    end
    data1=textscan(fid,'%s',3);
    data1=data1{:};
    sigma_11=str2double(data1{1});
    sigma_12=str2double(data1{2});
    sigma_31=str2double(data1{3});
    vonmises1=sqrt(sigma_11^2+(3*(sigma_12^2+sigma_31^2)));
    if (vonmises1>lsdynabeam)
        lsdynabeam=vonmises1;
        jtbeam=[beameleno sigma_11 sigma_12 sigma_31...
            lsdynabeam];
    end
```

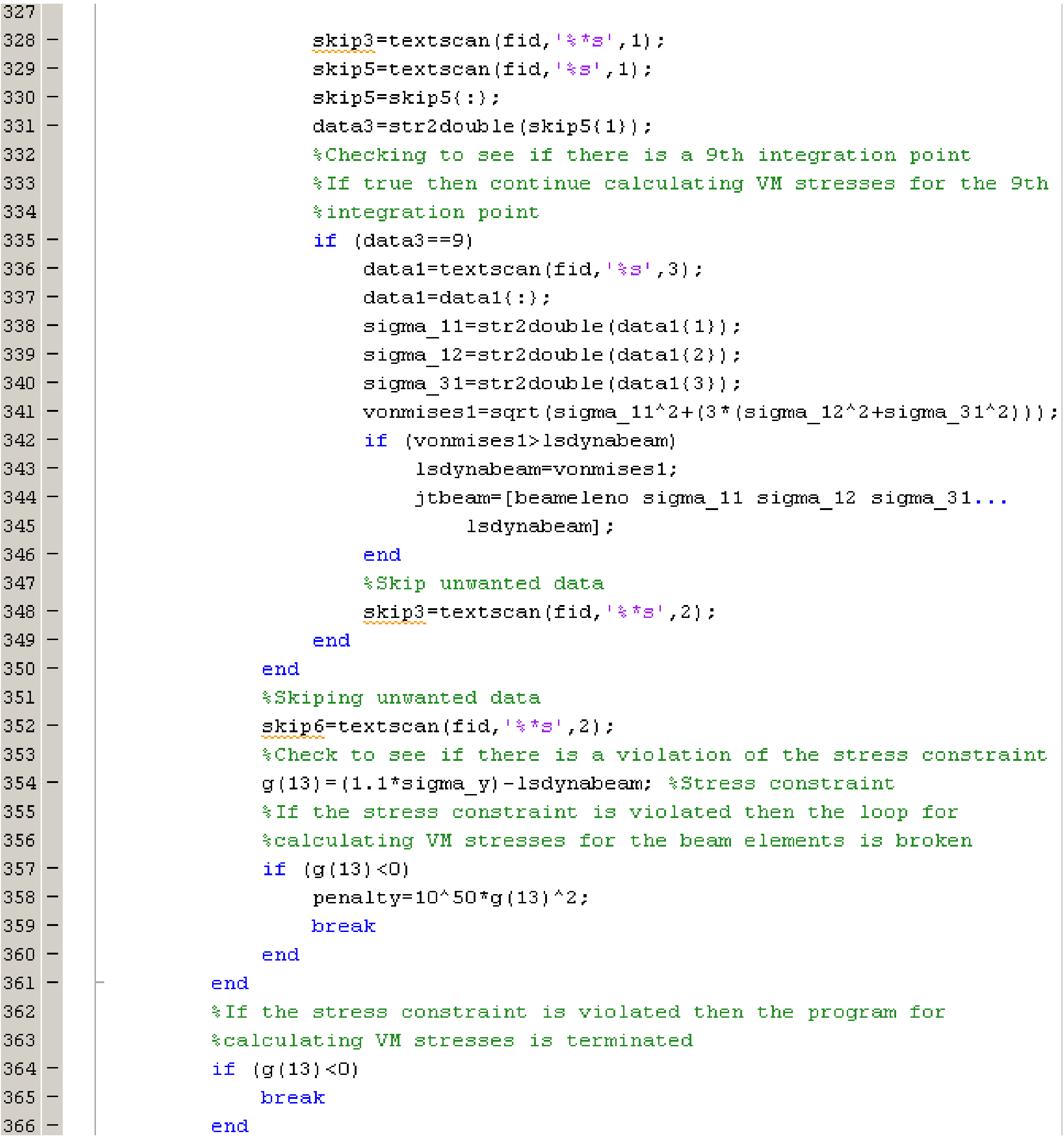

```

                skip3=textscan(fid,'%*s',1);
                skip5=textscan(fid,'%s',1);
                skip5=skip5{:};
                data3=str2double(skip5{1});
                %Checking to see if there is a 9th integration point
                %If true then continue calculating VM stresses for the 9th
                %integration point
                if (data3==9)
                    data1=textscan(fid,'%s',3);
                    data1=data1{:};
                    sigma_11=str2double(data1{1});
                    sigma_12=str2double(data1{2});
                    sigma_31=str2double(data1{3});
                    vonmises1=sqrt(sigma_11^2+(3*(sigma_12^2+sigma_31^2)));
                    if (vonmises1>lsdynabeam)
                        lsdynabeam=vonmises1;
                        jtbeam=[beameleno sigma_11 sigma_12 sigma_31...
                            lsdynabeam];
                    end
                    %Skip unwanted data
                    skip3=textscan(fid,'%*s',2);
                end
            end
            %Skiping unwanted data
            skip6=textscan(fid,'%*s',2);
            %Check to see if there is a violation of the stress constraint
            g(13)=(1.1*sigma_y)-lsdynabeam; %Stress constraint
            %If the stress constraint is violated then the loop for
            %calculating VM stresses for the beam elements is broken
            if (g(13)<0)
                penalty=10^50*g(13)^2;
                break
            end
        end
        %If the stress constraint is violated then the program for
        %calculating VM stresses is terminated
        if (g(13)<0)
            break
        end
```

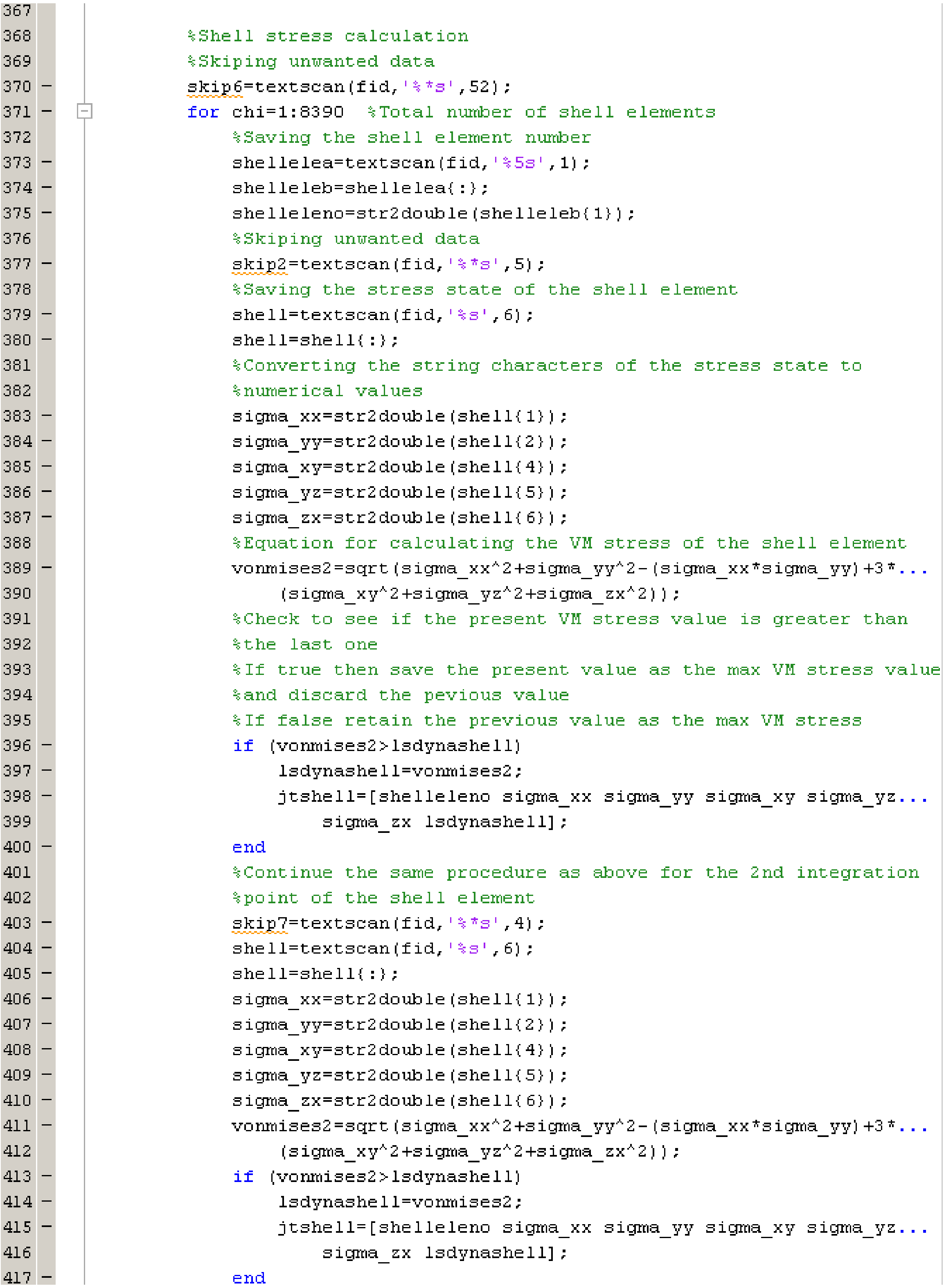

```

        %Shell stress calculation
        %Skiping unwanted data
        skip6=textscan(fid,'%*s',52);
        for chi=1:8390  %Total number of shell elements
            %Saving the shell element number
            shellelea=textscan(fid,'%5s',1);
            shelleleb=shellelea{:};
            shelleleno=str2double(shelleleb{1});
            %Skiping unwanted data
            skip2=textscan(fid,'%*s',5);
            %Saving the stress state of the shell element
            shell=textscan(fid,'%s',6);
            shell=shell{:};
            %Converting the string characters of the stress state to
            %numerical values
            sigma_xx=str2double(shell{1});
            sigma_yy=str2double(shell{2});
            sigma_xy=str2double(shell{4});
            sigma_yz=str2double(shell{5});
            sigma_zx=str2double(shell{6});
            %Equation for calculating the VM stress of the shell element
            vonmises2=sqrt(sigma_xx^2+sigma_yy^2-(sigma_xx*sigma_yy)+3*...
                (sigma_xy^2+sigma_yz^2+sigma_zx^2));
            %Check to see if the present VM stress value is greater than
            %the last one
            %If true then save the present value as the max VM stress value
            %and discard the pevious value
            %If false retain the previous value as the max VM stress
            if (vonmises2>lsdynashell)
                lsdynashell=vonmises2;
                jtshell=[shelleleno sigma_xx sigma_yy sigma_xy sigma_yz...
                    sigma_zx lsdynashell];
            end
            %Continue the same procedure as above for the 2nd integration
            %point of the shell element
            skip7=textscan(fid,'%*s',4);
            shell=textscan(fid,'%s',6);
            shell=shell{:};
            sigma_xx=str2double(shell{1});
            sigma_yy=str2double(shell{2});
            sigma_xy=str2double(shell{4});
            sigma_yz=str2double(shell{5});
            sigma_zx=str2double(shell{6});
            vonmises2=sqrt(sigma_xx^2+sigma_yy^2-(sigma_xx*sigma_yy)+3*...
                (sigma_xy^2+sigma_yz^2+sigma_zx^2));
            if (vonmises2>lsdynashell)
                lsdynashell=vonmises2;
                jtshell=[shelleleno sigma_xx sigma_yy sigma_xy sigma_yz...
                    sigma_zx lsdynashell];
            end
```

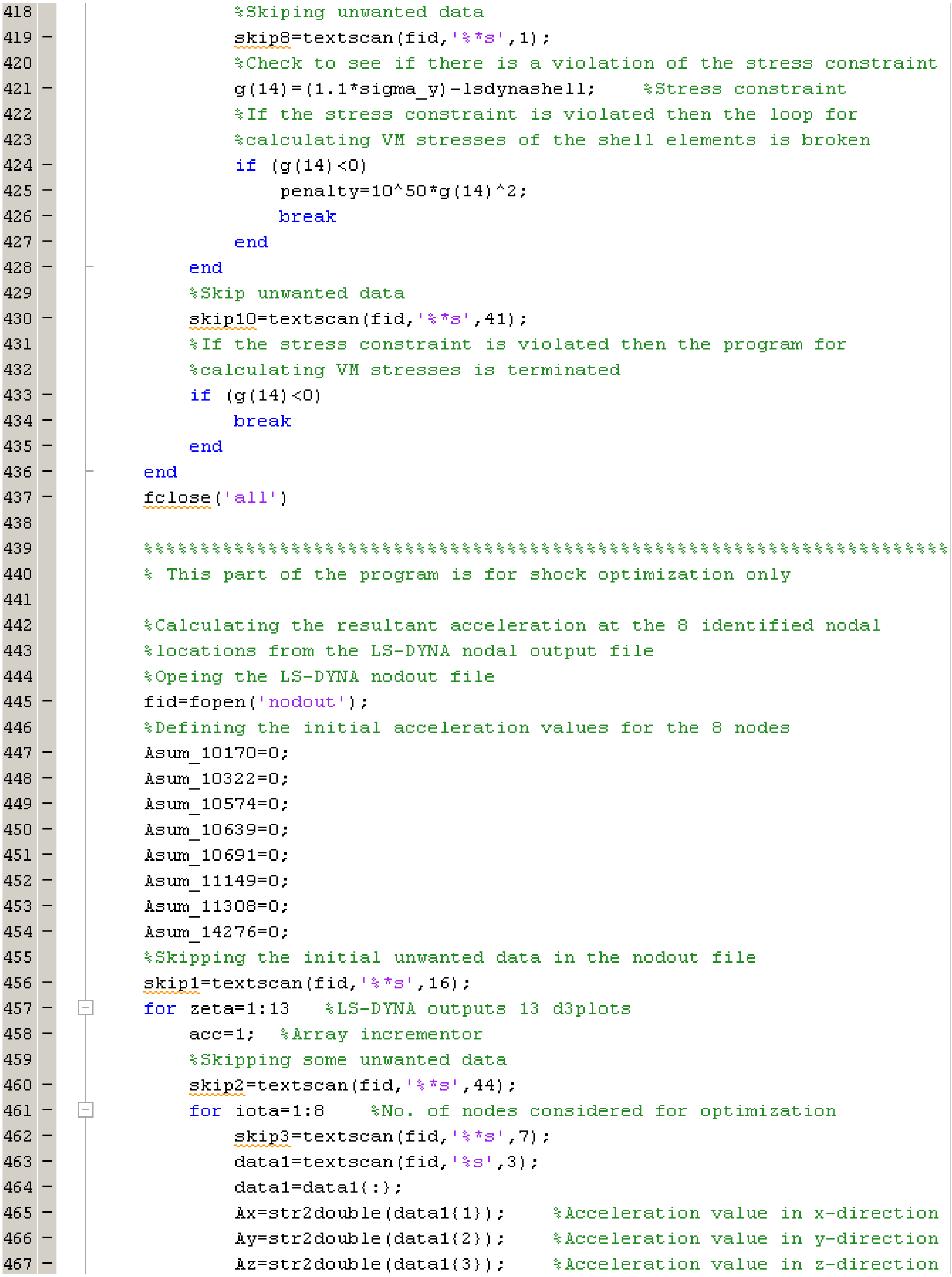

```
                %Skiping unwanted data
                skip8=textscan(fid,'%*s',1);
                %Check to see if there is a violation of the stress constraint
                g(14)=(1.1*sigma_y)-lsdynashell;    %Stress constraint
                %If the stress constraint is violated then the loop for
                %calculating VM stresses of the shell elements is broken
                if (g(14)<0)
                    penalty=10^50*g(14)^2;
                    break
                end
            end
            %Skip unwanted data
            skip10=textscan(fid,'%*s',41);
            %If the stress constraint is violated then the program for
            %calculating VM stresses is terminated
            if (g(14)<0)
                break
            end
        end
        fclose('all')

        %%%%%%%%%%%%%%%%%%%%%%%%%%%%%%%%%%%%%%%%%%%%%%%%%%%%%%%%%%%%%%%%%%%%%%%
        % This part of the program is for shock optimization only

        %Calculating the resultant acceleration at the 8 identified nodal
        %locations from the LS-DYNA nodal output file
        %Opeing the LS-DYNA nodout file
        fid=fopen('nodout');
        %Defining the initial acceleration values for the 8 nodes
        Asum_10170=0;
        Asum_10322=0;
        Asum_10574=0;
        Asum_10639=0;
        Asum_10691=0;
        Asum_11149=0;
        Asum_11308=0;
        Asum_14276=0;
        %Skipping the initial unwanted data in the nodout file
        skip1=textscan(fid,'%*s',16);
        for zeta=1:13   %LS-DYNA outputs 13 d3plots
            acc=1;  %Array incrementor
            %Skipping some unwanted data
            skip2=textscan(fid,'%*s',44);
            for iota=1:8    %No. of nodes considered for optimization
                skip3=textscan(fid,'%*s',7);
                data1=textscan(fid,'%s',3);
                data1=data1{:};
                Ax=str2double(data1{1});    %Acceleration value in x-direction
                Ay=str2double(data1{2});    %Acceleration value in y-direction
                Az=str2double(data1{3});    %Acceleration value in z-direction
```

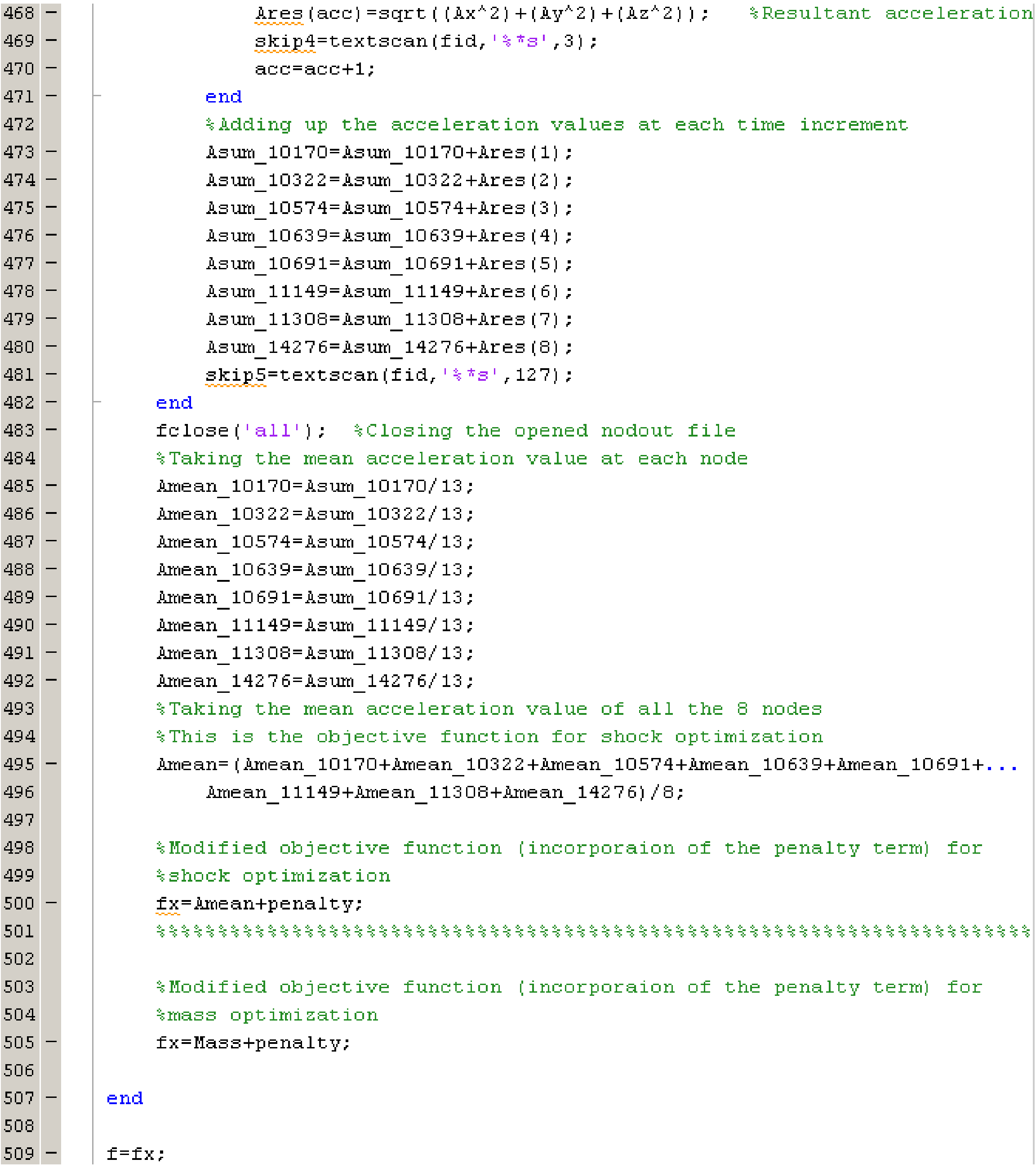

```
            Ares(acc)=sqrt((Ax^2)+(Ay^2)+(Az^2));   %Resultant acceleration
            skip4=textscan(fid,'%*s',3);
            acc=acc+1;
        end
        %Adding up the acceleration values at each time increment
        Asum_10170=Asum_10170+Ares(1);
        Asum_10322=Asum_10322+Ares(2);
        Asum_10574=Asum_10574+Ares(3);
        Asum_10639=Asum_10639+Ares(4);
        Asum_10691=Asum_10691+Ares(5);
        Asum_11149=Asum_11149+Ares(6);
        Asum_11308=Asum_11308+Ares(7);
        Asum_14276=Asum_14276+Ares(8);
        skip5=textscan(fid,'%*s',127);
    end
    fclose('all');  %Closing the opened nodout file
    %Taking the mean acceleration value at each node
    Amean_10170=Asum_10170/13;
    Amean_10322=Asum_10322/13;
    Amean_10574=Asum_10574/13;
    Amean_10639=Asum_10639/13;
    Amean_10691=Asum_10691/13;
    Amean_11149=Asum_11149/13;
    Amean_11308=Asum_11308/13;
    Amean_14276=Asum_14276/13;
    %Taking the mean acceleration value of all the 8 nodes
    %This is the objective function for shock optimization
    Amean=(Amean_10170+Amean_10322+Amean_10574+Amean_10639+Amean_10691+...
        Amean_11149+Amean_11308+Amean_14276)/8;

    %Modified objective function (incorporaion of the penalty term) for
    %shock optimization
    fx=Amean+penalty;
    %%%%%%%%%%%%%%%%%%%%%%%%%%%%%%%%%%%%%%%%%%%%%%%%%%%%%%%%%%%%%%%%%%%%%%%

    %Modified objective function (incorporaion of the penalty term) for
    %mass optimization
    fx=Mass+penalty;

end

f=fx;
```

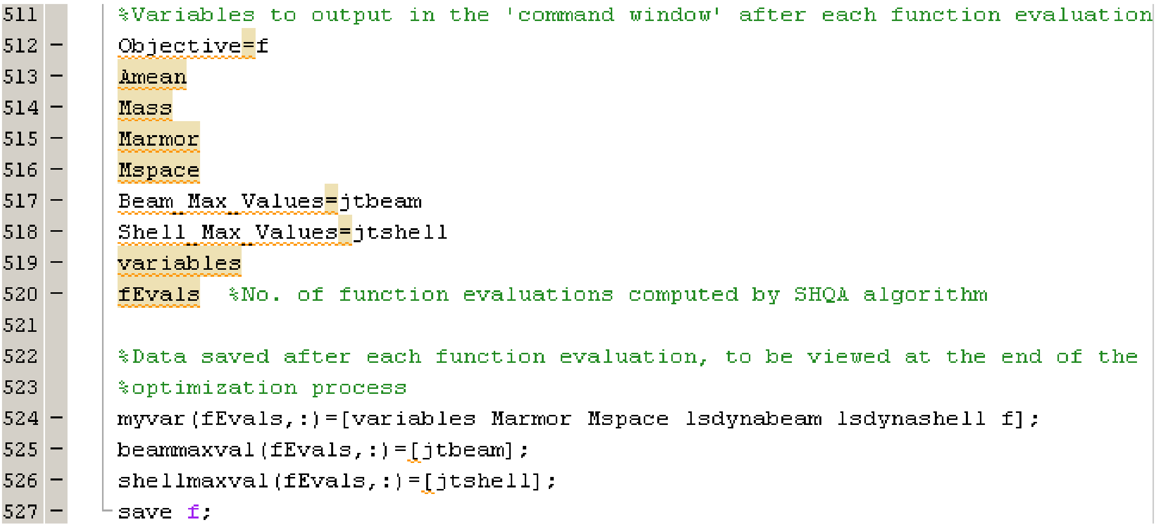

```
%Variables to output in the 'command window' after each function evaluation
Objective=f
Amean
Mass
Marmor
Mspace
Beam_Max_Values=jtbeam
Shell_Max_Values=jtshell
variables
fEvals  %No. of function evaluations computed by SHQA algorithm

%Data saved after each function evaluation, to be viewed at the end of the
%optimization process
myvar(fEvals,:)=[variables Marmor Mspace lsdynabeam lsdynashell f];
beammaxval(fEvals,:)=[jtbeam];
shellmaxval(fEvals,:)=[jtshell];
save f;
```

REFERENCES

1. Goldsmith W, Sackman JL (1991) Energy absorption by sandwich plates. A topic in crashworthiness. ASME-AMD 126:1-30.
2. Hassan JE, Frederick G (1996) Exact constraint design of vehicle components. Sensors, safety systems, and human factors :55-62.
3. Sickling DL, Reid JD, Rohde JR (1998) Development of a sequential kinking terminal for w-beam guardrails. Transportation research record 1647:89-96.
4. Ahmed AK, Haque MM, Rakheja S (1999) Nonlinear analysis of automatic hydraulic mounts for isolation of vibration and shock. Int J Vehicle Des 22:116-128.
5. Gupta AD (1997) Dynamic elasto-plastic response of a generic vehicle floor model to coupled transient loads. ASME-PVP 351:81-86.
6. Gupta AD, Santiago JM, Wisniewski HL (1992) Shock damage to sensitive components in an armored vehicle. Computers in Engineering, Proceedings of the International Conference and Exhibit 2:153-161.
7. Gupta AD, Santiago JM, Meyer C (1994) 3-D finite element modeling and analysis of an armored vehicle hull with multiple access openings. Computers in Engineering, Proceedings of the International Conference and Exhibit 2:581-587.
8. Medwadowski S (1985) Analysis of space frames and tension structures. International Association for Shell and Spatial Structures 26(87): 21-28.
9. Gaul L, Lenz J (1997) Nonlinear dynamics of structures assembled by bolted joints. Acta Mech 125:169-181.
10. Mackerle J (1996) Structural response to impact, blast and shock loadings a FE/BE bibliography (1993-1995). Finite Elem Anal Des 24:95-110.
11. Mackerle J (2000) Finite element vibration and dynamic response analysis of engineering structures: A bibliography (1994-1998). Shock Vib 7:39-56.
12. Meek JL, Loganathan S (1989) Large displacement analysis of space-frame structures. Computer Methods in Applied Mechanics and Engineering 72: 57-75.
13. Meek JL, Loganathan S (1989) Geometrically non-linear behavior of space frame structures. Computers and Structures 31(1): 35-45.
14. Meek JL, Tan HS (1984) Geometrically nonlinear analysis of space frames by an incremental iterative technique. Computer Methods in Applied Mechanics and Engineering 47: 261-282.
15. Masuda N, Nishiwaki T, Minagawa M (1987) Nonlinear dynamic analysis of frame structures. Comput Struct 27:103-110.
16. Karpurapu R, Yogendrakumar M (1993) A kinematic model for dynamic analysis of space frames. Computers & Structures 47(6): 945-955.
17. Vasilopoulos AA, Beskos DE (2009) Seismic design of space steel frames using advanced methods of analysis. Solid Dynamics and Earthquake Engineering 29: 194-218.
18. Goman WMH, Chan SL (1993) An accurate and efficient method for large deflection inelastic analysis of frames with semi rigid connections. J Constr Steel Res 26:171-191.
19. Chan SL (1996) Large deflection dynamic analysis of space frames. Comput Struct 58:381-386.

20. Sergeyey O, Mroz Z (2000) Sensitivity analysis and optimal design of 3D frame structures for stress and frequency constraints. Comput Struct 75:167-185.
21. Ogha M, Shigematsu T, Hara T (1993) A finite element-transfer matrix method for dynamic analysis of frame structures. Journal of Sound and Vibration 167(3): 401-411.
22. Liew JYR, Tang LK (2000) Advanced plastic hinge analysis for the design of tubular space frames. Engineering Structures 22: 769-783.
23. Liew JYR, Chen H, Shanmugam NE, Chen WF (2000) Improved nonlinear plastic hinge analysis of space frame structures. Engineering Structures 22: 1324-1338.
24. Huu CN, Kim SE, Oh JR (2007) Nonlinear analysis of space frames using fiber plastic hinge concept. Engineering Structures 29: 649-657.
25. Dabaon MA, Boghdadi MHE, Kharoob OF (2009) Experimental and numerical model for space steel and composite semi-rigid joints. Journal of Constructional Steel Research 65: 1864-1875.
26. Chen H, Blandford GE (1991) Thin-walled space frames II: Algorithmic details and applications. Journal of Structural Engineering 117: 2521-2539.
27. Yu Y, Luo YZ (2009) Finite particle method for kinematically indeterminate bar assemblies. Journal of Zhejiang University Science A 10(5): 669-676.
28. Haq M, Rudolph S (2007) A design language for generic space-frame structures design. International Journal of Computer Applications in Technology 30(1-2): 77-87.
29. Kollar L (1987) Stability problems of membranes structures and space frames. Journal of the International Association for Shell and Spatial Structures 27: 35-40.
30. Sastranegra A, Adachi T, Yamaji A (2005) Improvement of energy absorption of impacted column due to transverse impact. Int J Impact Eng 32:483-496.
31. Qui X, Deshpande V, Fleck NA (2003) Finite element analysis of the dynamic response of clamped sandwich beams subject to shock loading. Eur J Mech A-Solids 22:801-814.
32. Sheikh AE (2000) Behaviour of space frame roof structures with direct member loading. Journal of the International Association for Shell and Spatial Structures 41(133): 75-90.
33. Liu H, Yuan J, Hou S, Yang X (2009) Analysis of aseismatic performance of reinforced concrete frame side joints strengthened with carbon cloth. Key Engineering Materials 400-402: 707-711.
34. Overbey LA, Todd MD (2008) Damage assessment using generalized state-space correlation features. Structural Health Monitoring 7(4): 347-363.
35. Qian J, Ji X, Xu Y (2007) Two-stage damage diagnosis approach for steel braced space frame structures. Engineering Structures 29: 3277-3292.
36. Degertekin SO, Saka MP, Hayalioglu MS (2008) Optimal load and resistance factor design of geometrically nonlinear steel space frames via tabu search and genetic algorithm. Engineering Structures 30: 197-205.
37. Jalkanen J, Koski J (2005) Heuristic methods in space frame optimization. AIAA/ASME/ASCE/AHS/ASC Structures, Structural Dynamics and Materials Conference 2:1214-1228.
38. Degertekin SO (2007) A comparison of simulated annealing and genetic algorithm for optimum design of nonlinear steel space frames. Struct Multidiscip O 34:347-359.

39. Torstenfelt B, Karlbring A (2006) Structural optimization of modular product families with application to car space frame structures. Struct Multidiscip O 32:133-140.
40. Svanberg K (1987) The method of moving asymptotes-a new method for structural optimization. Int J Numer Meth Eng 24:259-373.
41. Hayalioglu MS (2001) Optimum load and resistance factor design of steel space frames using genetic algorithm. Struct Multidisc Optim 21: 292-299.
42. Soegiarso R, Adeli H (1997) Optimum load and resistance factor design of steel space-frame structures. Journal of Structural Engineering 123(2): 184-192.
43. Soegiarso R, Adeli H (1997) Optimization of large space frame steel structures. Engineering Journal 34(2): 54-60.
44. Czyz JA, Lukasiewicz SA (1998) Multimodal optimization of space frames for maximum frequency. Computers and Structures 66(2-3): 187-199.
45. Hamza K, Mahmoud H, Saitou K (2003) Design optimization of N-shaped roof trusses using reactive taboo search. Applied Soft Computing 3: 221-235.
46. Hamza K, Saitou K (2009) Automated vehicle structural crashworthiness design via a crash mode marching algorithm. Proceedings of the ASME International Design Engineering Technical Conferences and Computers and Information in Engineering Conference.
47. Lyu N, Saitou K (2005) Decomposition-based assembly synthesis of a three dimensional body-in-white model for structural stiffness. Journal of Mechanical Design 127(1): 34-48.
48. Lyu N, Saitou K (2006) Decomposition-based assembly synthesis of space frame structures using joint library. Journal of Mechanical Design 128(1): 243-251.
49. Lee B, Saitou K (2003) Decomposition-based assembly synthesis for in-process dimensional adjustability. Journal of Mechanical Design 125(3): 464-473.
50. Lee B, Saitou K (2006) Three-dimensional assembly synthesis for robust dimensional integrity based on screw theory. Journal of Mechanical Design 128(1): 57-65.
51. Lyu N, Lee B, Saitou K (2006) Optimal subassembly partitioning of space frame structures for in-process dimensional adjustability and stiffness. Journal of Mechanical Design 128(1): 527-535.
52. Trabia, MB, O'Toole BJ, Ladkany SG, Naraparaju J, Sridharala S, Huang J (2005) Optimization of Joint Design for Side Panel of a Military Vehicle for Shock Reduction. Shock and Vibration Symposium 76.
53. Trabia MB, Huang J, O'Toole BJ, Sakaray U (2006) Optimization of Joint Design for Bottom Panel of a Military Vehicle for Shock Reduction Under Blast Loading. Shock and Vibration Symposium 77.
54. Sakaray U, O'Toole BJ, Trabia MB, Thota J (2007) Optimization of a Vehicle Space Frame under Ballistic Impact Loading. Proceedings of the ASME International Design Engineering Technical Conferences and Computers and Information in Engineering Conference 6:317-324.
55. Baccouche MR, Mahmood HF (1998) Design of extruded aluminum space frame front end structutres for crash energy management-Part II. ASME Applied Mechanics Division 230: 1-15.

56. Baccouche MR, Mahmood HF, Shivakumar AK, Jawad SA (1999) Crashworthiness performance of space frame aluminum structure in NCAP's 35 mph full frontal. ASME Applied Mechanics Division 237: 85-96.
57. LS-DYNA theoretical manual. Livermore Software Technology Corportion.
58. Zekai C, Trabia MB (2003) Optimization of the closure-weld region of cylindrical containers for long-term corrosion resistance using the successive heuristic quadratic approximation technique. Journal of Mechanical Design 125: 533-539.
59. Juvinall RC, Marshek KM (2006)Fundamentals of machine component design. John Wiley & Sons, Inc. Fourth Edition.
60. G.V. Rekalitis, A. Ravindran, K.M. Ragsdell, (2006) Engineering Optimization: Methods and Applications. Wiley.
61. SignalCalc ACE. Data Physics Corporation. www.dataphysics.com. Accessed 23 April 2010.
62. ScopeCorder DL750/DL750P/SL1400. Yokogawa Electric Corporation. http://scopecorder.net/download/DL750_specifications.pdf. Accessed 23 April 2010.
63. Impact Hammer Model 086D05, ICP. PCB Piezotronics Vibration Division. http://www.pcb.com/spec_sheet.asp?model=086D05. Accessed on 23 April 2010.
64. ICP Accelerometer Model 352C22. PCB Piezotronics Vibration Division. http://www.pcb.com/spec_sheet.asp?model=352C22. Accessed on 23 April 2010.
65. Installation Drawing and Specification Model 4103C. Dytran Instruments, Inc. http://www.dytran.com/img/products/4103.pdf. Accessed on 23 April 2010.
66. Hand-Held Shaker Model 394C06. PCB Piezotronics Vibration Division. http://www.pcb.com/spec_sheet.asp?model=394C06&item_id=2198. Accessed on 23 April 2010.

VITA

Graduate College
University of Nevada, Las Vegas

Jagadeep Thota

Degrees:

Bachelor of Engineering, Mechanical Engineering, 2001
Bangalore Institute of Technology, Bangalore University, India

Master of Science, Mechanical Engineering, 2006
University of Nevada, Las Vegas

Special Honors and Awards:

- Inducted into Tau Beta Pi, engineering honor society (2005)
- Awarded second prize for paper in 2005 AIAA student conference (2005)
- Outstanding paper award, 51st International SAMPE Symposium & Exhibition (2006)
- Inducted to Phi Kappa Phi, honor society (2006)
- Awarded third prize for paper in 2006 AIAA student conference (2006)
- Outstanding academic achievement award from the UNLV Honors Convocation (2006)
- Best essay award from the ASME Nevada professional chapter (2008)
- Recipient of the 2008 Summer Session Scholarship from UNLV Graduate College (2008)

Publications:

- Trabia MB, O’Toole BJ, Thota J, Matta KK (2005) Modeling of a light-weight composite blast-containment vessel. ASME International Mechanical Engineering Congress and Exposition, Orlando, FL.
- O'Toole BJ, Trabia MB, Thota J, Wilcox T, Nakelswamy KK (2006) Structural response of blast loaded composite containment vessels. SAMPE Journal 42(4): 6-13.
- Thota J, Sridharala S, Sakaray U, O’Toole BJ (2006) Design and fabrication of a composite roller skate chassis. 38th SAMPE International Technical Conference, Dallas, TX.
- Sakaray U, O’Toole BJ, Thota J (2006) Numerical techniques in the simulation of energy absorbing materials in blast loaded structures. 38th SAMPE International Technical Conference, Dallas, TX.
- Thota J, Trabia MB, O’Toole BJ, Sridharala S (2006) Optimization of a light-weight composite explosion-proof vesse. 77th Shock and Vibration Symposium, Monterey, CA.

- O’Toole BJ, Rahman S, Malpica J, Thota J, Raagas S (2007) Effect of microsphere and binder properties on state-change material performance. International SAMPE Symposium and Exhibition, Baltimore, MD.
- O’Toole BJ, Rahman S, Malpica J, Thota J, Raagas S (2007) High temperature properties of a state-change material. International SAMPE Symposium and Exhibition, Baltimore, MD.
- O’Toole BJ, Trabia MB, Thota J (2007) Analysis and optimization of a composite blast containment vessel. 17th US Army Symposium on Solid Mechanics, Baltimore, MD.
- Thota J, O’Toole BJ, Trabia MB, Sakaray U (2007) Optimization of a vehicle space frame under ballistic impact loading. ASME IDETC: 33rd Design Automation Conference, Las Vegas, NV.
- Thota J, Ayyaswamy AK, Trabia MB, O’Toole BJ (2007) Optimization of a light-weight blast containment vessel structural response. ASME International Mechanical Engineering Congress and Exposition, Seattle, WA.
- Trabia MB, O'Toole BJ, Thota J, and Matta KK (2008) Finite element modeling of a light-weight composite blast containment vessel. ASME Journal of Pressure Vessel Technology 130: 011205.
- Nelson SM, O’Toole BJ, Thota J (2008) Characterization of a unidirectional carbon fiber/epoxy composite for prototype design. International SAMPE Symposium and Exhibition, Long Beach, CA.
- Thota J, Trabia MB, O’Toole BJ (2008) Optimization of a military vehicle space frame subject to high impact loading. ASME International Mechanical Engineering Congress and Exposition, Baltimore, MD.
- O'Toole BJ, Rahman S, Malpica J, Thota J, and Raagas S (2008) High temperature properties of a state-change material. SAMPE Journal 44(1): 42-52.
- Nelson SM, O’Toole BJ, Thota J (2009) Mechanical characterization of a porous state-change material for water soluble tooling. World Journal of Engineering.
- Thota J, Clark K, O’Toole BJ (2009) Quasistatic and vibration response of prototype composite ducts for aircraft components. World Journal of Engineering.
- Thota J, Trabia MB, O’Toole BJ (2009) Shock optimization in a military vehicle space frame. 10th US National Congress on Computational Mechanics, Columbus, OH.
- Nelson SM, O’Toole BJ, Thota J (2009) Uniaxial compression and creep behavior of a porous state-change material at ambient and elevated temperatures. International SAMPE Symposium and Exhibition, Baltimore, MD.
- Thota J, Trabia MB, O’Toole BJ (2009) Shock optimization in a military vehicle with internal space frame. ASME International Mechanical Engineering Congress and Exposition, Orlando, FL.
- Nelson SM, Thota J, O’Toole BJ (2010) Optimization of carbon fiber/epoxy tubes loaded in bending and compression. International SAMPE symposium and Exhibition, Seattle, WA.

- Thota J, Clark K, Higgins T, Nelson SM, O’Toole BJ (2010) Fabrication and analysis of prototype composite ducts for an unmanned aerial vehicle. International SAMPE Symposium and Exhibition, Seattle, WA.
- Thota J, Trabia MB, and O'Toole BJ (2010) Optimization of a light-weight composite blast containment vessel. ASME Journal of Pressure Vessel Technology 131: 031209.

Dissertation Title: Optimal Design of Vehicle with Internal Space Frame Structure Subjected to High Impact Load

Dissertation Examination Committee:
Chairperson, Mohamed B.Trabia, Ph. D.
Chairperson, Brendan J. O’Toole, Ph. D.
Committee Member, Woosoon Yim, Ph. D.
Committee Member, Georg F. Mauer, Ph. D.
Committee Member, Zhiyong Wang, Ph. D.
Graduate Faculty Representative, Samaan G. Ladkany, Ph. D.